UNIVERSITY OF READING

Department of Meteorology

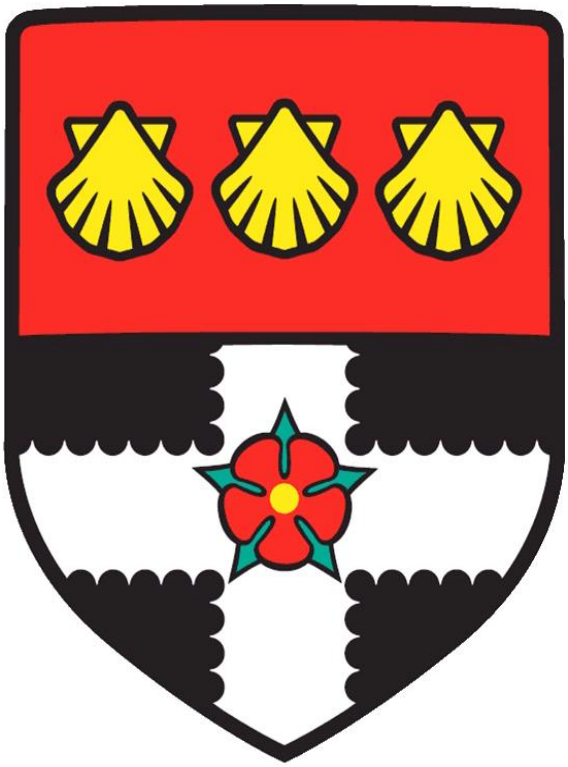

Understanding the Earth's Energy Flows from a Constellation of Satellites

Jake Joseph Gristey

A thesis submitted for the degree of Doctor of Philosophy

June 2018

DECLARATION

I confirm that this is my own work and the use of all material from other sources has been properly and fully acknowledged.

Jake Gristey

ABSTRACT

Observing Earth's energy flows is vital for monitoring, predicting and explaining climate changes. The top-of-atmosphere outgoing energy flows, comprised of reflected-solar and emitted-thermal radiation, pose a particular observational challenge due to their rapid evolutions. Recent technological advances have presented an exciting opportunity to capture and understand outgoing radiation variability from a constellation of satellites, yet this potential has not been explored.

Firstly, to evaluate the potential of the constellation concept, a new recovery method is developed and a series of simulation experiments are conducted. Using simple broadband radiometers as an example, a constellation of 36 satellites is found to be capable of monitoring global outgoing radiation to a spatial resolution of 1000 km at hourly time scales. The error in recovered daily mean reflected-solar and emitted-thermal irradiance is 0.16 and −0.13 W m^{-2}, with estimated hourly uncertainty of 0.45 and 0.15 W m^{-2}, respectively.

Secondly, to gain insight into diurnal variability that a satellite constellation could reveal, dominant diurnal patterns are extracted from modelled global outgoing radiation. Diurnal patterns related to solar zenith angle (88.4 %) and both convective and marine stratocumulus cloud (6.7 %) are found to dominate the reflected-solar radiation, whereas surface heating (68.5 %) and convective cloud (16.0 %) dominate the emitted-thermal radiation. Strong coupling between radiation and other model variables support these processes, and reveal an intriguing time lag in the radiation response to cloud variations.

Finally, to assess the additional value of spectrally resolved observations from the constellation, top-of-atmosphere short-wave reflectance spectra are computed. Clustering of the computed spectra reveals signatures related to distinct surface properties and cloud regimes. By assigning real observations to computed clusters, intra-annual and inter-annual variability associated with the West African monsoon is detected, including a 14.5 % annual range in relative frequency of a vertically-distributed cloud signature, demonstrating an alternative route forward for monitoring our climate system.

ACKNOWLEDGEMENTS

First and foremost, I thank my primary supervisors Christine Chiu and Robert Gurney. Both have provided fantastic support throughout. Christine, I especially thank you for your meticulous feedback on my work, and the generosity with your time including hosting me during a visit to Colorado State University to complete this thesis. Robert, your insights into the novelty and potential impact of this work have been extremely valuable, and I am grateful for your ongoing efforts to communicate results to external organisations and develop the ideas further. I thank Graeme Stephens for occasional but insightful supervisor meetings, and Keith Shine who kindly offered to step into a supervisory role during the later stages resulting in many productive discussions.

I would also like to acknowledge feedback from my monitoring committee members Richard Allan and Keith Shine, and my collaborators Cyril Morcrette, Stephan Havemann, Jean-Claude Thelen, Jacqueline Russell, Helen Brindley, Peter Hill and Shin-Chan Han. Feedback during committee meetings improved my writing and critical thinking. Likewise, feedback from collaborators improved our published works. Particular thanks go to Met Office collaborators Cyril, Stephan and Jean-Claude who provided customised model output and radiative transfer tools central to this thesis.

I am very grateful for the incredible support network that I have had around me during my doctoral studies. Everyone in the Lyle 5 office and wider department have created an engaging work environment, and also organised many enjoyable social activities. My family have been incredibly supportive whenever I have needed advice. Most importantly, my wife Megan has been there for me every step of the way and helped me to maintain a positive attitude throughout.

Finally, I am appreciative of the financial support that I have received. A stipend and funding to attend multiple conferences has been provided by the Natural Environment Research Council (NERC) SCience of the Environment: Natural and Anthropogenic pRocesses, Impacts and Opportunities (SCENARIO) Doctoral Training Partnership. Additional financial support has been provided by the Met Office via a Collaborative Awards in Science and Engineering (CASE) agreement, coordinated by Phil Evans, and by the National Aeronautics and Space Administration (NASA) Jet Propulsion Laboratory (JPL) for an extended visit in 2015, arranged by Graeme Stephens.

CONTENTS

1 CHAPTER ONE: Introduction....1

1.1 Earth's energy budget.... 1

1.1.1 Definition and components....1

1.1.2 Previous satellite measurements....3

1.1.3 Scientific relevance....6

1.2 Constellation concept....10

1.2.1 Opportunity presented by small satellites....10

1.2.2 Applicability to EOR measurements....12

1.3 Thesis objective and proposed science questions....13

2 CHAPTER TWO: Determination of global Earth outgoing radiation at high temporal resolution using a theoretical constellation of satellites....15

2.0 Statement of publication status....15

2.1 Introduction....15

2.2 Simulation experiment for recovering irradiance fields....18

2.2.1 Simulation of measurements....18

2.2.2 Recovery method....20

2.2.3 Experiment design and setup....23

2.3 Results....26

2.3.1 Recovered outgoing irradiance from the baseline constellation....26

2.3.2 Sensitivity tests....34

2.3.2.1 Assumption of isotropic radiation....34

2.3.2.2 Instrument performance and calibration....37

2.3.2.3 Number of satellites....39

2.4 Summary (published abstract)....41

3 CHAPTER THREE: Insights into the diurnal cycle of global Earth outgoing radiation using a numerical weather prediction model....42

3.0 Statement of publication status....42

3.1 Introduction....42

3.2 Data....45

3.2.1 Global model output....45

3.2.2 Supporting satellite datasets 46
3.3 Method 48
3.3.1 Pre-processing.....48
3.3.2 Extracting dominant patterns of EOR diurnal variability.....49
3.3.3 Coupling dominant patterns of diurnal variability.....50
3.4 Results.....51
3.4.1 Dominant patterns of diurnal variability in modelled global OLR.....51
3.4.2 Dominant patterns of diurnal variability in TOA albedo.....56
3.4.2.1 From model output.....56
3.4.2.2 From GERB observations 62
3.4.3 Coupled patterns of diurnal variability in EOR and other geophysical variables 64
3.4.3.1 OLR.....64
3.4.3.2 TOA albedo.....67
3.4.3.3 Lag times in GERB and SEVIRI observations 68
3.5 Summary (published abstract).....70

4 CHAPTER FOUR: Short-wave spectral radiation budget signatures and their physical controls.....71
4.0 Statement of publication status 71
4.1 Introduction.....71
4.2 Data and methodology 74
4.2.1 Observed hyperspectral reflectance from SCIAMACHY 74
4.2.2 Computed hyperspectral reflectance.....75
4.2.2.1 Input from A-train satellite observations 75
4.2.2.2 Fast radiative transfer code 77
4.2.3 Radiative signature clustering.....79
4.3 Results.....81
4.3.1 Clusters of computed reflectance spectra.....81
4.3.1.1 Spectral signatures and their controlling properties.....81
4.3.1.2 Cloud radiative effects of each cluster 90
4.3.2 Variations with spatial scale.....94
4.3.3 Tracking variability in SCIAMACHY observations.....103

4.4 Summary 107

5 CHAPTER FIVE: Summary, conclusions and future work 108

5.1 Summary and conclusions.....108

5.2 Future work 115

6 REFERENCES 120

7 APPENDIX I: List of acronyms 144

1 Introduction

1.1 Earth's energy budget

1.1.1 Definition and components

The top-of-atmosphere (TOA) energy budget presents the most fundamental equation of Earth's climate. Over multi-year timescales, if there is more energy entering than leaving at the TOA, the climate system must warm on average. It is therefore of vital importance that the balance between these TOA energy flows, commonly referred to as the Earth Radiation Budget (ERB), can be observed with sufficient accuracy, frequency and coverage for climate change studies.

The residual in the TOA energy flows, or net radiation imbalance, N, is not observed directly from satellites. Instead, the three components are observed: the incoming solar radiation or total solar irradiance (TSI), the outgoing long-wave radiation (OLR) and the reflected short-wave radiation (RSR). From these components, N can be calculated simply as

$$N = \frac{\mathrm{TSI}}{4} - (\mathrm{OLR} + \mathrm{RSR}), \qquad (1.1)$$

where the factor of a quarter applied to TSI relates the radiation intercepted by Earth to the total surface area of Earth. Defined in this way, N is positive when there is an accumulation of energy in the climate system. A schematic diagram representing Eq. (1.1), and the relationship of each of the terms with the underlying atmosphere and surface, is shown in Fig. 1.1. Note that many recent versions of Fig. 1.1 are available in the literature [e.g., *Trenberth*, 2009; *Stephens and L'Ecuyer*, 2015; *Wild et al.*, 2015], but estimates of the components of the TOA energy flows are broadly consistent across the different versions. These components are discussed in further detail for the remainder of this section.

The TSI is the primary energy source for physical processes in the Earth system, exceeding any other input by four orders of magnitude. Despite being commonly referred to as the "solar constant", TSI exhibits a distinct 11-year cycle in sunspot activity [*Gnevyshev*, 1977; *Hathaway*, 2015] that is modulated by much longer-term variations [*Owens et al.*, 2017; *Usoskin*, 2017]. Even small variations in TSI can produce natural forcing of Earth's climate with global and regional-scale responses

[*Gray et al.*, 2010; *Lockwood*, 2012; *Haigh et al.*, 2015]. Knowledge of the Earth's energy budget therefore requires accurate and stable TSI measurements. The latest measurements of TSI, provided by the Total Irradiance Monitor (TIM) on the National Aeronautics and Space Administration (NASA) Solar Radiation and Climate Experiment (SORCE), suggest a value of 1361 W m^{-2} [*Kopp and Lean*, 2011], lower than previous estimates. This new reference level has been used to extend the TSI record back in time during the satellite record [*Dudok de Wit et al.*, 2017], or hundreds of years beyond the satellite record using proxies for TSI such as sunspot area indices [*Coddington et al.*, 2016]. The uncertainty in these recent measurements of TSI from TIM has been estimated as ± 0.5 W m^{-2}, or just 0.04 % [*Kopp and Lean*, 2011]. This equates to an uncertainty of ± 0.1 W m^{-2} for the incoming solar radiation averaged over the Earth's surface (see Fig. 1.1) which, importantly, is substantially smaller than the estimated magnitude of N.

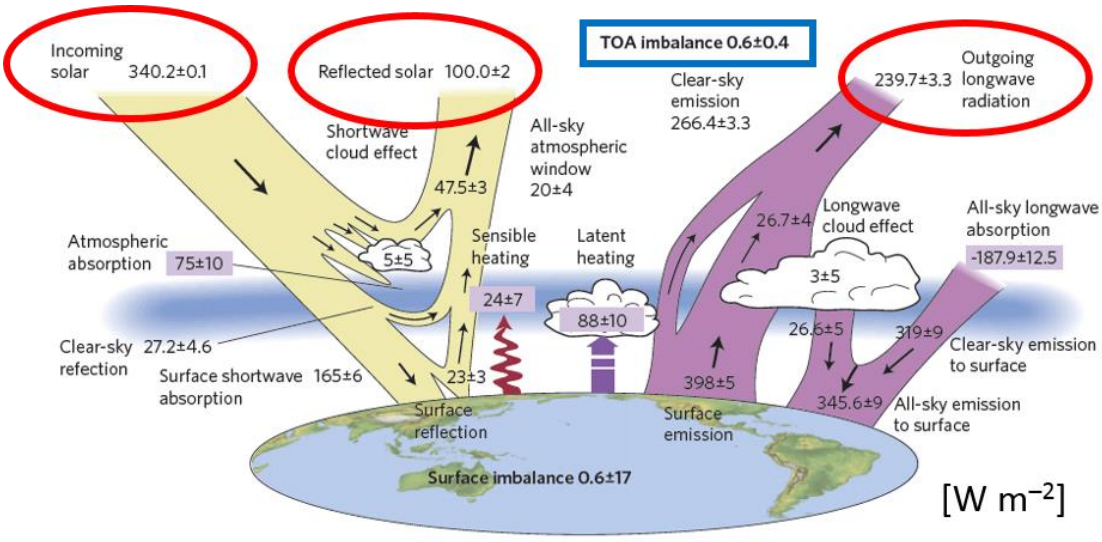

Figure 1.1. Earth's global annual mean energy budget for the period 2000–2010 (adapted from *Stephens et al.* [2012]). At the top-of-atmosphere, satellite observations indicate an approximate balance between the incoming solar, reflected solar and outgoing long-wave radiation (red circles). However, ocean heat content observations indicate a positive residual leading to a radiation imbalance (blue rectangle).

The outgoing energy flows, as opposed to the TSI, are dynamic by nature. They are inherently connected to the rapidly evolving Earth scene from which the radiation originates and are therefore more difficult both to observe and to understand. The OLR

and RSR currently observed by the Clouds and the Earth's Radiant Energy System (CERES) have uncertainties of 3.3 and 2.0 W m^{-2}, or 1.4 and 2.0 %, respectively (see Fig. 1.1, and note that these values are similar to updated estimates by *Loeb et al.* [2018]). Since the uncertainties in satellite observations of OLR and RSR are almost an order of magnitude larger than the estimated magnitude of N, around 0.6 W m^{-2} (again see Fig. 1.1, and note that this value is also similar to updated estimates by *Johnson et al.* [2016]), the imbalance cannot be observed from satellites with sufficient uncertainty to resolve its sign. Instead, improved absolute accuracy in N, as shown in Fig. 1.1, is derived from ocean heat content observations [*Lyman et al.*, 2010]. The rationale is that any excess energy entering at the TOA over multi-year timescales is predominantly stored in the oceans, because the heat capacity of the oceans overwhelms that of the atmosphere, land and ice [*Church et al.*, 2011]. Given the much larger uncertainty associated with satellite observations of OLR and RSR, compared with TSI, this thesis focuses on observations of the outgoing energy flows only, collectively referred to as Earth Outgoing Radiation (EOR).

1.1.2 Previous satellite measurements

Dedicated satellite measurements of EOR have been made since the beginning of the space age. After several early launch failures, the first usable measurements were collected over a period of 7-months by the Explorer VII satellite, launched in 1959 [*Suomi*, 1960]. The wide-field-of-view (WFOV) radiometers on this satellite consisted of a black hemisphere, that measured the total EOR, and a white hemisphere, that only measured the OLR by reflecting away the RSR. The RSR was then calculated as the difference between the two. Unfortunately, the white hemisphere rapidly degraded, rendering the daytime measurements useless. However, the radiometers provided useful information at night time when the instrument was in the Earth's shadow. By analysing these night time measurements, *Weinstein and Suomi* [1961] presented the first scientific results from satellite based EOR measurements. They showed that high magnitudes of OLR were associated with regions of clear-sky and high surface pressure, whereas low magnitudes of OLR were associated with cloudy low surface pressure systems, as was expected.

In the years that followed the first EOR measurements from Explorer VII in 1959, several other early satellites led to important advances in ERB science. The Television

Infrared Observational Satellite (TIROS) series of satellites, launched in the early 60s, provided the first complete year of observations to reveal seasonal variations [*Rao*, 1964], and used narrow-field-of-view (NFOV) scanning radiometers to observe finer spatial scale distributions [*Bandeen et al.*, 1961]. The Environmental Sciences Service Administration (ESSA), National Oceanic and Atmospheric Administration (NOAA), and Nimbus satellites that flew during the 1960s and 70s were launched on more powerful rockets, capable of reaching polar orbits. These satellites provided global coverage over multi-year timescales and led to the first satellite estimates of planetary albedo and emission [*Vonder Haar and Suomi*, 1971; *Gruber*, 1977; *Gruber and Winston*, 1978; *Gruber and Krueger*, 1984]. In 1975, a dedicated ERB instrument was launched on Nimbus-6, and later Nimbus-7 [*Smith et al.*, 1977; *Jacobowitz et al.*, 1984; *Kyle et al.*, 1993]. This ERB instrument had both WFOV and NFOV sensors, and was the first to measure all 3 components of ERB: the incoming solar, reflected solar, and emitted thermal radiation. The Nimbus-7 NFOV scanner was used to derive the first Angular Distribution Models (ADMs) [*Suttles et al.*, 1988, 1989]. A detailed discussion of these early measurements is provided by *House et al.* [1986].

A distinct landmark was achieved with the launch of the three-satellite ERB Experiment (ERBE) in the 1980s [*Barkstrom*, 1984]. The ERBE concept was driven by an interest from the scientific community for continued observations of ERB as well as the desire to obtain more accurate measurements through improved sampling. The sampling was provided by 3 identical instruments, each similar to that on Nimbus-7. The instruments were hosted on two Sun-synchronous NOAA satellites and a dedicated drifting ERB Satellite (ERBS). Importantly, the combination of the two NOAA satellites and ERBS provided the sampling required to capture both global EOR variability and monthly average diurnal variation at the regional scale [*Harrison et al.*, 1983]. The measurements from ERBE provided detailed global maps of the short-wave and long-wave cloud radiative effects and, crucially, revealed that the net cloud radiative effect is emphatically negative [*Hartmann*, 1993].

The ERBE was followed by the CERES [*Wielicki et al.*, 1996] that provides global EOR observations to this day. The first CERES launch was in 1997 aboard the Tropical Rainfall Measuring Mission (TRMM) on a drifting orbit that sampled diurnal variability, similar to the ERBS. Unfortunately, due to an instrument anomaly, CERES

on TRMM only provided 9-months of useful science data [*Loeb and Kato*, 2002]. Six further CERES flight models have since been launched, but all in Sun-synchronous orbits. Geostationary narrow-band observations are utilised to incorporate diurnal variability into the CERES products [*Doelling et al.*, 2013, 2018]. Another instrument, the Scanner for Radiation Budget (ScaRaB), currently captures long-term averaged diurnal variability due to the drifting low-Earth orbit of the MeghaTropiques satellite [*Viollier and Raberanto*, 2010], but the coverage is limited to the central tropics due to the very low inclination of the orbit. The CERES instruments have provided a global EOR dataset with unparalleled accuracy and precision for over two decades, and their flagship Energy Balanced And Filled (EBAF) product [*Loeb et al.*, 2009, 2018] has been extensively used within the scientific community. However, the final flight model of CERES has now been flown. Despite efforts to develop a follow on mission for CERES [*Georgieva et al.*, 2015], there is currently no funded mission to sustain the crucial EOR record beyond CERES.

Table 1.1. Selected satellite measurements that have made substantial contributions to ERB science.

Launch	Instrument	Satellite(s)	Noteworthy contributions to ERB science
1959	N/A	Explorer VII	First EOR satellite observations
1975	ERB	Nimbus 6 and 7	First complete ERB instrument, measuring all three components
1984	ERBE	ERBS, NOAA 9 and 10	First multi-satellite system designed to measure ERB
1997	CERES	TRMM, Aqua, Terra, Suomi-NPP, JPSS-1	Continuing to provide over two decades of EOR observations with higher accuracy and precision than any preceding observations
2002	GERB	Meteosat 8, 9, 10, and 11	High frequency observations that reveal diurnal EOR over a large region

Finally, during the CERES record, the Geostationary ERB (GERB) mission was also launched [*Harries et al.*, 2005]. The GERB mission has distinctly different scientific objectives from the preceding missions. The geostationary orbit of GERB does not permit global coverage but, instead, provides frequent observations over the same region that reveal the detailed diurnal variability in EOR over that region. Studies using GERB observations have demonstrated the process level understanding that can be obtained from high frequency observations, as will be discussed further in Sect. 1.1.3. A detailed discussion of all recent EOR observations is provided by *Dewitte and Clerbaux* [2017]. A summary of key missions is provided in Table 1.1.

1.1.3 Scientific relevance

The early EOR satellite observations drastically advanced our understanding of fundamental climate parameters. For example, early satellite estimates of the planetary albedo of 30 % [*Vonder Haar and Suomi*, 1971] are similar to today's best estimates of 29 % from CERES [*Wielicki et al.*, 1996], but substantially lower than pre-satellite estimates ranging between 32 and 50 % [*Dines*, 1917; *London*, 1957]. Similarly, early satellite estimates of the OLR revealed the magnitude of the greenhouse effect to be about 150 W m^{-2} [*Dickinson*, 1985], calculated as the difference between 390 W m^{-2}, the emission from a globally averaged surface temperature of 15 °C, and 237 W m^{-2}, the observed globally averaged OLR. Perhaps most importantly, the extended spatial coverage provided by satellites quantified the regional distribution of energy imbalances, and therefore outlined the drivers of the general circulation in the atmosphere and ocean [*Rasool and Prabhakara*, 1966; *Charney*, 1975].

More recently, EOR observations have played a crucial role in studying climate forcing and feedbacks [e.g., *Futyan et al.*, 2005; *Loeb et al.*, 2007; *Brindley and Russell*, 2009; *Dessler*, 2013; *Ansell et al.*, 2014], global energy imbalance and its implication in the hydrological cycle [e.g., *Stephens et al.*, 2012; *Trenberth and Fasullo*, 2012; *Allan et al.*, 2014; *Hegerl et al.*, 2015], and in the development, improvement and validation of weather and climate models [e.g., *Forster and Gregory*, 2006; *Hartmann and Ceppi*, 2014]. However, substantial differences persist between observations of the TOA energy flows, and those represented by climate models (Fig. 1.2). A difference of 0.01 in albedo is equivalent to about 4 W m^{-2}, which is roughly the same as the forcing expected for a doubling of atmospheric carbon dioxide concentrations, so the

differences in Fig. 1.2 are not small. The CERES data shown in Fig. 1.2 are from a later time period of March 2000–December 2003, compared to the ERBE and model data which are from February 1985–May 1989, but that should not be a dominant factor in explaining the differences because *Stephens et al.* [2015] report that the inter-annual variability in global albedo is remarkably small. To further complicate matters, the climate models are "tuned" to agree better with the satellite observations by adjusting various model parameters [*Mauritsen et al.*, 2012], but precisely how this is achieved is often not made clear [*Hourdin et al.*, 2017].

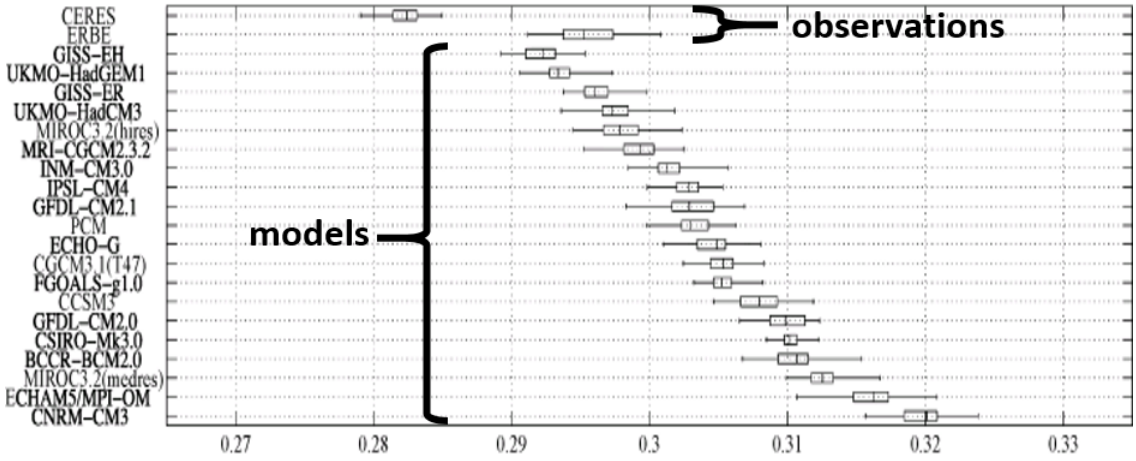

Figure 1.2. Earth's global mean monthly de-seasonalised albedo from satellite observations and Coupled Model Intercomparison Project Phase 3 climate models (adapted from *Bender et al.* [2006]).

The discrepancies between modelled and observed albedo are not simply a systematic offset at the global scale. Satellite observations indicate a remarkable symmetry in hemispheric albedo [*Ramanathan*, 1987; *Stephens et al.*, 2015] that is poorly represented by climate models (Fig. 1.3). The large spread in the extent to which different models represent the observed hemispherical albedo symmetry indicates a fundamental issue in the representation of radiative properties and processes in the models. Properly representing these processes could have important implications for eliminating longstanding model biases previously thought to be intractable [*Haywood et al.*, 2016]. This calls for EOR observations capable of capturing relevant variability at the process level.

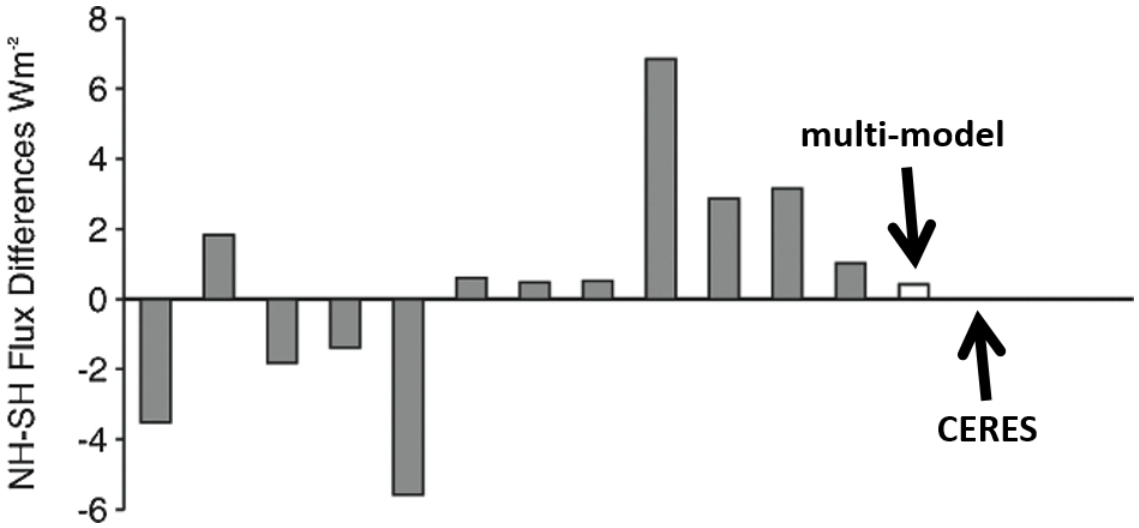

Figure 1.3. Northern Hemisphere (NH) minus Southern Hemisphere (SH) annual mean outgoing short-wave irradiance from climate models and satellite observations (adapted from *Stephens et al.* [2015]). Each grey bar represents a different model from the Coupled Model Intercomparison Project Phase 5. The white bar represents the multi-model mean. The absence of a bar associated with the Clouds and the Earth's Radiant Energy System (CERES) indicates hemispherical symmetry in albedo from satellite observations.

One way to observe EOR variability better is to make observations with high temporal resolution, because we know the underlying properties and processes controlling EOR variability evolve rapidly (e.g., cloud systems and large diurnal variations). Studies using GERB observations have demonstrated the value of high temporal resolution for understanding processes. For example, dominant diurnal patterns of OLR extracted over the GERB footprint have quantified the relative importance of processes such as surface heating and deep convective cloud development (Fig. 1.4). The range in the diurnal variations of OLR associated with these processes was found to be up to 80 W m^{-2}. This not only underlines the significance of diurnal processes for properly representing ERB variability, but also highlights the difficulty associated with making EOR observations from Sun-synchronous orbits with limited diurnal sampling. By under-sampling the diurnal variability, extreme care must be taken when adjusting the diurnally limited observations to obtain accurate long-term averages. Unfortunately, an EOR observing system that samples the diurnal variability explicitly at the global scale does not currently exist.

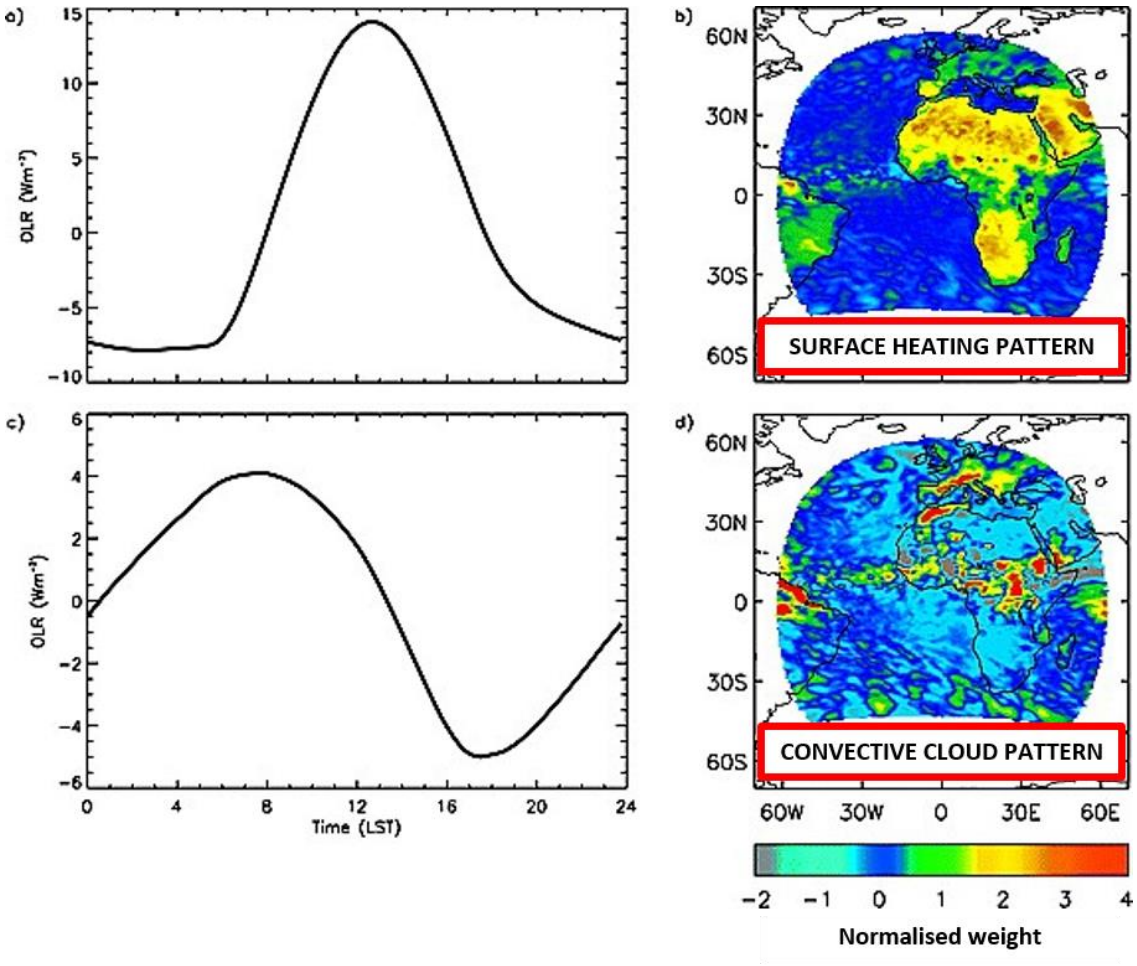

Figure 1.4. The two dominant patterns in the diurnal cycle of outgoing long-wave radiation (OLR) for July 2006, as observed by the Geostationary Earth Radiation Budget (GERB) instrument (adapted from *Comer et al.* [2007]). The principal components (a and c) represent the temporal variations during the diurnal cycle, and the empirical orthogonal functions (b and d) represent the corresponding spatial patterns associated with the diurnal variations.

Another way to capture ERB variability better is to make spectrally resolved observations. All of the previous ERB observations, as discussed in Sect. 1.1.2, have been based on observations that are broadband, or spectrally integrated. However, interactions between radiation and various aspects of the Earth-atmosphere system are typically wavelength specific. The spectrum of radiation emerging at TOA therefore contains a rich amount of information about the path through the Earth-Atmosphere system that the radiation has traversed. If the spectrum contains compensating features, they can be partly or fully masked in broadband observations, leading to a smaller signal of physical processes and their changes with climate [*Feldman et al.*, 2011a]. An

example of compensating spectral features can be seen by returning to the intriguing hemispherical albedo symmetry. Despite the symmetry in spectrally integrated albedo, the Northern Hemisphere is more reflective in the near-infrared due to high reflection in this part of the spectrum from the larger fraction of land mass, whereas the Southern Hemisphere is more reflective in the visible due to high reflection in this part of the spectrum from the larger fraction of cloud (Fig. 1.5). Although the value of spectral information for understanding the physical properties and processes involved has been widely demonstrated [*Brindley and Bantges*, 2016], it remains somewhat underutilised for ERB observations, and particularly for RSR.

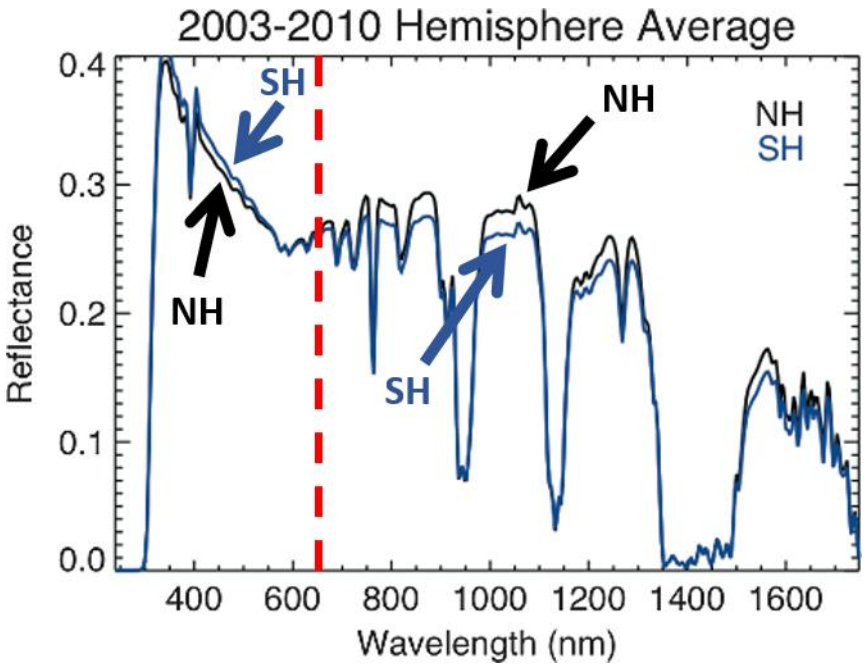

Figure 1.5. The hemispheric, annual averaged spectral reflectance as measured by the SCanning Imaging Absorption spectroMeter for Atmospheric CHartographY (SCIAMACHY) over the period 2003–2010 (adapted from *Stephens et al.* [2015]). The red dash line separates the spectrum at the visible/near infrared boundary, where dominance of the Northern Hemisphere (NH; black) and Southern Hemisphere (SH; blue) reverses.

1.2 Constellation concept

1.2.1 Opportunity presented by small satellites

Earth observation has traditionally been achieved by unique, sophisticated and expensive satellites, operated by large government backed space agencies. The focus of

these satellites has often been on measurement synergy from multiple instruments on large and heavy satellites, such as the 8.2 tonne Environmental Satellite (ENVISAT) from the European Space Agency (ESA) or the 4.9 tonne Terra satellite from the NASA. Although observations from these types of satellites have been instrumental in providing scientific advancements, it has been difficult to sustain and advance this traditional approach over the past decade or so given budget constraints. In addition, the observations provided by a single, or few, orbiting platforms have fundamental sampling restrictions that can limit the scientific value of the observations.

Recent advancements in small satellite technology [*Sandau et al.*, 2010] and sensor miniaturisation [*Barnhart et al.*, 2009] have offered an alternative approach: a novel, viable and sustainable sampling strategy from a constellation of satellites. The constellation approach has attracted enormous and increasing attention over the past decade, evidenced by almost 300 launched small satellites in 2017 [*Kulu*, 2018]. Instead of large government agencies, the small satellite industry is dominated by the private sector and universities, and has become popular for many reasons including:

- Reduced launch costs via secondary payload launches;
- Use of commercial-off-the-shelf components, reducing the cost of hardware development;
- Reduced risk, since failed satellites and instruments can be easily replaced;
- Rapid re-visit times from multiple small satellites.

Many of the small satellite developments in recent years have been centred on the CubeSat concept. A single unit or "1U" CubeSat is defined by a volume of 10 cm × 10 cm × 10 cm and a weight of 1.33 kg [*Puig-Suari et al.*, 2001]. Multiple 1U cubes can then be combined to produce larger systems. Although CubeSats were initially envisioned as educational tools or low-cost technology demonstration platforms, advanced small-satellite constellations for science are becoming commonplace [*Crisp et al.*, 2015]. For example, small-satellite constellations have been applied for monitoring surface wind speeds over oceans and within tropical cyclones [*Ruf et al.*, 2012], surface albedo [*Nag et al.*, 2015], and providing surface imagery for natural disaster monitoring [*Underwood et al.*, 2005]. An extensive list of small-satellite missions is provided by *Poghosyan and Golkar* [2017]. The growing number of small

satellite constellations for science applications has exposed the high scientific value that constellations of small satellites can provide.

1.2.2 Applicability to EOR measurements

Measurements of EOR are the ideal candidate for a satellite constellation. The improved sampling from a constellation would complete the ERBE and GERB visions by providing global scale EOR observations from multiple satellites whilst also capturing diurnal variability. This has been pointed out previously by *Wiscombe and Chiu* [2013] who argued the case for broadband WFOV radiometers to be hosted on the Iridium satellite constellation for the measurement of EOR.

Unfortunately, EOR observations were not funded for inclusion on the Iridium satellite constellation. However, development of instrumentation, similar to what would have been included on the Iridium satellites, went ahead in the form of the Radiometer Assessment using Vertically Aligned Nanotubes (RAVAN) [*Swartz et al.*, 2015]. The RAVAN instrument incorporates two key technologies. The first is a new radiometer material consisting of vertically aligned carbon nanotubes which are amongst the blackest and most spectrally flat absorbers known. The second is a calibration source consisting of a gallium blackbody that serves as a stable and repeatable reference to track sensor degradation. A single RAVAN instrument was launched on a 3U CubeSat as a technology demonstration on 11th November 2016 (Fig. 1.6a). The first results that are currently emerging from RAVAN suggest that the different channels of the radiometer are in excellent agreement, and the calibration source is responding as expected [*Swartz et al.*, 2017].

In addition to the broadband RAVAN instrument, miniaturised spectrometers have also been considered for various applications such as cloud thermodynamic phase; fire fuel, combustion, burn severity, and recovery; cryospheric albedo, energy balance, and melting; and more [*Green et al.*, 2017]. The level of maturity of a spectrally resolved CubeSat instrument specifically designed to measure EOR is undoubtedly somewhat behind that of its broadband counterpart. However, it is certainly not inconceivable that an EOR spectrometer suitable for deployment on a constellation of CubeSats could be developed in the coming years.

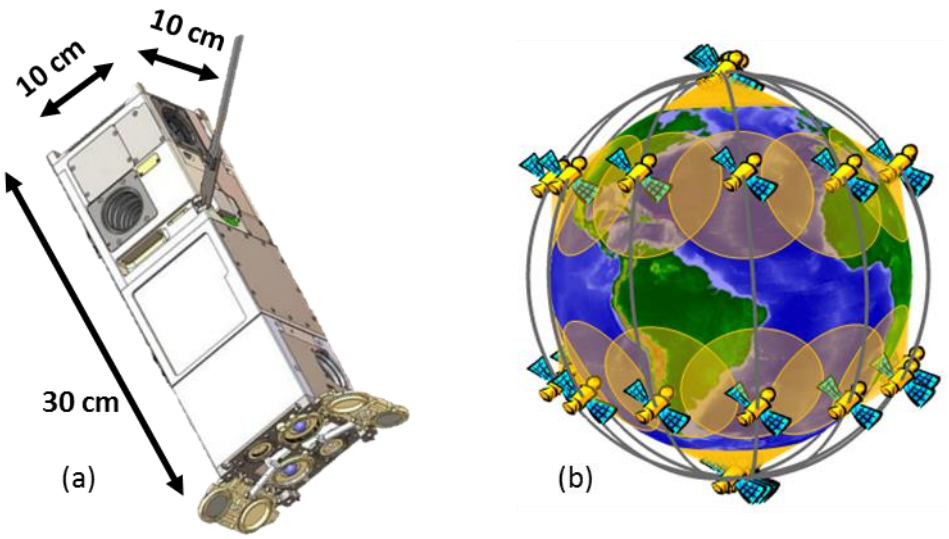

Figure 1.6. (a) The Radiometer Assessment using Vertically Aligned Nanotubes (RAVAN) CubeSat (adapted from *Swartz et al.* [2015]). (b) Snapshot of a possible constellation of 36 CubeSats orbiting the Earth.

The promising results from the RAVAN in-orbit demonstration, and the additional potential of spectrally resolved observations, pave the way for a CubeSat constellation for EOR to be launched in the future (e.g., Fig. 1.6b). As well as demonstration of the required technology, a clear science case must be put forward. It therefore remains to fully demonstrate the scientific potential of the constellation approach for EOR observations.

1.3 Thesis objective and proposed science questions

In light of sampling deficiencies in current EOR satellite observations, and recent technological advances in small satellite technology and sensor miniaturisation, the primary objective of this thesis is to determine the extent to which a constellation of small satellites could enhance global EOR observations. This will include exploration of the associated science that such observations could provide.

Firstly, to evaluate the potential of the constellation concept, and to investigate the configuration requirement for measuring radiation at a time resolution sufficient to resolve the diurnal cycle for weather and climate studies, a new recovery method is developed, and a series of simulation experiments are conducted. These simulation

experiments are the subject of Chapter 2, and are performed to answer the following science question:

Science question 1. Can a feasible constellation of satellites enhance observations of Earth's outgoing energy flows?

Secondly, a satellite constellation could potentially reveal the diurnal cycle of EOR at the global scale, but it is unclear what the underlying processes controlling this diurnal variability are. To provide insights into the dominant processes controlling the diurnal cycle of EOR at a global scale, high frequency output from a global Numerical Weather Prediction (NWP) model of EOR and other relevant model variables is analysed in detail. This analysis of NWP model output is the subject of Chapter 3, and seeks to answer the following science question:

Science question 2. What controls the diurnal cycle of global outgoing radiation?

Thirdly, although the value of spectrally resolved EOR has been identified previously, a way that the entire spectrum of information can be used to understand physical properties leading to variability in EOR, and track changes in those properties, has not been provided. Given that the spectral dimension is most underutilised for RSR, spectral signatures of RSR are extracted from computed reflectance spectra using observationally based atmospheric and surface properties, and a route forward is provided for mapping between the spectral signatures that could be observed by a future satellite constellation and the contributing properties. The spectral signatures and their contributing properties are the subject of Chapter 4, and are formulated to answer the following science question:

Science question 3. How can spectrally resolved outgoing short-wave radiation be used to fingerprint the Earth system?

2 CHAPTER TWO: Determination of global Earth outgoing radiation at high temporal resolution using a theoretical constellation of satellites

2.0 Statement of publication status

The material in this chapter was published in the Journal of Geophysical Research: Atmospheres on 21st January 2017. I am the lead author of the manuscript. All figures and tables were generated by myself, and I led and finalised the scientific writing. I take full responsibility for the results. Other authors listed on this publication helped in the supply of model data, were involved in discussions of the methods and provided valuable feedback on the results. The published manuscript can be found at the following reference:

Gristey, J. J., J. C. Chiu, R. J. Gurney, S.-C. Han, and C. J. Morcrette. (2017). Determination of global Earth outgoing radiation at high temporal resolution using a theoretical constellation of satellites. *Journal of Geophysical Research: Atmospheres*, **122(2)**, 1114–1131. https://doi.org/10.1002/2016JD025514

The content of this chapter differs from the published article in the following ways:

- The published abstract is moved to the end of the chapter to provide a concise summary;
- The published conclusions and summary are excluded from this chapter and are incorporated into Chapter 5;
- For consistency with the thesis structure, the numbers of the section headings, equations, figures and tables are updated, and minor format changes are applied;
- American English spellings are changed to British English.

Note that the published introduction included in this chapter contains minor overlaps with Chapter 1, but is included in its original form for completeness.

2.1 Introduction

The Earth reflects part of the incoming solar radiation back to space and responds to the remaining absorbed energy by adjusting its temperature and emitting thermal infrared

radiation out to space. Observing these energy flows exiting the top-of-the-atmosphere (TOA), referred to as Earth outgoing radiation (EOR), has advanced our understanding of fundamental climate parameters such as the planetary brightness [*Vonder Haar and Suomi*, 1971], the greenhouse effect [*Dickinson*, 1985], and the zonal and meridional heat transports required by the atmosphere and ocean to redistribute regional energy imbalances [*Rasool and Prabhakara*, 1966; *Charney*, 1975]. EOR observations also play a crucial role in studying climate forcing and feedbacks [*Futyan et al.*, 2005; *Loeb et al.*, 2007; *Brindley and Russell*, 2009; *Ansell et al.*, 2014], global energy imbalance and its implication in the hydrological cycle [*Stephens et al.*, 2012; *Trenberth and Fasullo*, 2012; *Allan et al.*, 2014; *Hegerl et al.*, 2015], and in the development, improvement, and validation of weather and climate models [*Forster and Gregory*, 2006].

Measurements of EOR have been made from dedicated missions since 1975; examples include the early ERB experiments [*Smith et al.*, 1977; *Barkstrom*, 1984; *Kyle et al.*, 1993], the current Clouds and the Earth's Radiant Energy System (CERES) [*Wielicki et al.*, 1996], and the Geostationary ERB (GERB) experiment [*Harries et al.*, 2005]. CERES has proven invaluable for studying global energy balance; the uncertainty on the monthly net TOA irradiance determined from CERES ranges from –2.1 to 6.7 W m^{-2} [*Loeb et al.*, 2009]. Improved absolute accuracy is attainted by incorporating ocean heat content observations [*Lyman et al.*, 2010; *Church et al.*, 2011]. Unlike CERES, operated mainly in Sun-synchronous orbits, the geostationary capability of GERB provides outgoing radiation products at a 15 min temporal resolution, but over the European and African continents and surrounding areas only.

Since radiation shows distinct diurnal signatures directly linked to the evolution of weather and climate system processes, CERES and geostationary satellite observations have been combined to generate a temporally interpolated data set [*Doelling et al.*, 2013, 2016] that has been used in studies of cloud and aerosol radiative forcing [*Taylor*, 2012], explaining TOA diurnal cycle variability [*Taylor*, 2014; *Dodson and Taylor*, 2016], and to make comparisons with models and reanalyses [*Itterly and Taylor*, 2014; *Hill et al.*, 2016]. However, incorporating different geostationary observations with unique sensor characteristics and varying degrees of quality can produce significant artefacts resulting in unnatural spatial patterns in radiation fields [*Doelling et al.*, 2013]. It is clear that current missions are not designed for these high temporal resolution

applications, despite the apparent need for global EOR at high temporal resolution, preferably sufficient for resolving the diurnal cycle.

Such EOR measurements require a new observation strategy. Recently, because of a technology revolution in small satellites and sensor miniaturisation [*Sandau et al.*, 2010], a constellation approach has drawn considerable attention and has been applied in monitoring surface wind speeds over oceans and within tropical cyclones [*Komjathy et al.*, 2000; *Ruf et al.*, 2012], surface albedo [*Nag et al.*, 2015], and providing surface imagery for natural disaster monitoring [*Underwood et al.*, 2005]. Its potential for providing high temporal resolution EOR observations, however, has not been fully explored.

This paper aims to evaluate whether the new constellation concept can potentially provide an EOR observational data set with high temporal resolution and accuracy for weather and climate studies and to identify the key factors affecting the performance of the constellation. While various advanced sensors like scanning narrow field-of-view (FOV) radiometers can be potential candidates for a constellation, we focus on applications using wide FOV (WFOV) broadband radiometers. This type of sensor is low cost and, more importantly, has features preferable for any Earth radiation budget mission, such as mature instrumentation technology and no moving parts.

WFOV measurements have proven invaluable for monitoring planetary EOR [*Smith et al.*, 1977; *Barkstrom*, 1984; *Kyle et al.*, 1993], but their large footprint size makes it less straightforward to obtain EOR at a synoptic scale. To enhance the spatial resolution of WFOV observations, *Hucek et al.* [1987, 1990] applied spherical harmonic analysis to 6 day measurements of a single WFOV radiometer and showed significant improvement not only in spatial resolution but also in the root-mean-square error (RMSE) of the global mean albedo. Their recovery analysis greatly enhanced the EOR product from monthly mean to weekly mean; however, the enhancement reached a limit, because a time interval of 6 days was necessary to accumulate sufficient instantaneous measurements from a single radiometer. Clearly, an increase of available satellites using a constellation can help push this time limit further and enhance the temporal resolution, but it is unclear what the required configuration of the constellation will be if we aim to observe EOR hourly to monitor fast evolving systems such as dust storms and cyclones in the tropics and extra-tropics. An enhanced ability

to track these systems allows us to capture their evolution and understand the underlying radiative processes, further constraining future warming of our climate system.

We will perform extensive simulation experiments to explore the capability of the constellation concept for observing EOR. Similarly to *Hucek et al.* [1987, 1990], *Han et al.* [2008], and *Salby* [1988a, 1988b], we use spherical harmonic analysis for detailed EOR recovery from WFOV measurements, but necessarily, different constraints are applied to make the recovery work for a much higher temporal resolution. In this paper, Sect. 2.2 details the recovery method and the design of simulation experiments, while Sect. 2.3 presents the results from a baseline constellation and related sensitivity tests. Finally, Sect. 2.4 provides a brief summary of our key findings.

2.2 Simulation experiment for recovering irradiance fields

2.2.1 Simulation of measurements

To develop and evaluate our recovery method, synthetic data sets were generated using output from the Met Office global numerical weather prediction (NWP) model [*Walters et al.*, 2014]. The model was run from an operational 00 Z analysis using 1024 longitudinal and 769 latitudinal grid points, with a coarsest spatial resolution of approximately 39 km × 26 km along the equator. Normally, the time step used for global NWP with this configuration is 12 min and for reasons of computational expense, full radiation calculations are only done every hour [*Manners et al.*, 2009]. In this simulation, however, the time step was reduced to 5 min and, to represent evolution of the radiation fields better, the radiation scheme [*Edwards and Slingo*, 1996] was called on every one of those time steps. Arbitrarily, we chose a 1 day model output from 12 Z on 28 August 2010 (T + 12 to T + 36) to simulate satellite WFOV measurements for our experiment. Figure 2.1 shows an example of the modelled outgoing short-wave (SW) and long-wave (LW) irradiance fields at the TOA of 80 km, for 00 Z on 29 August 2010. These irradiance fields contain clear structures associated with meteorological phenomena including large regions of tropical convection in the central and western Pacific and a mid-latitude frontal system in the northern Pacific. Meteorological phenomena of this type are large in spatial scale (~1000 km), evolve quickly (approximately hourly) and appear to dominate the variability of the outgoing

irradiance fields, and will therefore be of interest to observe when recovering outgoing irradiance fields.

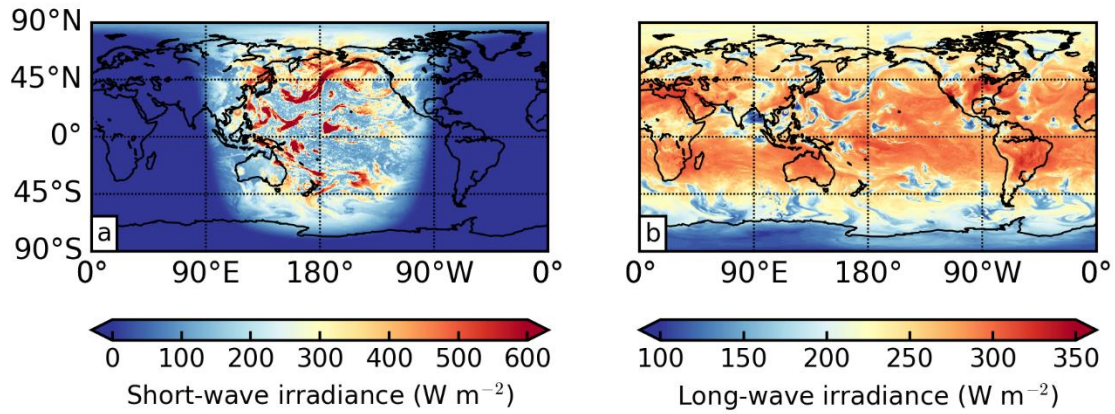

Figure 2.1. Simulated outgoing (a) short-wave and (b) long-wave irradiance at the top-of-the-atmosphere at 00 Z on 29 August 2010 from the Met Office global numerical weather prediction model. The model resolution is 0.35° in longitude and 0.23° in latitude.

Using these modelled irradiance fields, the instantaneous irradiance measured by each satellite, F_{sat}, at colatitude θ and longitude λ, is then the integration of radiation received from all points within the WFOV, given as

$$F_{sat}(\theta,\lambda) = \int_{\Omega(\theta,\lambda)} I_{TOA}(\theta',\lambda')\, A(\theta,\lambda,\theta',\lambda') \cos\beta \, d\Omega' + e, \qquad (2.1)$$

where $I_{TOA}(\theta',\lambda')$ is the radiance reaching the satellite from TOA location (θ',λ') within the satellite FOV Ω, $A(\theta,\lambda,\theta',\lambda')$ is a factor to account for the laboratory-measured angular response of the instrument, β is the angle between the satellite nadir and the line of satellite to location (θ',λ'), and e represents systematic and random instrument error, which is investigated in Sect. 2.3.2.2. For the sake of simplicity, we assume that the instrument has a flat spectral response that is insensitive to the spectral composition of the observed scene and a flat angular response to omit $A(\theta,\lambda,\theta',\lambda')$ from hereon in. Since the model output provides irradiance rather than radiance, I_{TOA} were generated using an isotropic assumption. In other words, Eq. (2.1) can now be rewritten as

$$F_{sat}(\theta,\lambda) = \int_{\Omega(\theta,\lambda)} \frac{F_{TOA}(\theta',\lambda')}{\pi} \cos\beta \, d\Omega' + e, \qquad (2.2)$$

where F_{TOA} is the instantaneous outgoing irradiance at the TOA. This assumption inevitably introduces uncertainty in the recovery, which will be evaluated in Sect. 2.3.2.1 using angular distribution models (ADMs) from the CERES [*Loeb et al.*, 2003].

Using Eq. (2.2), synthetic measurements are generated at the sampling rate of the satellite instruments. At each time step, a satellite will have progressed through space, giving a different value of θ and λ and thus a different FOV and F_{sat}. This forms nonuniformly distributed yet dense satellite measurements, which rely on spherical harmonic analysis to recover the global distribution of the outgoing irradiance field, as explained next.

2.2.2 Recovery method

Spherical harmonic analysis serves as a homogenisation of multiplatform observations to provide the complete distribution of the irradiance field on the entire Earth. This distribution can then be used to interpolate the irradiance field to smaller scales by optimally exploiting the dense measurements. At a given location (θ, λ), F_{TOA} can be represented exactly by a spherical harmonic series as

$$F_{TOA}(\theta,\lambda) = \sum_{l=0}^{\infty}\sum_{m=0}^{l}[C_{lm}Y_{lm}^{C}(\theta,\lambda) + S_{lm}Y_{lm}^{S}(\theta,\lambda)], \quad (2.3)$$

or be approximated by a truncated series as

$$F_{TOA}(\theta,\lambda) \approx \sum_{l=0}^{L}\sum_{m=0}^{l}[C_{lm}Y_{lm}^{C}(\theta,\lambda) + S_{lm}Y_{lm}^{S}(\theta,\lambda)], \quad (2.4)$$

where L is the truncation limit, leading to $(L + 1)^2$ terms on the right-hand side. The spherical harmonic functions Y_{lm}^{C} and Y_{lm}^{S} represent the spatial distribution, defined as

$$Y_{lm}^{C}(\theta,\lambda) = P_{lm}(\cos\theta)\cos m\lambda;$$

$$Y_{lm}^{S}(\theta,\lambda) = P_{lm}(\cos\theta)\sin m\lambda, \quad (2.5)$$

where P_{lm} is the associated Legendre function. The coefficients S_{l0} are always zero, while the first term containing the harmonic coefficient C_{00} finds the global mean outgoing irradiance. In contrast, the higher degree harmonics, C_{lm} and S_{lm}, represent the amplitude of structures at finer resolutions. Denoting R_E as the Earth radius, the subscript l represents structures at a wavelength of $2\pi R_E/l$ in spherical harmonic

analysis and thus a resolution (half of the wavelength) of approximately 20,000/l km. In other words, the spatial resolution of the recovered irradiance field is determined by the truncation limit L; a value of 20 leads to a resolution of 1000 km, recovered from 441 (i.e., $(L + 1)^2$) spherical harmonic coefficients.

Substituting Eq. (2.4) into Eq. (2.2) gives

$$F_{sat}(\theta,\lambda) = \int_{\Omega(\theta,\lambda)} \sum_{l=0}^{L} \sum_{m=0}^{l} [C_{lm} Y_{lm}^{C}(\theta',\lambda') + S_{lm} Y_{lm}^{S}(\theta',\lambda')] \frac{\cos\beta}{\pi}\, d\Omega' + e,$$

$$= \sum_{l=0}^{L} \sum_{m=0}^{l} \left[C_{lm} \int_{\Omega(\theta,\lambda)} Y_{lm}^{C}(\theta',\lambda') \frac{\cos\beta}{\pi} d\Omega' + S_{lm} \int_{\Omega(\theta,\lambda)} Y_{lm}^{S}(\theta',\lambda') \frac{\cos\beta}{\pi} d\Omega' \right] + e,$$

$$= \sum_{l=0}^{L} \sum_{m=0}^{l} [C_{lm} \bar{Y}_{lm}^{C}(\theta,\lambda) + S_{lm} \bar{Y}_{lm}^{S}(\theta,\lambda)] + e, \qquad (2.6)$$

where the truncation inequality has been dropped; $\bar{Y}_{lm}^{C}$ and $\bar{Y}_{lm}^{S}$ represent the spatially integrated spherical harmonic functions within the WFOV and respectively relate to Y_{lm}^{C} and Y_{lm}^{S} in Eq. (2.5) by

$$\bar{Y}_{lm}^{C}(\theta,\lambda) = \int_{\Omega(\theta,\lambda)} Y_{lm}^{C}(\theta',\lambda') \frac{\cos\beta}{\pi}\, d\Omega';$$

$$\bar{Y}_{lm}^{S}(\theta,\lambda) = \int_{\Omega(\theta,\lambda)} Y_{lm}^{S}(\theta',\lambda') \frac{\cos\beta}{\pi}\, d\Omega'. \qquad (2.7)$$

For M satellite measurements, Eq. (2.6) becomes a system of equations and can be written in matrix form as

$$\boldsymbol{F_{sat}} = \bar{\boldsymbol{Y}}\boldsymbol{c} + \boldsymbol{e}, \qquad (2.8)$$

where $\boldsymbol{F_{sat}}$ is a M × 1 matrix comprising all satellite measurements, $\bar{\boldsymbol{Y}}$ is a M × N matrix containing N number of the spatially integrated functions (i.e., $\bar{Y}_{lm}^{C}$ and $\bar{Y}_{lm}^{S}$) for each simulated satellite measurement, $\boldsymbol{c}$ is a N × 1 matrix comprising the unknown coefficients C_{lm} and S_{lm}, and $\boldsymbol{e}$ is a M × 1 matrix containing the measurement errors. Using a constrained least squares approach, an estimate of $\boldsymbol{c}$ in Eq. (2.8), $\hat{\boldsymbol{c}}$, is given by

$$\hat{\boldsymbol{c}} = (\overline{\boldsymbol{Y}}^T\overline{\boldsymbol{Y}} + \varepsilon^2\boldsymbol{I})^{-1}\,\overline{\boldsymbol{Y}}^T\boldsymbol{F_{sat}}, \tag{2.9}$$

where ε^2 is empirically chosen to be 10^{-4} and $\boldsymbol{I}$ is an N × N identity matrix. The ε^2 factor was chosen to be large enough to improve the condition number of the normal matrix and therefore stabilise the solution, while being 6 orders of magnitude smaller than the mean of the simulated satellite measurements and therefore not introduce significant bias in the recovery. Once Eq. (2.9) is solved, we place the coefficients, $\hat{\boldsymbol{c}}$, back into Eq. (2.4) to recover the TOA outgoing SW or LW irradiance $\hat{F}_{TOA}(\theta,\lambda)$ for all global locations.

Assuming that the errors in $\boldsymbol{F_{sat}}$ are uncorrelated and have constant variance σ^2, the variance-covariance matrix of $\hat{\boldsymbol{c}}$ can be given as [*Hastie et al.*, 2009, p. 47]

$$\mathrm{var}(\hat{\boldsymbol{c}}) = (\overline{\boldsymbol{Y}}^T\overline{\boldsymbol{Y}} + \varepsilon^2\boldsymbol{I})^{-1}\sigma^2, \tag{2.10}$$

where

$$\sigma^2 = \frac{1}{M-N-1}\sum_{i=1}^{M}\left(\boldsymbol{F_{sat}} - \hat{\boldsymbol{F}}_{\boldsymbol{sat}}\right)^2, \tag{2.11}$$

and

$$\hat{\boldsymbol{F}}_{\boldsymbol{sat}} = \overline{\boldsymbol{Y}}\hat{\boldsymbol{c}} + \boldsymbol{e}. \tag{2.12}$$

Then, the variance in the recovered outgoing irradiance field at each location (θ,λ) can be estimated by

$$\mathrm{var}\left(\hat{F}_{TOA}(\theta,\lambda)\right) = \boldsymbol{Y}(\theta,\lambda)\,\mathrm{var}(\hat{\boldsymbol{c}})\,\boldsymbol{Y}^T(\theta,\lambda), \tag{2.13}$$

where $\boldsymbol{Y}(\theta,\lambda)$ is a 1 × N matrix comprising the spherical harmonic functions Y_{lm}^C and Y_{lm}^S in Eq. (2.5), and the square root of it (i.e., the standard deviation representing about 68 % of the normal distribution) is used as the recovery uncertainty estimate.

Note that the spherical harmonic analysis above uses one set of matrices (i.e., Eq. (2.8)) to recover one irradiance field (i.e., Eq. (2.4)), which implicitly assumes that the irradiance field does not change during the analysis. This assumption is a particular concern for the SW spectral region, because SW irradiance fields evolve fast for two reasons. One is that the illuminated portion of the Earth changes rapidly due to Earth's rotation and solar geometry; the other is that albedo varies with changes in the radiative

properties of the atmosphere and surface. For a WFOV, the former is found to be the dominant factor for SW radiation evolution and needs to be incorporated into the recovery method. Therefore, instead of instantaneous satellite measurements, we used time-averaged values in Eq. (2.9) through the following process. For each WFOV satellite measurement, the instantaneous albedo, A_{INS}, is calculated as the ratio of this measurement and the instantaneous incoming solar irradiance over the WFOV. The average incoming solar irradiance within the measurement collection period (e.g., 1 h), $\bar{S}$, can be also calculated. The time-averaged satellite measurement in the SW, $F'_{sat,SW}$, can then be estimated by

$$F'_{sat,SW} = A_{INS}\bar{S}, \tag{2.14}$$

and the set of measurements generated in this way replaces $\boldsymbol{F_{sat}}$ in Eq. (2.9) when performing the recovery. The LW measurements remain unchanged.

2.2.3 Experiment design and setup

The configuration of a satellite constellation is defined by several parameters including the inclination angle, altitude, number of satellites, number of orbit planes, phasing of the satellites between planes, instrument sampling rate, and collection time period used to recover the irradiance field. While possible configurations can be unlimited, they unavoidably depend on launch opportunities, available finances, and, importantly, the required accuracy of the recovered irradiance.

To provide a general guideline, we focus on a baseline constellation configuration that consists of 36 satellites spread evenly across six orbital planes (Fig. 2.2a), with no phase difference between satellites in adjacent planes. Each orbital plane resides in an 86.4° non-Sun-synchronous orbit, allowing every satellite to precess throughout 24 h and provide coverage all the way to the poles, while maintaining plenty of separation to avoid any possibility of collision. The altitude of the satellites is chosen to be 780 km, the upper end of typical small satellite altitudes [*Maessen*, 2007; *Lücking et al.*, 2011]. This altitude enables a FOV as large as possible, corresponding to a horizon-horizon footprint of approximately 6000 km in diameter for an instrument FOV of 126°. For simplicity, we use circular orbits with all satellites at the same altitude, but the performance for varied satellite altitudes and other combinations of orbits is consistent given that the same sampling density shown in Fig. 2.2b is provided. Note that this

baseline configuration typically requires six launches, but it is possible to use fewer launches and let satellites drift and spread out, although it may take several months for satellites to reach the specified planes [*Bingham et al.*, 2008].

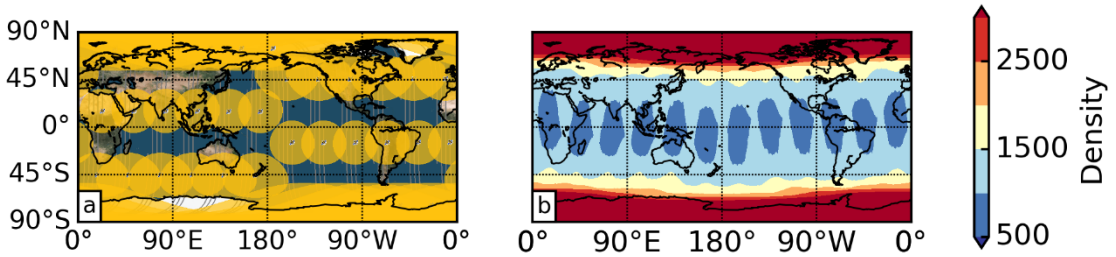

Figure 2.2. Sampling provided by the baseline constellation. (a) A snapshot of instantaneous sampling shows the ground tracks (lines) and footprints (circles) of each satellite. (b) The sampling density shows the accumulated number of times each grid point is "seen" by 5 s instantaneous measurements in a time interval of 1 h.

Additionally, we use a 5 s sampling rate to be consistent with past WFOV radiometer response times [*Hucek et al.*, 1987]. We also focus on measurements over a 1 h collection period because of the following trade-off. For scientific purposes, it is crucial to enhance our ability to observe the diurnal cycle of the global irradiance field; therefore, the collection time period must be as short as possible. However, in practice, it is necessary to accumulate sufficient measurements to provide dense global coverage that is required for the success of the recovery. To optimise this collection time period, we used the model output to examine how many times each grid point needs to fall within satellite's FOVs (i.e., to be seen by the satellites) to produce a stable recovery. As expected, the most challenging region is at lower latitudes. As shown in Fig. 2.2b, while it is not difficult to sample high-latitude regions densely, the sample size at low latitudes is at least 5 times smaller than that at high latitudes during a 1 h time period. Interestingly, several regions along the equator with small sample sizes somehow coincide with satellite ground tracks (see Fig. 2.2a), which is counterintuitive. The reason is that the "gaps" between satellite tracks have a better chance of being observed from both sides; in other words, the overlapping FOVs from satellites in adjacent orbital planes make the regions between tracks better sampled than those along the tracks. In general, we found that a minimum density of 500 samples is required for stable recovery, which can be achieved for the entire globe by a 1 h collection time

period as shown in Fig. 2.2b. A much longer duration is inappropriate because it would result in time aliasing, strongly violating the assumption of a static irradiance field as discussed in Sect. 2.2.2, and introduce a source of recovery instability.

The performance of the recovery method is measured by three metrics. In addition to commonly used global mean bias and RMSE, we also use the signal-to-noise ratio (SNR) from power spectra to quantify the recovery errors dependent on spatial resolution, investigate how fast the recovery errors increase with spatial resolution, and when the recovery noise becomes dominant and thus the recovery outcome is no longer reliable. For each spatial resolution, the SNR is defined as the ratio of the recovery amplitudes and error amplitudes. The average recovery amplitude associated with a spatial resolution of 20,000/l km, $A_{r,l}$, is given by

$$A_{r,l} = \sqrt{\sum_{m=0}^{l} [\hat{C}_{lm}{}^2 + \hat{S}_{lm}{}^2]}, \tag{2.15}$$

where $\hat{C}_{lm}$ and $\hat{S}_{lm}$ are the recovered coefficients in $\hat{\boldsymbol{c}}_{\boldsymbol{lm}}$ and the corresponding error amplitude, $A_{e,l}$, is calculated by

$$A_{e,l} = \sqrt{\sum_{m=0}^{l} [(C_{lm} - \hat{C}_{lm})^2 + (S_{lm} - \hat{S}_{lm})^2]}, \tag{2.16}$$

We used a value of SNR of unity to identify the spatial scale at which fast-evolving meteorological phenomena can be reliably recovered.

The performance of the baseline configuration is also used to compare and contrast recovery errors introduced by other factors, such as the number of satellites, the configuration of the satellites, instrument performance/calibration, and the isotropic assumption. We conducted a series of sensitivity tests to identify which of these factors play the most crucial roles and to provide guidelines about what needs to be considered when designing an optimal configuration.

2.3 Results

2.3.1 Recovered outgoing irradiance from the baseline constellation

The performance of the recovery method depends on the required spatial resolution. The SNR of the recovered irradiance field, calculated from the power spectra analysis in Fig. 2.3, generally decreases as the spatial resolution becomes finer. These variations are determined by the spatial structures in the radiation field and are therefore non-monotonic in nature. For example, the error at the largest planetary scales in the SW is relatively large due to the need to recover the position of the terminator. At a 1000 km spatial resolution, the SNR remains greater than unity in both the SW and the LW, suggesting that features of the atmosphere and surface are still recovered well at this resolution.

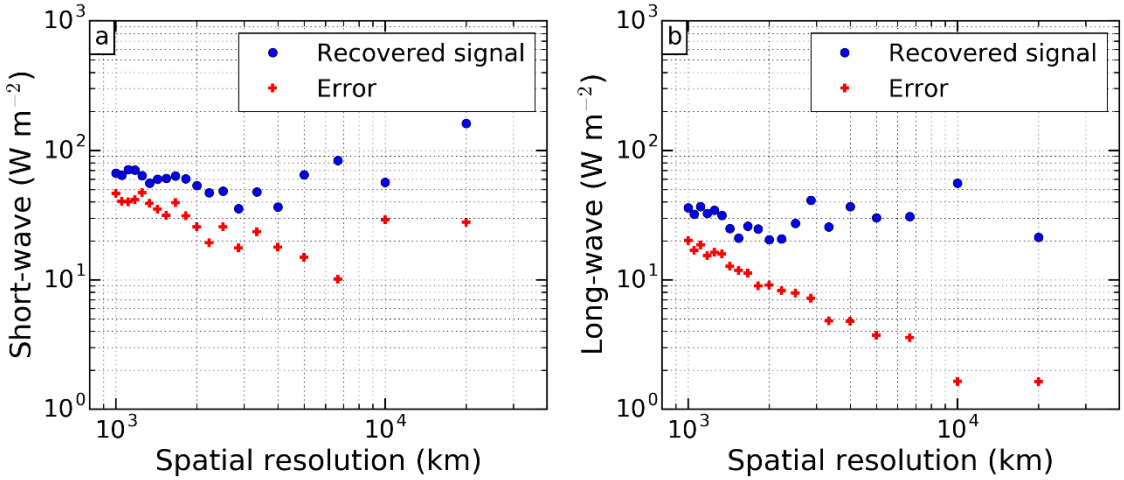

Figure 2.3. Power spectra of the recovered outgoing (a) short-wave and (b) long-wave irradiance at the top-of-the-atmosphere, based on a spherical harmonic analysis. The recovered signal (blue circles) is the amplitude of the recovery at varying spatial resolutions. The error (red crosses) is the difference between the amplitude of the recovery and the amplitude of the modelled "truth".

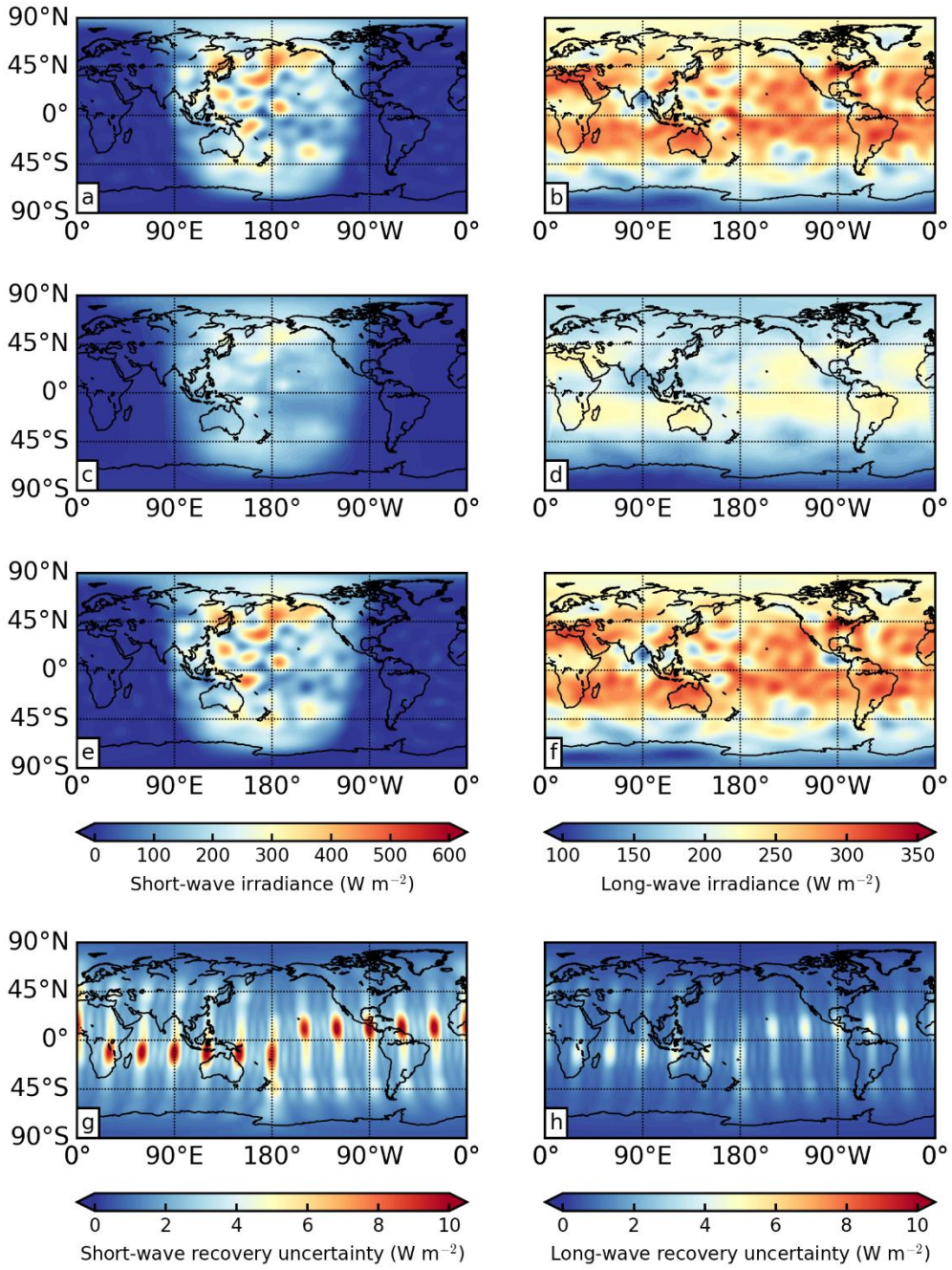

Figure 2.4. Maps of the outgoing (a, c, e, and g) short-wave and (b, d, f, and h) long-wave irradiance at the top-of-the-atmosphere at a 1000 km spatial resolution from 00 Z to 01 Z on 29 August 2010, based on a spherical harmonic analysis. (a) and (b) represent the truth, an average of 5 min irradiance fields from the Met Office model during this period. (c) and (d) represent the synthetic observations, linearly interpolated from the raw wide-field-of-view measurements onto the same grids as (a) and (b). The recovered irradiance from the synthetic observations is shown in (e) and (f), with associated uncertainty in (g) and (h).

Taking 1000 km resolution as an example, Fig. 2.4 shows the truth irradiance field averaged from the finer-resolution model output (i.e., Fig. 2.1) over the 1 h observation period, along with the synthetic WFOV satellite measurements and the recovery from the baseline constellation. As shown in Fig. 2.4a and b, although the truth irradiance field at a coarse resolution loses fine structures of the atmospheric systems, synoptic-scale features such as tropical cyclones in the central Pacific and mid-latitude frontal systems that were previously identified as dominant features of the outgoing irradiance field are retained. Due to the WFOV of the satellites, these features are not directly revealed in satellite measurements at the native resolution (Fig. 2.4c and d). However, once the spherical harmonic analysis is applied, the recovered irradiance fields (Fig. 2.4e and f) over a 1 h collection time period show a remarkable resemblance with the truth fields, which reconfirms the added value of performing the spherical harmonic analysis.

The uncertainty associated with the recovery is shown in Fig. 2.4g and h, which has a spatial distribution similar to that of the sample density in Fig. 2.2b. Interestingly, the regions with large recovery uncertainty do not coincide with the gaps of the sample density but fall between the gaps. Recall that the gaps of the sample density coincide with satellite ground tracks. Compared to the samples close to the edge of the FOV, nadir samples along the satellite track have much larger radiative contribution imparted to the WFOV measurement due to the cosine factor as seen in Eq. (2.1) and (2.2). Therefore, even though the corresponding sample density along the satellite tracks is relatively lower than neighboring regions, nadir radiation is retained well in WFOV observations and can be recovered with small uncertainty. In contrast, although regions between ground tracks are seen more frequently in the WFOV than along the tracks, their radiative contribution is small and thus the corresponding irradiance has larger uncertainty. Additionally, the regions with large recovery uncertainty in the Eastern Hemisphere are generally to the south of the equator, while those in the Western Hemisphere are to the north of the equator. This is as a result of sampling. Note that the satellites are going north in the Eastern Hemisphere and going south in the Western Hemisphere. Since all satellites have an orbital period longer than our collection time of 1 h and have not completed a full orbit yet, some regions are therefore not sampled as well as others, leading to larger recovery uncertainty.

We evaluate the recovery performance further via scatterplots and histograms of the recovery errors, calculated by subtracting the recovered outgoing irradiance from the truth on a 1000 km grid. Consistent with Fig. 2.4, the scatterplots in Fig. 2.5 show that the truth and the recovered outgoing irradiance are correlated well in the both SW and LW regions, and the majority of the data points fall onto the 1:1 line. Compared to the SW, the LW recovery errors in Fig. 2.5d are smaller (within 10 %), because the LW irradiance field is smoother and evolves more slowly, leading to less truncation error and time aliasing. As a result, the absolute errors in the LW recovery (Fig. 2.5f) are distributed more evenly around the globe but increase generally toward the equator as the magnitude of the outgoing LW irradiance increases. In contrast, while 94 % of recovery in the SW agrees with the truth within 25 % (Fig. 2.5c), Fig. 2.5e shows that large isolated errors can exist, particularly on the daylight side of the terminator and in the regions where tropical convection is common.

As shown in Fig. 2.4 and 2.5, the recovery errors are significantly larger than the estimated uncertainty, which calls into question the sources of the errors. To investigate the issues involved, we first looked into two convection systems that are associated with similar SW outgoing irradiance of over 600 W m^{-2} but have very different recovery errors (one less than 25 W m^{-2} and the other ~120 W m^{-2}). The case with small errors in Fig. 2.6a is mainly composed of an isolated convective system at the centre of the domain. There are many surrounding cloud bands, but they are small and far from the main convection system, leading to a good recovery in both location and magnitude. Unlike the case in Fig. 2.6a, the case with large errors in Fig. 2.6b is composed of many complex cloud systems that surround each other closely, making it difficult to capture the fine gaps between systems and to recover the exact boundaries of convections. Consequently, although the recovery is able to capture the main features of the truth, the magnitude and location of the main system centred at the domain are off, leading to large recovery errors surrounding the main convection system.

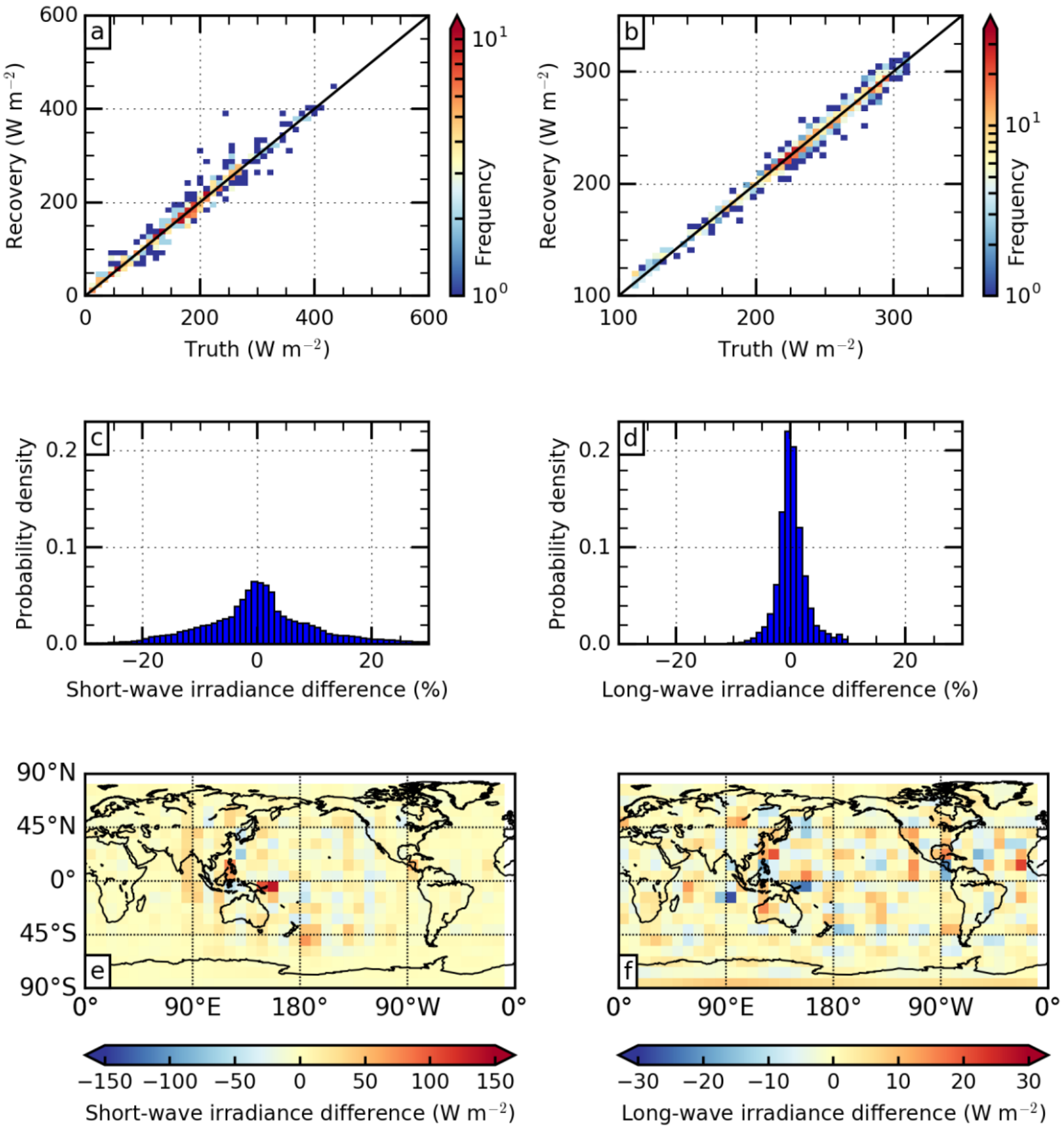

Figure 2.5. Error analysis of the recovered outgoing (a, c, and e) short-wave and (b, d, and f) long-wave irradiance at the top-of-the-atmosphere in Fig. 2.4. The scatterplots in (a) and (b) show the recovered versus the truth irradiance. The histograms in (c) and (d) represent the recovery errors (recovery minus the truth) relative to the truth as a percentage. The spatial distributions of the errors are mapped in (e) and (f).

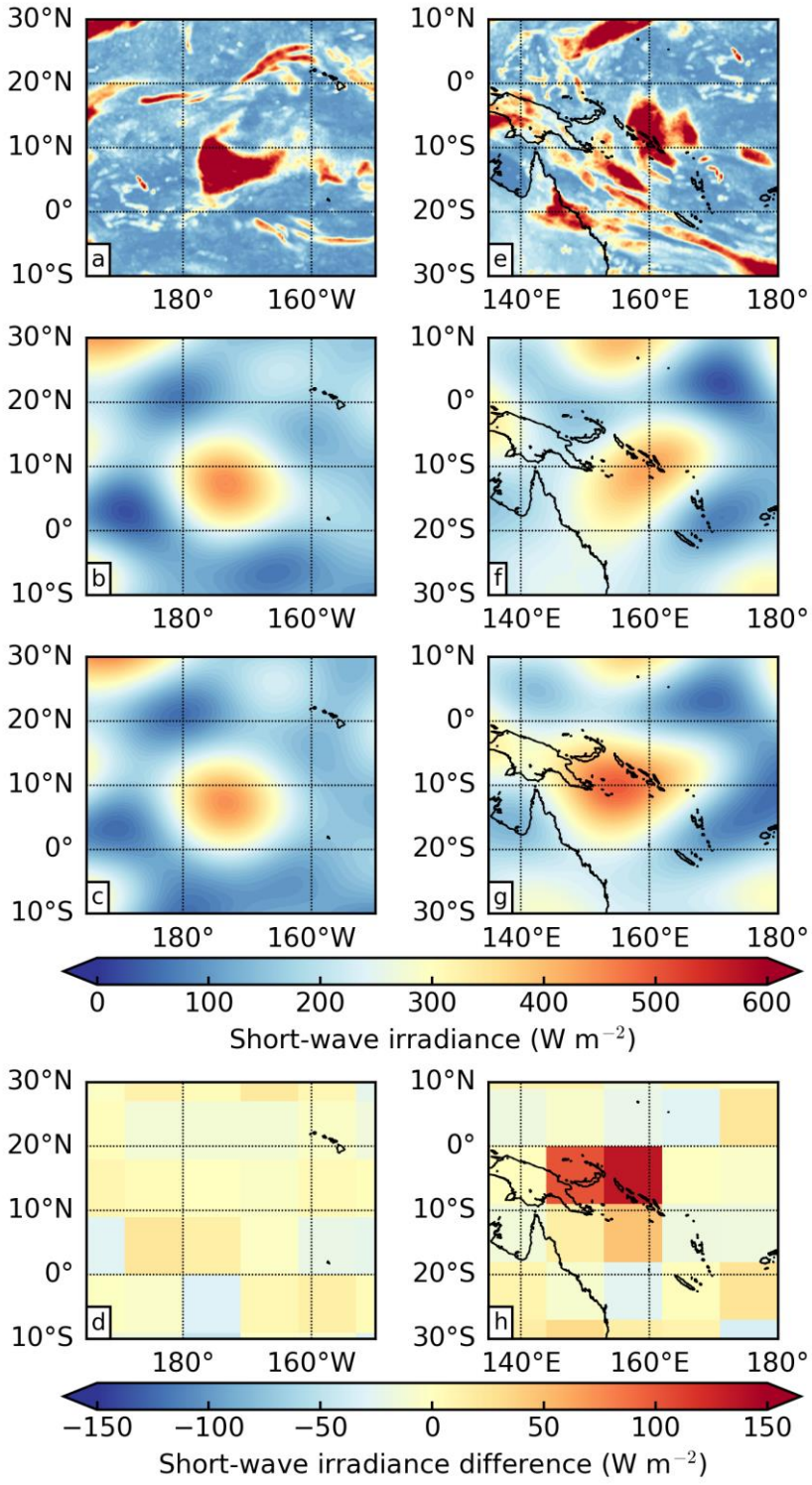

Figure 2.6. Zoom-in maps of the top-of-the-atmosphere outgoing short-wave irradiance fields extracted from the same case in Fig. 2.4 and 2.5 for two regions: (a–d) the central Pacific and (e–h) the west Pacific near Australia. Panels from top to bottom represent the truth SW irradiance at high resolution (~30 km), at low resolution (1000 km), the recovery at 1000 km, and the irradiance difference between the recovery and the truth.

These case studies indicate that the recovery includes two types of errors: one is the omission error that is owing to a limited spherical harmonic degree (i.e., a spatial resolution issue) and the other is the commission error mainly due to producing a static field from measurements collected over some finite time interval (i.e., a temporal resolution issue). To diagnose their relative impact on the recovery, the following experiments were performed. We started with a low resolution of 1000 km, static irradiance field (averaged over 1 h as shown in Fig. 2.4a and b) as input to simulate synthetic satellite measurements. As expected, this leads to an excellent recovery with negligible errors of less than 0.01 W m^{-2} for all grid points. We then put spatial complexity back into the input irradiance field by replacing the static, low-resolution field with a field averaged over 1 h at the original high resolution. The corresponding recovery (Fig. 2.7a) reveals similar errors to those found in Fig. 2.5e in the western and central Pacific region, suggesting that the spatial resolution is the primary issue for the large errors found in the daylight side of the terminator (except the edges). For the temporal resolution issue, we estimate the largest possible errors by taking the difference between 00 Z and 01 Z irradiance fields. As shown in Fig. 2.7c, the rapid change of ± 100 W m^{-2} in SW occurs not only on the edges of the terminator but also in the regions approximately 45° east and west extended from the edges, making the recovery prone to large commission errors. Note that we take an extreme estimate in Fig. 2.7c and d and that the actual errors are much less, as shown in Fig. 2.5e and f. Based on these analyses, adding low-inclination satellites to improve samples in the tropics and shortening the collection time period will be effective ways to reduce both the omission and commission errors.

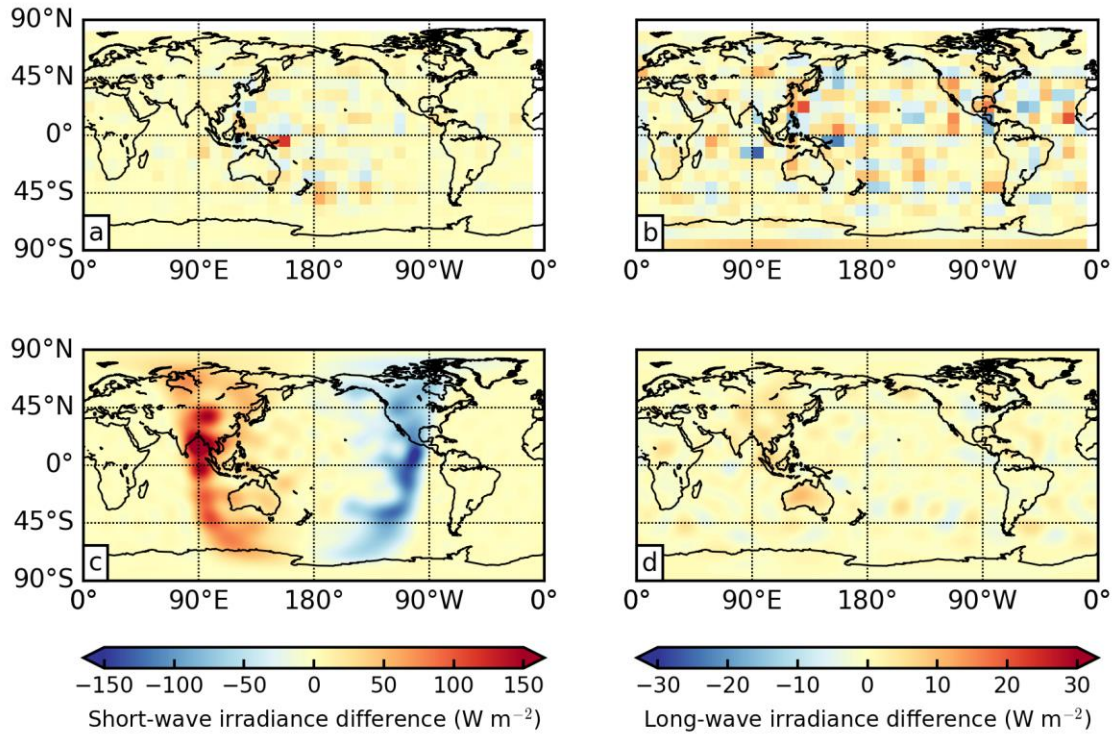

Figure 2.7. Spatial omission and temporal commission error analysis for the recovered (a and c) short-wave and (b and d) long-wave irradiance at the top-of-the-atmosphere in Fig. 2.4. The irradiance difference plots in (a) and (b) are the same as in Fig. 2.5e and f but using the 1 h averaged (i.e., static) high-resolution irradiance field to simulate satellite measurements, highlighting only spatial omission errors. The low-resolution (1000 km) truth irradiance difference between 00 Z and 01 Z shown in (c) and (d) highlights areas of high temporal commission errors.

The recovery errors over all grid points in Fig. 2.4e and f are 0.5 ± 16.4 and –0.02 ± 5.94 W m^{-2} (mean with one standard deviation) in the SW and LW, respectively. To examine whether the reported bias and errors for this particular time period are representative, Fig. 2.8 shows a 24 h time series of the hourly recovered SW and LW global mean biases. Recall that the previous results and discussions are based on the 1 h observations from 00 Z to 01 Z, around the middle of the time series in Fig. 2.8. Overall, on this day, the hourly global biases in the SW have a mean 0.16 W m^{-2} with a standard deviation of 0.45 W m^{-2}. For the LW, negative hourly biases dominate, and the hourly global biases have a mean of –0.13 W m^{-2} with a standard deviation of 0.15 W m^{-2}. These uncertainties are well below the current observational uncertainty for even the global annual means for the period 2000–2010 (respectively 2 W m^{-2} and 3.3

W m^{-2} in the SW and LW as shown in *Stephens et al.* [2012]), demonstrating that a constellation can potentially greatly enhance our capability to observe global EOR with much smaller uncertainty even at the hourly and daily time scale. However, the results from this experiment, which we will refer to as the control experiment, are clearly based on theoretical simulations containing some simplifying factors when compared with the real observational problem. To identify the factors that are most important in limiting the performance of the recovery method, including the assumption of isotropic radiation (Sect. 2.3.2.1), instrument performance (Sect. 2.3.2.2), and the number of satellites (Sect. 2.3.2.3), we next present results from a series of sensitivity tests.

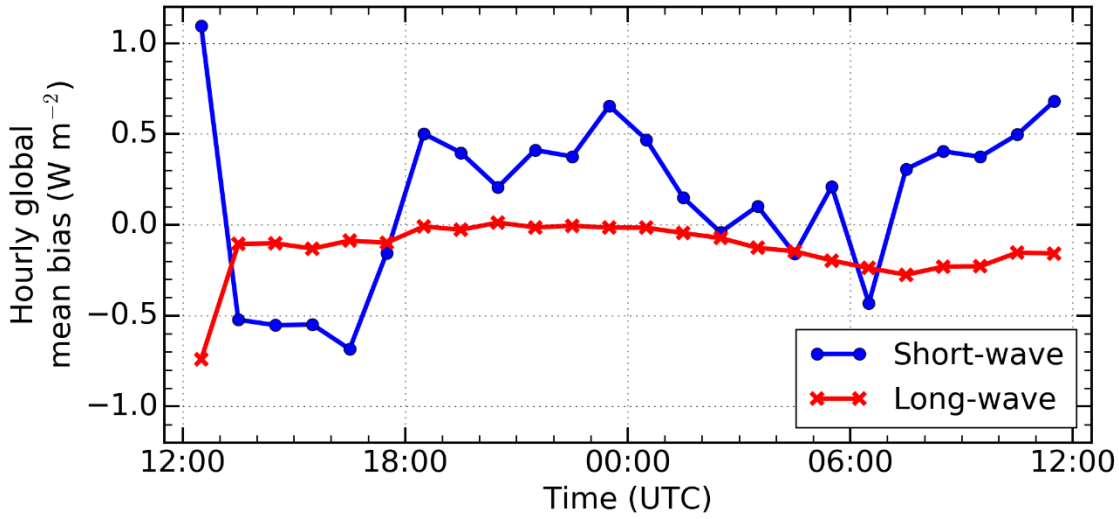

Figure 2.8. A 24 h time series of global mean bias in the hourly recovered short-wave and long-wave top-of-the-atmosphere outgoing irradiance fields, starting from 12 Z on 28 August 2010 to 12 Z on 29 August 2010.

2.3.2 Sensitivity tests

2.3.2.1 Assumption of isotropic radiation

As described in Sect. 2.2.1, an isotropic assumption was made to convert modelled irradiance output to radiance during the generation of the WFOV satellite measurements. To evaluate the magnitude of the recovery errors introduced by the isotropic assumption, we capitalise on the ADMs outlined by *Loeb et al.* [2003] to account for anisotropy in our synthetic satellite measurements. These ADMs consist of a set of anisotropic factors that empirically relate the isotropic radiance to that observed under certain conditions. In the SW, the anisotropic factors depend on the solar-viewing geometry, the surface type, and the meteorology of the scene (i.e., near-surface wind

speed, cloud phase, cloud optical depth, and cloud fraction) which we also obtain from the Met Office NWP model output. In the LW, anisotropic factors span a smaller range and are typically much closer to 1 [*Gupta et al.*, 1985], so we focus our attention on the SW here where the most serious consequences of making an isotropic assumption are likely to exist.

To include a more realistic radiance distribution, we simulate the 1 h set of measurements from the baseline constellation again but this time apply an appropriate anisotropic factor to each and every grid point within each WFOV measurement (i.e., insert this factor within the integral in Eq. (2.2)). We found that producing this new set of simulated measurements introduces a systematic bias to the measurements of 1.61 W m^{-2} which will of course hamper the recovery accuracy. To determine the origin of this bias, we simulated another set of measurements by randomly including the meteorology in the anisotropic factors to isolate the influence of meteorology and the viewing geometry. Those two sets of measurements are only offset by 0.10 W m^{-2} (Fig. 2.9a), suggesting the bias is largely related to the viewing geometry. We call the set of anisotropic factors that fully account for the scene meteorology "Full-ADM," and the set that randomly include the meteorology as "Random-ADM."

To alleviate the anisotropic issue, we perform the recovery on the simulated measurements using the Full-ADM (i.e., the most realistic estimate of what the measurements would be) but use the Random-ADM in the recovery process. This is a reasonable step to take since at any instant in time we will always know the solar-viewing geometry and surface type, even if simultaneous observations of the scene meteorology are not available. As shown in Fig. 2.9b and c, the SW anisotropic factors used in this experiment can change the radiance by more than a factor of 10 in extreme cases. However, the resulting bias in the hourly recovered global mean outgoing SW irradiance is just 0.56 W m^{-2} larger than the control experiment and is 0.93 W m^{-2} smaller than the experiment that uses Full-ADM measurements but isotropic radiation in the recovery process. Interestingly, this suggests that the instrument's WFOV of 6000 km in diameter encompasses such a large area that contains a range of meteorological regimes and makes the meteorological dependence of the ADM less critical for obtaining the hourly global mean. If one wishes to consider regional information, however, the errors increase significantly using the Random-ADM in the recovery process. In this case we recommend performing the recovery assuming that

the radiation is isotropic, which only increases the RMSE by 6 % compared to the control experiment. In practice, the regional error could be reduced by using climatological distributions of the meteorological variables or better still by incorporating the simultaneous meteorology using geostationary imagery or observations similar to the Moderate Resolution Imaging Spectroradiometer.

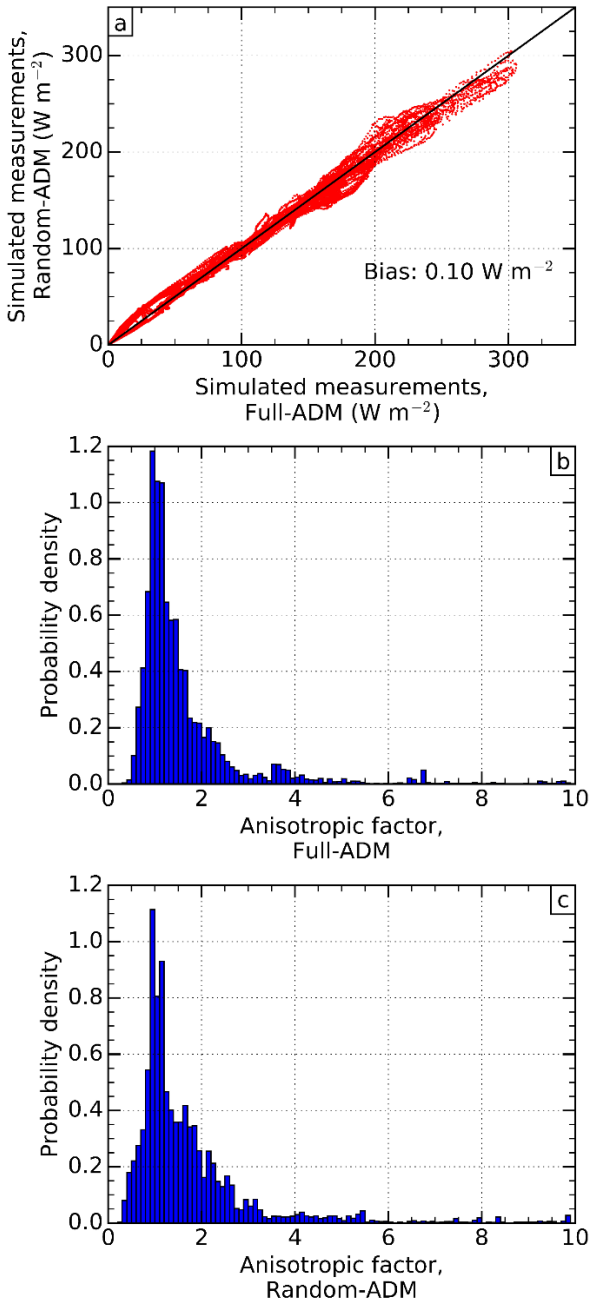

Figure 2.9. Simulated measurements from the baseline constellation using "Full-ADM" plotted against those using "Random-ADM" in (a), with the histograms of anisotropic factors applied in each case shown in (b) and (c), respectively. Greater than 98 % of the factors are contained in the range 0-10 shown.

Note that *Su et al.* [2015] have recently provided a new generation of ADMs. The new ADMs incorporate additional anisotropic effects, such as those of aerosols and sastrugi. Although the change in regional monthly mean instantaneous irradiances over some regions can be large (up to 5 W m^{-2}), the global mean irradiances do not change dramatically (less than 0.5 W m^{-2}). Again, since our 5 s instantaneous measurements are generated from a WFOV that samples a large area and a wide range of viewing angles, regional differences would have a limited effect on our results and, therefore, the difference between the old and new ADMs is unlikely to affect our estimate of the anisotropic impact significantly.

2.3.2.2 Instrument performance and calibration

Because there is no existing constellation for us to properly estimate potential instrument performance, and because development and demonstration of miniaturised broadband radiometers are ongoing research activities [*Swartz et al.*, 2015, 2016], we test a number of possible scenarios to investigate how fast recovery errors grow with varying instrument performance characteristics to provide a level of uncertainty that engineering development should aim for. These scenarios include adding random instrument noise and systematic calibration errors to synthetic satellite measurements for the case used in Fig. 2.4. If these additional uncertainties are applied based on certain probability density functions, we repeat each test 10 times to ensure that the mean result is robust. A summary of these sensitivity results is listed in Table 2.1, which applies to both the SW and LW.

Firstly, a random instrument noise is included by adding 0.1 W m^{-2} of white noise to the simulated measurements, more than an order of magnitude larger than that for similar early instruments [*Kyle et al.*, 1985]. This could account for unknown variations in the angular and spectral response across the WFOV, wobbles in instrument pointing, blurring of scenes due to insufficient instrument response time, or other imperfections in the instrument or satellite performance. Since we applied white noise, the resulting difference in average global mean irradiance from the control experiment is essentially zero with a standard deviation of approximately 0.002 W m^{-2} (i.e., ~0.002 % in SW and less than 0.001 % in LW). The reason that this difference is almost negligible is that there are a huge number of individual simulated measurements that are fed to the recovery inversion such that any random noise quickly averages to zero, one of the key

advantages of a large constellation approach. When this white noise is increased to 0.25 W m^{-2} and 0.5 W m^{-2}, the average global mean difference remains essentially zero, but the associated standard deviation increases to approximately 0.01 W m^{-2}. This change is still an order of magnitude smaller than the absolute bias derived from the recovery performance (0.16 W m^{-2} in SW and 0.13 W m^{-2} in LW; see Fig. 2.8) and therefore is tolerable.

Table 2.1. Changes in hourly-recovered global means for outgoing short-wave and long-wave irradiance at the top-of-the-atmosphere, due to instrument white noise and calibration errors applied to synthetic satellite measurements. The changes in the global mean are calculated with respect to that derived from the baseline constellation. The standard deviation in the recovered global means is computed from ten realisations.

Instrument white noise (W m^{-2})	Calibration error		Change in recovered global mean (W m^{-2})
	Mean (W m^{-2})	Standard deviation (W m^{-2})	
0.1	–	–	0.000 ± 0.002
0.25	–	–	0.000 ± 0.005
0.5	–	–	0.00 ± 0.01
0.0	0.5	–	0.631
0.1	0.5	–	0.631 ± 0.003
0.1	0.5	0.1	0.657 ± 0.043

Secondly, we consider the influence of a systematic calibration bias on the recovered global mean outgoing irradiance. A flat systematic bias of 0.5 W m^{-2} across the constellation is found to result in a change in the recovered global mean of 0.63 W m^{-2}. Including 0.1 W m^{-2} of instrument noise on top of this systematic bias results in the same mean with a standard deviation of 0.003 W m^{-2}, consistent with that from instrument noise alone. Finally, instead of a systematic calibration bias, we included a standard deviation of 0.1 W m^{-2} between individual satellites, with a mean bias of 0.5

W m^{-2} and 0.1 W m^{-2} of instrument noise; this results in an average change of 0.657 W m^{-2} in the recovered global mean outgoing irradiance with a standard deviation of 0.043 W m^{-2}. Overall, the error growths due to compounding sources of uncertainty generally follow a linear behaviour.

Results in Table 2.1 suggest that maintaining any systematic bias to a minimum would be crucial for a satellite constellation to measure the EOR accurately, consistent with most climate monitoring missions. To achieve it, in addition to prelaunch and on-flight calibrations, several steps that are unique to the constellation approach can potentially help facilitate further calibration. The footprints of satellites in adjacent orbital planes have considerable simultaneous overlap at the poles, and the footprints of adjacent satellites in the same orbital plane are almost identical just minutes apart, providing the perfect opportunity to carry out frequent cross calibrations as suggested by *Wiscombe and Chiu* [2013]. In addition, the slowly evolving, bright, and largely homogeneous polar regions present an ideal natural calibration target. Absolute calibration, required to track and correct for long-term drift, would require a small subset of the constellation to have a highly accurate on board calibration system or have absolute calibration transferred to the constellation from an external source, both of which are active research areas [*Wielicki et al.*, 2008; *Swartz et al.*, 2015, 2016].

2.3.2.3 Number of satellites

Since the number of satellites available in reality may differ from the 36-satellite baseline constellation, we also test how sensitive the recovery performance is to the number of satellites using two distinct configurations: satellite limited and orbit plane limited. The satellite-limited configuration is defined as having six equally spaced orbit planes while varying the number of satellites in each plane, useful for when launch opportunities are plentiful but fewer satellites are desirable. Conversely, the orbit plane-limited configuration has six satellites in each plane while the number of orbit planes is varied, useful for when mass production of satellites is possible (i.e., CubeSats) but launch opportunities are restricted. Since these two different configurations directly lead to sampling differences, we performed recoveries every hour throughout a 24 h time period to ensure that we capture any potential worse-case scenarios within the diurnal cycle.

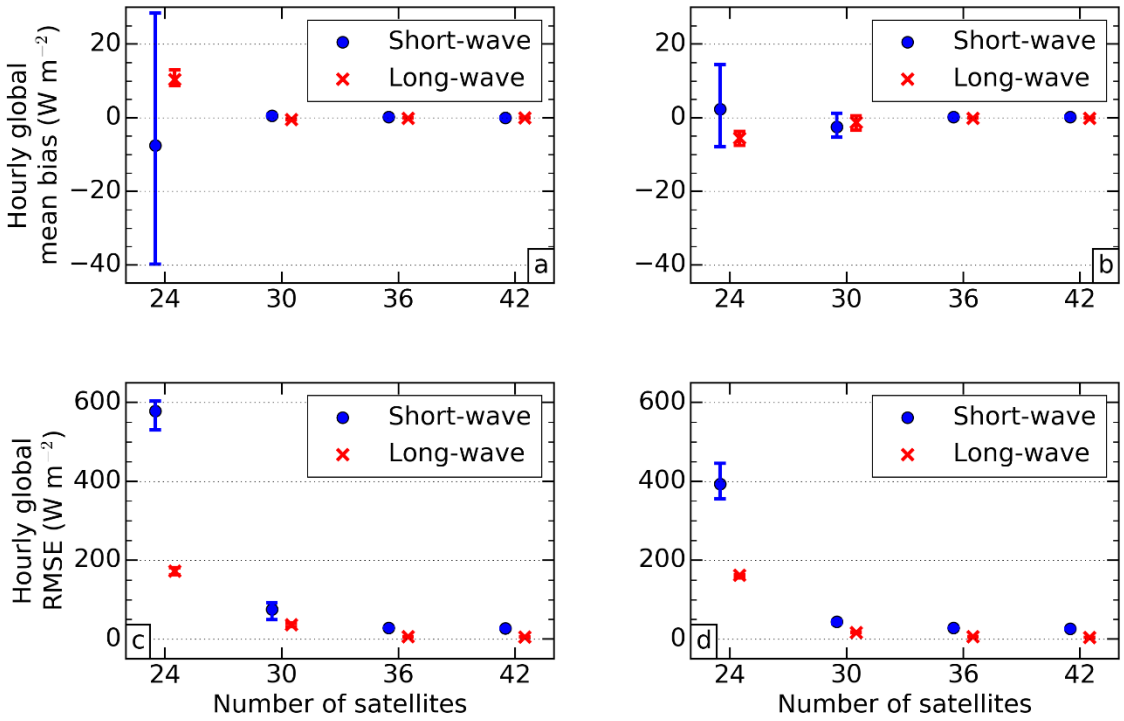

Figure 2.10. (a and b) Mean hourly bias and (c and d) root-mean-square error in the global top-of-the-atmosphere outgoing short-wave and long-wave irradiance for a satellite limited configuration (a and c) and an orbit plane limited configuration (b and d). Dots and error bars represent the means and the 25th and 75th percentiles, respectively, from 24 recovered irradiance fields.

As the number of satellites increases and the Earth becomes better sampled, Fig. 2.10 shows that the absolute global mean bias in the recovered irradiance decreases. The improvement in absolute bias from 36 satellites to 42 satellites is small in both satellite limited and orbit plane limited, and both in the SW and LW, because the recovered irradiance from 36 satellites already achieves a satisfactory SNR for a recovery to a 1000 km spatial resolution (see Fig. 2.3). For fewer than 36 satellites, the density criterion of 500 samples per hour is no longer met globally; mathematical instability begins to influence the recovery process, contaminating the global mean bias and resulting in a sharp increase in this bias. The instability becomes more widespread as the number of satellites is further reduced below 30, increasing both the average bias and the RMSE. To overcome this problem with fewer satellites would require relaxation of the 1000 km spatial resolution requirement. Additionally, while the bias and RMSE are comparable in the SW and LW for 36 and 42 satellites, the SW bias generally becomes much larger for fewer satellites. This is due to the nature of the SW

irradiance field evolving more quickly in space and time, and spanning a larger range of magnitudes, resulting in more pronounced instabilities when they do occur.

When comparing the global mean bias and RMSE between the satellite-limited and orbit plane-limited configurations, the orbit plane-limited configuration generally yields improved results. This improvement is most apparent for fewer satellites and suggests that if one needs to reduce the total number of satellites from the baseline constellation, limiting the total number of orbit planes would provide the most scientific value with the same number of satellites, recovering the global mean outgoing irradiance more accurately and better representing spatial patterns.

2.4 Summary (published abstract)

New, viable, and sustainable observation strategies from a constellation of satellites have attracted great attention across many scientific communities. Yet the potential for monitoring global Earth outgoing radiation using such a strategy has not been explored. To evaluate the potential of such a constellation concept and to investigate the configuration requirement for measuring radiation at a time resolution sufficient to resolve the diurnal cycle for weather and climate studies, we have developed a new recovery method and conducted a series of simulation experiments. Using idealised wide field-of-view broadband radiometers as an example, we find that a baseline constellation of 36 satellites can monitor global Earth outgoing radiation reliably to a spatial resolution of 1000 km at an hourly time scale. The error in recovered daily global mean irradiance is 0.16 and –0.13 W m^{-2}, and the estimated uncertainty in recovered hourly global mean irradiance from this day is 0.45 and 0.15 W m^{-2}, in the short-wave and long-wave spectral regions, respectively. Sensitivity tests show that addressing instrument-related issues that lead to systematic measurement error remains of central importance to achieving similar accuracies in reality. The presented error statistics therefore likely represent the lower bounds of what could currently be achieved with the constellation approach, but this study demonstrates the promise of an unprecedented sampling capability for better observing the Earth's radiation budget.

3 CHAPTER THREE: Insights into the diurnal cycle of global Earth outgoing radiation using a numerical weather prediction model

3.0 Statement of publication status

The material in this chapter was published in Atmospheric Chemistry and Physics on 16th April 2018. I am the lead author of the manuscript. All figures and tables and were generated by myself, and I led and finalised the scientific writing. I take full responsibility for the results. Other authors listed on this publication helped in the supply of model and observational data, were involved in discussions of the methods and provided valuable feedback on the results. The published manuscript can be found at the following reference:

Gristey, J. J., J. C. Chiu, R. J. Gurney, C. J. Morcrette, P. G. Hill, J. E. Russell, and H. E. Brindley. (2018). Insights into the diurnal cycle of global Earth outgoing radiation using a numerical weather prediction model. *Atmospheric Chemistry and Physics*, **18(7)**, 5129–5145. https://doi.org/10.5194/acp-18-5129-2018

The content of this chapter differs from the published article in the following ways:

- The published abstract is moved to the end of the chapter to provide a concise summary;
- The published conclusions and summary are excluded from this chapter and are incorporated into Chapter 5;
- For consistency with the thesis structure, the numbers of the section headings, equations, figures and tables are updated, and minor format changes are applied.

Note that the published introduction included in this chapter contains minor overlaps with Chapter 1, but is included in its original form for completeness.

3.1 Introduction

Solar radiation entering the top of the atmosphere (TOA) is the primary energy source for atmospheric processes on Earth. Around a third of this radiation is returned directly to space as reflected solar radiation (RSR). The remainder is absorbed by the atmosphere and surface, acting to constantly heat the Earth. The Earth is, in unison,

constantly losing heat energy to space in the form of outgoing long-wave radiation (OLR). The RSR and OLR, collectively referred to as Earth outgoing radiation (EOR), approximately balance the incoming solar radiation when globally and annually averaged, maintaining a state of equilibrium in the global energy budget [e.g., *Trenberth*, 2009; *Stephens et al.*, 2012; *Wild et al.*, 2015]. Understanding the physical nature and influences on the processes that determine the variability in the global energy budget underpins climate science research.

While the TOA incoming solar radiation is relatively stable, predictable and observed with high accuracy [e.g., *Kopp and Lean*, 2011], EOR is dynamic by nature and therefore inherently more difficult both to observe and to understand. This is perhaps manifested most clearly in the strong diurnal signatures that EOR exhibits, a direct result of the rapidly evolving scene from which the radiation originates. Diurnal variability in the Earth system that defines such signatures has been studied extensively [e.g., *Nitta and Sekine*, 1994; *Webster et al.*, 1996; *Soden*, 2000; *Yang and Slingo*, 2001; *Wood et al.*, 2002; *Nesbitt and Zipser*, 2003; *Taylor*, 2012]. However, discrepancies persist when comparing the diurnal cycles in observations and models [e.g., *Betts*, 2002; *Dai and Trenberth*, 2004; *Slingo et al.*, 2004; *Tian et al.*, 2004; *Itterly and Taylor*, 2014]. These discrepancies highlight a lack of understanding along with insufficient computing resources; yet it is essential to correctly represent diurnal variability since it constitutes a fundamental forcing cycle for our weather and climate.

Previous attempts to identify patterns of diurnal variability in EOR have made use of principal component analysis (PCA). For example, *Smith and Rutan* [2003] performed PCA on seasonally averaged OLR observations bounded by 55° N to 55° S from the scanning radiometer aboard the Earth Radiation Budget Satellite (ERBS) [*Harrison et al.*, 1983; *Barkstrom*, 1984]. They found dominant patterns that appeared to be related to heating of the surface and lead–lag effects from the development of cloud, noting that the patterns over ocean and land explain significantly different amounts of variance. *Comer et al.* [2007] applied a similar method to OLR observations from the Geostationary Earth Radiation Budget (GERB) instrument [*Harries et al.*, 2005] but, instead of separating land and ocean, chose to consider the domain as a whole. The dominant patterns in the GERB observations were similar to those found by *Smith and Rutan* [2003] but the orography of the land was used to support the explanation of the patterns, illustrating the value of additional information for understanding the physical

processes involved. The dominant OLR patterns of variability revealed by PCA also provide a useful tool for comparing and evaluating the diurnal cycle of OLR in climate models [*Smith et al.*, 2008].

By contrast with OLR, the diurnal cycle of RSR has received less attention. This is likely due to its non-continuous nature and relatively complex variations. To our knowledge only *Rutan et al.* [2014] have considered RSR by using observations from the ERBS, similar to *Smith and Rutan* [2003], to perform PCA on the diurnal cycle of TOA albedo. Interestingly, they found the diurnal cycle of TOA albedo is primarily driven by a dependence on solar zenith angle (SZA) and that any other signals are an order of magnitude smaller.

The aforementioned studies represent the forefront of our knowledge regarding the dominant patterns of diurnal variability in EOR. However, none of the datasets used in those studies permit the global coverage required for relating the revealed patterns back to the global energy budget, nor do they use variations in other geophysical data to support physical interpretation of the patterns. A numerical weather prediction (NWP) model provides a unique tool for achieving these criteria. Clearly, care must be taken to analyse the model data in line with their ability to reproduce real-world processes, but the wealth and variety of data available enables a deeper understanding at the process level. It is intended that any process-level understanding obtained from analysis of NWP model output will help to formulate hypotheses that can be tested later with observations.

Here we perform PCA on global output from the Met Office NWP model. The dominant patterns of variability that this reveals will be supported by satellite observations and radiative transfer calculations where possible. Section 3.2 outlines details of the model run and supporting satellite datasets. Section 3.3 describes the method of identifying and interpreting patterns of diurnal variability. Section 3.4 reports our findings that, crucially, take three distinct steps forward. In Sect. 3.4.1, we examine the dominant patterns of diurnal variability in OLR at a fully global scale for the first time, required for relating the dominant patterns to the global energy budget. In Sect. 3.4.2, we examine the dominant patterns in the diurnal variability of TOA albedo, using the surface and cloud-free fluxes combined with radiative transfer calculations to reveal the processes contributing to the patterns. In Sect. 3.4.3, the patterns of EOR

variability are coupled with variability in other relevant geophysical variables to aid their physical interpretation. Section 3.5 summarises the results and conclusions are drawn.

3.2 Data

3.2.1 Global model output

The main data used in this analysis are synthetic global EOR fields generated using the Met Office Unified Model in its global NWP configuration. We used the Global Atmosphere 6.0 (GA6) and Global Land 6.0 (GL6) components, described by *Walters et al.* [2017], with sea surface temperatures and sea ice prescribed from the Operational Sea Surface Temperature and Sea Ice Analysis [*Donlon et al.*, 2012]. The sea surface temperatures are updated daily and, therefore, do not exhibit diurnal variability. Operationally, for reasons of computational expense, full radiation calculations are not done every time step [*Manners et al.*, 2009]. In GA6, the full radiation calculations are done every hour, with an update to represent the changing cloud fields every 12 min time step [*Manners et al.*, 2009; *Walters et al.*, 2017]. In this simulation however, the full radiation scheme, based on *Edwards and Slingo* [1996], was called on every model time step to better represent the evolution of EOR. The model was run with this set-up for each day from an operational 0000 Z analysis.

The data are provided for each day in September 2010. The year of 2010 was chosen arbitrarily, but the month of September was selected specifically due to the timing of the equinox. At the equinox the day length is approximately constant at all locations on Earth, so the months containing the equinoxes are the only times during the year that a consistent diurnal cycle can be assessed globally. In particular, RSR only has a signature during the daylight hours so away from the equinoxes the analysis would be fundamentally limited in one of the hemispheres. While dominant patterns in the diurnal cycle of EOR do exhibit spatial variations between seasons, the relative importance of physical processes that control the dominant patterns typically remains robust throughout the year [*Smith and Rutan*, 2003; *Rutan et al.*, 2014]. This allows insight to be gained for the entire annual cycle, at least in a qualitative sense, by just considering this unique situation.

The data are provided with a 12 min temporal resolution (i.e., at every model time step) on the N320 grid, giving a spatial resolution of approximately 40 km in mid-latitudes.

These temporal and spatial resolutions are selected to retain all relevant information while avoiding data redundancy. This is based on initial experiments in which we reduced the temporal/spatial resolutions artificially in one day of very high resolution (5 min/ ∼17 km in mid-latitudes) global EOR fields, and found that the dominant patterns in the data (see Sect. 3.3.2) are well retained at a resolution of 15 min/ ∼50 km in mid-latitudes.

When analysing the RSR we work with the TOA albedo, similar to *Rutan et al.* [2014], calculated as the division of outgoing by incoming TOA solar irradiance. This normalisation removes the variability associated with the amount of incoming solar radiation that would otherwise dominate the diurnal cycle, but is not of interest here. For September 2010 it is possible to define the TOA albedo from 07:00 to 17:00 local solar time and from 61.5° N to 61.5° S, encompassing over 94 % of the total incoming short-wave irradiance entering the Earth system.

As well as the OLR and TOA albedo, a host of other geophysical variables were simultaneously outputted from the model to aid the physical interpretation of the EOR diurnal cycles. The additional variables included in this study are the equivalent surface and clear-sky radiation fluxes, surface temperature, cloud liquid water path (LWP), cloud ice water path (IWP) and cloud top height (CTH).

3.2.2 Supporting satellite datasets

Several observational datasets of EOR currently exist that are derived from various satellite instruments. Global EOR observations, such as those from the Clouds and the Earth's Radiant Energy System (CERES) instrument [*Wielicki et al.*, 1996], provide complete coverage but are not used in this study mainly due to their lack of diurnal sampling from low-Earth Sun-synchronous orbits. Substantial efforts have been applied to interpolate between the diurnal gaps in CERES sampling [*Doelling et al.*, 2013, 2016] but these products do not match the high temporal resolution of the model data required for thorough investigations of the diurnal cycle. Observations from the Scanner for Radiation Budget (ScaRaB) instrument are capable of capturing long-term averaged diurnal variability due to the drifting orbit of the MeghaTropiques satellite [*Viollier and Raberanto*, 2010], but are limited to the central tropics due to the very low inclination of the orbit and are therefore also not appropriate. GERB observations, however, made from the unique vantage point of geostationary orbit, provide EOR at

high temporal resolution over a large region including Africa, Europe and their surrounding waters, and are therefore much better suited to this study. An added advantage is that simultaneous retrievals of cloud properties are available from the Spinning Enhanced Visible and InfraRed Imager (SEVIRI) instrument [*Schmid*, 2000]. We therefore choose to use the GERB and SEVIRI observations to support our model analysis.

Specifically, we make use of OLR and TOA albedo observations from GERB 2 (GERB Edition 1 High Resolution product with "SW combined adjustment" applied) and CTH observations from SEVIRI (Climate Monitoring Satellite Applications Facility (CMSAF) Cloud Property DAtAset using SEVIRI (CLAAS) Edition 2 product [*Finkensieper et al.*, 2016; *Benas et al.*, 2017]). We do not include the SEVIRI LWP and IWP products because the retrieval method, which assumes that the cloud phase is the same as the cloud top for the whole column, leads to unphysical diurnal variability during convective cloud development, which turns out to be an important process in the diurnal cycles of both OLR and TOA albedo, as will be shown in Sect. 3.4. To avoid missing data in the Southern Hemisphere and high uncertainty data near the edge of the field of view (FOV) we use data north of 20° S and with a viewing zenith angle of less than 70°, respectively. Unfortunately, the time window of the model and observation data cannot be matched because full diurnal GERB observations are not available close to the equinoxes due to potential instrument damage. Instead we use observations from July 2006. This month accommodates large solar insolation over the Northern Hemisphere land mass in the GERB FOV that should amplify any diurnal signatures in these regions, and was also the subject of the *Comer et al.* [2007] study. We acknowledge that it would be ideal to use model output from July 2006 for comparison with these observations. However, to fully capitalise on understanding the diurnal cycle at a global scale, it is crucial to use the model output for September because the relative importance of processes inferred from a global and a regional scale can be quite different (as discussed in Sect. 3.4.1).

Note that the longitudinal coverage of GERB has recently been extended to include the Indian Ocean [*Dewitte et al.*, 2017], but the coverage remains well short of global. This lack of global coverage removes the opportunity to investigate processes across regions that is afforded by the model data, but at least allows us to evaluate our model results over one portion of the globe. The potential for global diurnal sampling of EOR from a

single observing system has recently been highlighted via the use of a constellation of small satellites [*Gristey et al.*, 2017] but, for now at least, observations required to resolve the diurnal cycle fully in global EOR do not exist.

3.3 Method

3.3.1 Pre-processing

Before performing PCA, we must ensure that the data fields are in an appropriate format for extracting patterns of diurnal variability. This involves conversion of the diurnal time coordinate, creation of an average diurnal cycle and a correction to account for changes in grid resolution, implemented as follows.

First, all data fields are transformed from UTC to local solar time. This is required such that all spatial locations correspond to the same part of the diurnal cycle. To achieve this transform, we note that each longitude column in UTC represents a single local solar time. We then select the longitude columns from each UTC map that correspond to the same local solar time and combine them to generate a new set of maps that are now a function of local solar time.

Next, we calculate the monthly average diurnal cycle for each data field by simply averaging the local solar time maps from each day in the month. Since the variations on any given day consist of not only diurnal variations, resulting from the periodic forcing, but also transient weather variations, which are not diurnally forced, performing this monthly averaging helps to reduce the noise from weather events and extract the signal from the diurnal variations of interest.

Lastly, since the data are on equal latitude-longitude grids, we apply a latitude correction by multiplying each grid point by the square root of the cosine of its latitude. This avoids spurious poleward enhancement of variability due to the changes in grid spacing [e.g., *Wallace et al.*, 1992; *Comer et al.*, 2007; *Bakalian et al.*, 2010].

Note that we do not separate data over ocean and land before performing PCA. This is because we intend to reveal global patterns and their relative importance across all regions. *Comer et al.* [2007] showed that the behaviour of the system can be captured well by considering the diurnal cycles over ocean and land simultaneously.

3.3.2 Extracting dominant patterns of EOR diurnal variability

PCA applied to the local solar time, monthly averaged and latitude corrected fields of OLR and TOA albedo extracts empirical orthogonal functions (EOFs) and principal components (PCs) that reveal spatial and temporal patterns in the data, respectively. The first PC describes the maximum possible variance, and each subsequent PC describes the maximum possible variance remaining once the preceding PCs have been removed. There are several approaches to achieve PCA. The approach used is this study is outlined below.

First, we generate a data matrix, $\boldsymbol{F}$, containing the spatial-temporal data to be used as input for the PCA. The matrix $\boldsymbol{F}$ has t rows and s columns, where t is the number of time steps in the diurnal cycle and s is the total number of spatial grid points. In other words, each row of $\boldsymbol{F}$ consists of a flattened map of the data field at a given local solar time, and each column represents a time series at a given location. Additionally, the mean is removed from each column of $\boldsymbol{F}$ to give an anomaly time series.

In a standard PCA one would next form the large covariance matrix, $\boldsymbol{R}$, of $\boldsymbol{F}$ given by

$$\boldsymbol{R} = \boldsymbol{F}^T\boldsymbol{F}, \tag{3.1}$$

and perform an eigenvalue decomposition on $\boldsymbol{R}$ to obtain the EOFs. However, in this application $\boldsymbol{F}$ is very non-square (the spatial dimension is much greater than the temporal dimension), which would result in a very large $s \times s$ covariance matrix from Eq. (3.1) and an expensive eigenvalue decomposition. To reduce computational expense, we follow the equivalent method to obtain the leading EOFs and PCs by forming the smaller $t \times t$ covariance matrix, $\boldsymbol{R}^*$, given by

$$\boldsymbol{R}^* = \boldsymbol{F}\boldsymbol{F}^T. \tag{3.2}$$

The eigenvalue problem for the small covariance matrix, $\boldsymbol{R}^*$, in Eq. (3.2) is formulated as

$$\boldsymbol{R}^*\boldsymbol{C}^* = \boldsymbol{C}^*\boldsymbol{\lambda}', \tag{3.3}$$

where $\boldsymbol{C}^*$ is a $t \times t$ matrix with columns comprising the eigenvectors of $\boldsymbol{R}^*$; and $\boldsymbol{\lambda}'$ is a $t \times t$ diagonal matrix containing the corresponding eigenvalues in descending order. For convenience, the diagonal elements of $\boldsymbol{\lambda}'$ are placed into $\boldsymbol{\lambda}$, a row vector of length t.

The eigenvalues, $\boldsymbol{\lambda}$, from Eq. (3.3) are also the leading eigenvalues of the large covariance matrix, $\boldsymbol{R}$, in Eq. (3.1). However, the leading eigenvectors of $\boldsymbol{R}$ are not $\boldsymbol{C}^*$, but are represented by columns in a $s \times t$ matrix $\boldsymbol{C}$. These column vectors, $\boldsymbol{C}_j$, are calculated as

$$\boldsymbol{C}_j = (\boldsymbol{F}^T \boldsymbol{C}^*)_j \Big/ \sqrt{\lambda_j}. \tag{3.4}$$

A proof of this relationship is provided by *Bjornsson and Venegas* [1997]. The column vectors $\boldsymbol{C}_j$ are the EOFs that we seek. For illustrative purposes, we scale each EOF such that the maximum absolute value is ten.

The corresponding PC is calculated by projecting the original data matrix, $\boldsymbol{F}$, on to the EOF, $\boldsymbol{C}_j$, in Eq. (3.4) as

$$\boldsymbol{A}_j = \boldsymbol{F}\boldsymbol{C}_j, \tag{3.5}$$

where $\boldsymbol{A}_j$, a column vector of length t, is the PC that we seek.

The percentage variance, τ_j, explained by the EOF/ PC pair from Eq. (3.4) and Eq. (3.5) is

$$\tau_j = \left(\lambda_j \Big/ \sum_{n=1}^{t} \lambda_n\right) \times 100. \tag{3.6}$$

3.3.3 Coupling dominant patterns of diurnal variability

To aid physical interpretation of the leading EOR EOFs, the corresponding PCs and the percentage variance they explain, respectively calculated from Eq. (3.4)–(3.6), we also investigate their extent of coupling with the variability in other geophysical variables. Coupled PCA patterns between multiple variables have been widely examined in the weather and climate sciences [e.g., *Kutzbach*, 1967; *Wallace et al.*, 1992; *Deser and Blackmon*, 1993; *Zhang and Liu*, 1999] but this additional step has not been applied in previous PCA studies of EOR.

A comprehensive overview of the advantages and disadvantages of common techniques used to identify coupled patterns is given by *Bretherton et al.* [1992]. Here, we are interested in the relationship between a selected pattern of variability in EOR and all of the variability in another variable, which is well suited to an analysis technique

previously referred to as single-field PCA [e.g., *Wallace et al.*, 1992]. In our application, this will involve studying the correlations between a PC in either OLR or TOA albedo with the diurnal cycle of another variable that we expect to be related to the PC. These correlations are illustrated as heterogeneous correlation maps, which reveal the spatial distributions of where the selected EOR PC has the highest correlations with the diurnal variability in the other variable.

Before generating the heterogeneous correlation maps, we first perform a cross-correlation between the selected EOR PC and the related PC of the other variable to identify any lag between the patterns. Both PCs represent global time series with the rationale that the radiation PC is dominated by a certain process, and the other PC exhibits variability directly related to that process. The cross-correlation is achieved here by calculating a set of Pearson correlation coefficients between the PC of the other variable, which remains fixed in time, and the EOR PC, which is shifted by one time step at a time throughout the entire diurnal cycle. For the TOA albedo, the correlation coefficients are calculated for the time window over which it is defined. From this cross-correlation we can extract the maximum correlation coefficient magnitude, giving an indication of the strength of coupling, and the lag time at which it occurs, giving an indication of how out of phase the patterns are. We define the lag time to be positive when the PC of EOR follows the PC of the other variable (e.g., a change in OLR occurs after the development of LWP). The lag time is then removed before calculating the heterogeneous correlation maps.

The lag times themselves also provide insight into processes and their evolution. We therefore calculate the lag times between various radiation and cloud variables in both the model and GERB/SEVIRI observations. Since the observational data are provided on an irregular grid, we linearly interpolate the observational data onto the same grid as the model data in order to perform the local solar time conversion (see Sect. 3.3.1).

3.4 Results

3.4.1 Dominant patterns of diurnal variability in modelled global OLR

The first EOF of the global OLR diurnal cycle (Fig. 3.1a) reveals positive weights, indicating a consistent sign in the diurnal variations, over land surfaces that are largest in arid regions such as the Sahara Desert, Atacama Desert and Arabian Peninsula. The

corresponding PC (Fig. 3.1c) reaches maximum amplitude just after local midday and minimum amplitude overnight. This spatio-temporal pattern is consistent with that expected from solar heating of the land surface and accounts for 68.5 % of the global diurnal variance.

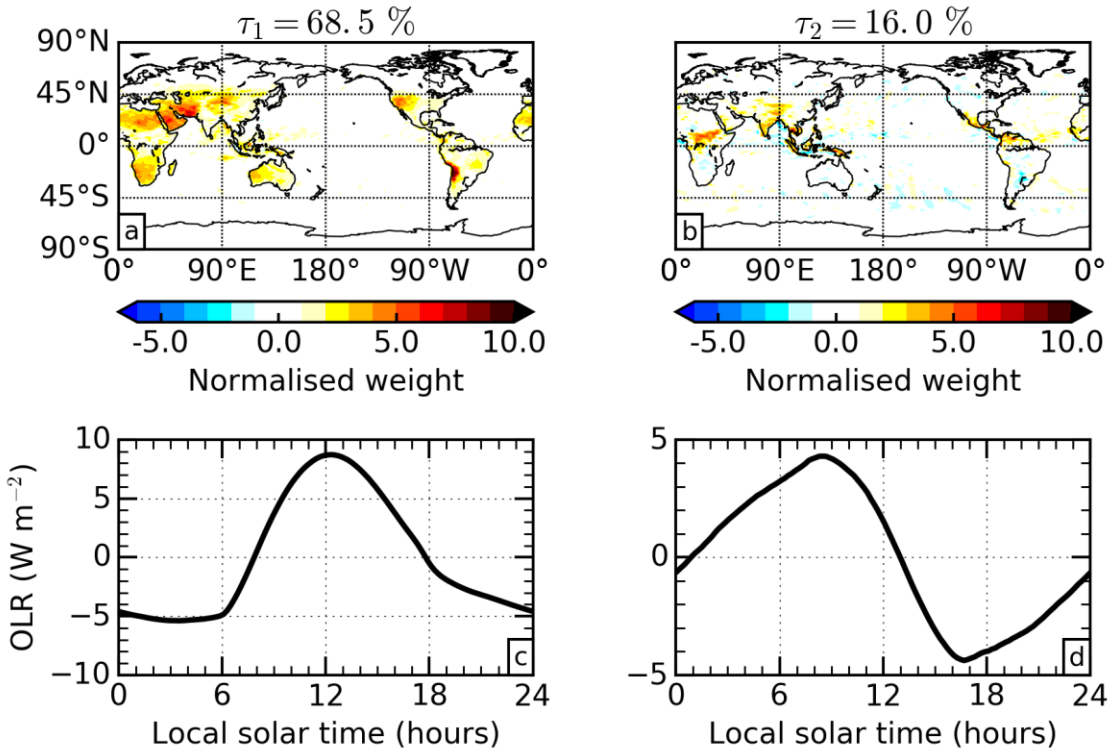

Figure 3.1. Principal component analysis of the global outgoing long-wave radiation (OLR) diurnal cycle for September 2010 in the Met Office model. The empirical orthogonal functions (a and b) and principal components (c and d) are presented for the first (a and c) and second (b and d) most dominant patterns of variability. The percentage variance explained by each pattern is stated above the corresponding empirical orthogonal function.

Although solar heating occurs primarily at the surface, the atmosphere is also heated mainly via absorption of the increased surface emission. The OLR can therefore increase due to increased emission from the warmer atmosphere, as well as increased emission from the warmer surface. To understand whether the first diurnal pattern of OLR (Fig. 3.1a and c) is dominated by surface or atmospheric heating, we performed the following radiative transfer calculations, and use the Sahara Desert as an example since this region contributes strongly to the diurnal pattern.

Firstly, for a surface emission change of ΔSE due to an increased surface temperature, the atmospheric transmittance, Tr, can be derived as

$$Tr = \Delta OLR / \Delta SE, \quad (3.7)$$

where ΔOLR is the corresponding change in OLR. Assuming an increase of 1 K in surface temperature, Fig. 3.2a shows that Tr ranges between 15 and 38 % in various clear-sky conditions, larger than the global mean of 10 % reported by *Costa and Shine* [2012] for all-sky conditions. Since the dry and predominantly clear-sky atmosphere over the Sahara Desert corresponds to a similar amount of water vapour to that of the mid-latitude winter profile used in Fig. 3.2a, we take 30 % as an estimate for Tr in the next back-of-the-envelope calculations.

Now we estimate ΔSE in Eq. (3.7) for the Sahara Desert region from model output. Figure 3.2b shows that the model diurnal surface temperature range in the Sahara Desert is around 40 K, with a typical minimum surface temperature of 293 K at night-time and a maximum surface temperature of 333 K at daytime. This diurnal temperature change leads to a ΔSE of ~250 W m^{-2}, assuming a surface emissivity of 0.9 over the Sahara Desert [*Ogawa and Schmugge*, 2004]. Combining the estimated Tr of 30 %, from Eq. (3.7) we can derive ΔOLR to be ~75 W m^{-2}. This is comparable to the magnitude of the total change represented by the combination of the first EOF and PC (Fig. 3.1a and c), without considering any change in atmospheric temperature.

Similarly to the previous exercise, we next consider the case of fixed surface temperature and instead perturb the atmospheric temperature. Figure 3.2c shows that the diurnal range of atmospheric temperature close to the surface (2 m altitude) is already a factor of 2 smaller than at the surface itself. By examining some vertical profiles of diurnal temperature range in the Sahara Desert (not shown), we find that the diurnal temperature range becomes negligible at around 100 m altitude. Taking an exaggerated case that the magnitude of the 2 m diurnal temperature range, ~20 K in the Sahara Desert, is present over the entire bottom 100 m of the atmosphere, and fixing the surface temperature at the centre of the diurnal range of 313 K, results in ΔOLR of less than 1 W m^{-2} for the mid-latitude winter atmosphere. This result holds regardless of whether the initial atmospheric temperature is taken from the standard mid-latitude winter atmosphere, or from the September 2010 minimum and maximum 2 m model temperatures in the Sahara Desert, and is consistent with the fact that the atmosphere is

an order of magnitude less efficient at increasing OLR for a given change in temperature [*Soden et al.*, 2008]. We therefore conclude that the first spatial-temporal pattern in the diurnal cycle of OLR is dominated by increased surface emission.

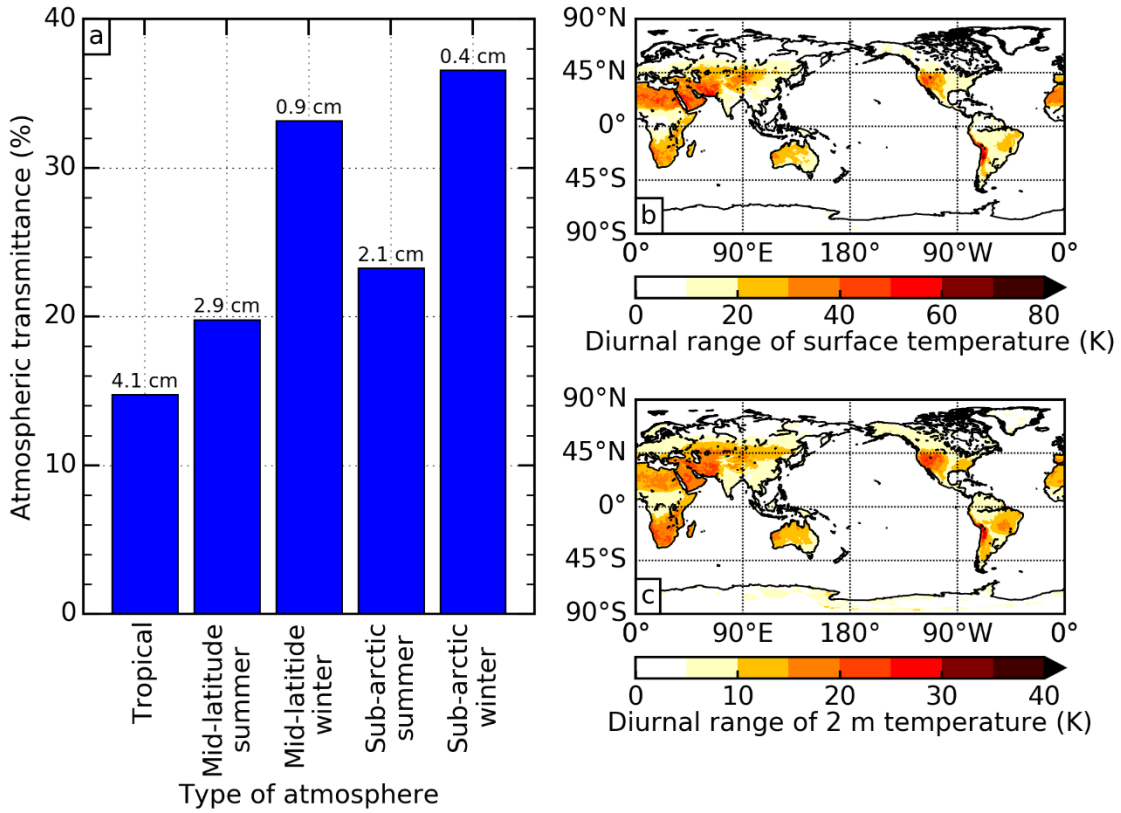

Figure 3.2. (a) Atmospheric transmittance calculated from radiative transfer, using standard atmospheric profiles with various amounts of precipitable water (denoted above each bar). Panels (b) and (c) show the maps of diurnal range of surface temperature and 2 m temperature, respectively, calculated from the average diurnal cycle for September 2010 in the Met Office model. The transmittance is calculated using Eq. (3.7**), given as a ratio of changes in outgoing long-wave radiation to changes in surface emission, assuming a 1 K increase in surface temperature. The initial surface temperatures used in calculations are 299.2 K (tropical profile), 285.8 K (mid-latitude summer and winter profiles) and 256.4 K (sub-arctic summer and winter profiles), calculated by averaging modelled surface temperature over the regions of 30° N–30° S, 30–60° N and S and 60–90° N and S, respectively. The Discrete Ordinate Radiative Transfer (DISORT) model Santa Barbara DISORT Atmospheric Radiative Transfer [*Ricchiazzi et al.*, 1998] is used here.**

The second EOF (Fig. 3.1b) contains consistent features across many different regions, but the features themselves are small in spatial extent and therefore difficult to interpret at the global scale. When examining the Maritime Continent region as an example (Fig. 3.3), we find positive weights over the islands that are enhanced along the coastlines and negative weights just offshore. Similar patterns are seen in other coastal regions in the tropics. The corresponding PC (Fig. 3.1d) shows that these patterns are at a minimum in the late afternoon and a maximum in the early morning. This spatio-temporal pattern, accounting for 16.0 % of the global diurnal variance, is consistent with the OLR signature from the cold tops of deep convective clouds that develop over land during the late afternoon and over the oceans in the early morning. The unique topography of this region permits strong sea breezes [*Qian*, 2008], explaining the enhancement along the coastlines. Note that in the studies by *Smith and Rutan* [2003] and *Rutan et al.* [2014], coastal data are omitted. The spatial patterns of OLR in this region also match surprisingly well with retrieved rainfall at different times during the diurnal cycle, as presented by *Love et al.* [2011] using observations from the Tropical Rainfall Measuring Mission (TRMM). However, the timing of the minimum modelled OLR signal is substantially earlier than the peak in TRMM retrieved rainfall, consistent with well documented model biases in the timing of convection [e.g., *Yang and Slingo*, 2001].

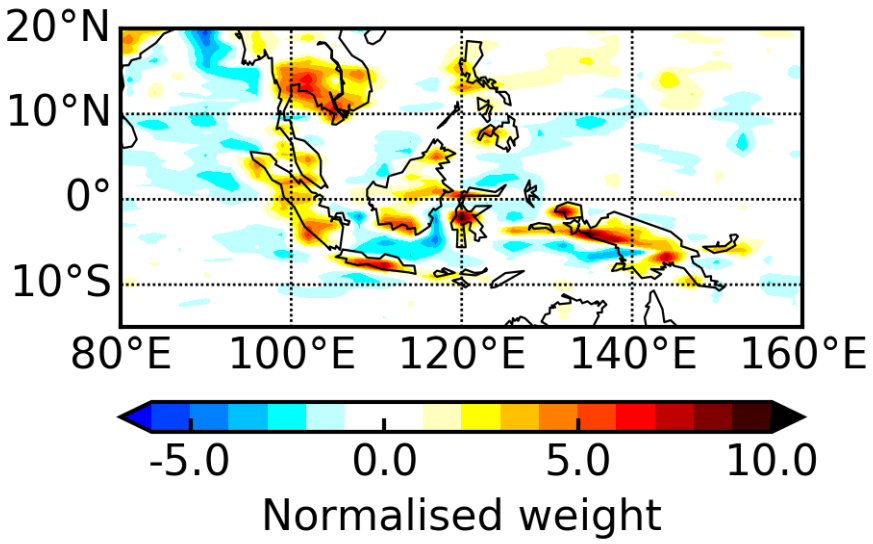

Figure 3.3. A zoom-in of Fig. 3.1b showing the second empirical orthogonal function over the Maritime Continent region bounded by 15° S–20° N and 80–160° E.

Both of the dominant EOFs and PCs of OLR diurnal variability in Fig. 3.1 are, reassuringly, similar to those identified with GERB [*Comer et al.*, 2007] and ERBS [*Smith and Rutan*, 2003] observations, despite the different regions and time periods considered. However, what is markedly different is the percentage variance that these patterns account for. *Comer et al.* [2007] considered the domain of analysis as a whole rather than separating land and ocean, facilitating a direct comparison with our results. The variances explained by the dominant patterns in their study were 82.3 and 12.8 %. To first order, this suggests that their results exhibit a higher relative contribution from surface heating to the OLR diurnal variability and a lower relative contribution from convective processes, although there may also be an influence from the fact that the actual diurnal variations in some regions can be better explained by a contribution from both dominant patterns for reasons such as surface thermal lag [*Futyan and Russell*, 2005]. This only appears to be the case for a small number of regions including the Tibetan Plateau and parts of southern Africa. However, the total variance explained by their first two patterns is higher at 95.1 % compared with 84.5 % in our results. These differences could be a result of the different time periods and spatial regions considered, or model-observation discrepancies such as the fixed sea surface temperatures in the model. To isolate the influence from different spatial regions, we repeated our analysis using the model data subsampled over the GERB FOV (not shown), and found that the total variance explained by the first two patterns increases to 89.6 %, indicating that around half of the difference is due to the disproportionately high fraction of land mass within the GERB FOV. This is because the first two dominant patterns of OLR diurnal variability appear to be driven, directly and indirectly, by solar heating of land mass. Interestingly, this suggests that the relative importance of diurnal processes acting within the GERB FOV, the only portion of the Earth for which we currently make well resolved diurnal observations of EOR, may not be representative of the global OLR diurnal cycle.

3.4.2 Dominant patterns of diurnal variability in TOA albedo

3.4.2.1 From model output

PCA is repeated for the TOA albedo diurnal cycle. The dominant pattern of variability, explaining 88.4 % of the total variance, consists of an EOF (Fig. 3.4a) with positive weights everywhere, and a diurnally symmetric PC (Fig. 3.4c) that follows the inverse

timing of incoming short-wave irradiance. The dominance of this leading spatio-temporal pattern, despite being consistent with observations from the ERBS [*Rutan et al.*, 2014], is somewhat surprising given that the TOA albedo is a quantity normalised by the amount of incoming solar radiation. This dominance indicates a strong dependence of the TOA albedo on the SZA itself that has been well documented in empirically based angular distribution models [*Loeb et al.*, 2003, 2005; *Su et al.*, 2015], but warrants further investigation into the physical processes at play.

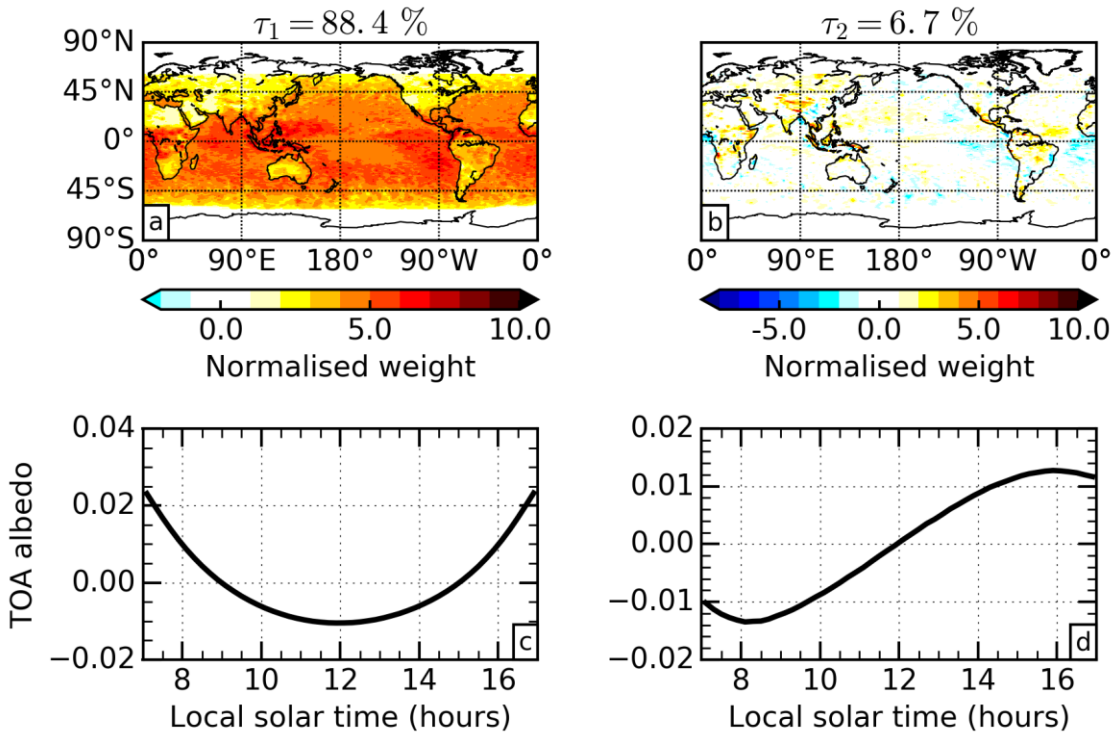

Figure 3.4. Same as Fig. 3.1, but for the top-of-atmosphere (TOA) albedo.

The first PC in Fig. 3.4c has a U-shape feature, representing a dependence on $1/\mu_0$, where μ_0 is the cosine of SZA. To illustrate how the cloud-free atmosphere contributes to the shape, Fig. 3.5 shows TOA albedos from offline radiative transfer simulations under various simplified situations. For a typical example of an aerosol-free atmosphere, we see that Rayleigh scattering dominates and that atmospheric absorption is only able to counteract this dependence when the Rayleigh scattering is scaled down to around 10 % of its original value (Fig. 3.5a). Adding a moderate amount of aerosol into the simulations (Fig. 3.5b), we find that the U-shape is retained but is scaled to a different magnitude. In fact, this U-shape is not limited to certain atmosphere set-ups or aerosol types because, in low optical depth atmospheres, different optical depths, single

scattering albedos and asymmetry parameters only provide a scaling of the shape. In other words, the reflectance function of the atmosphere under a single scattering approximation always retains a dependence on $1/\mu_0$ since this is the factor by which the path length increases and heightens the chance of a scattering event occurring. As a result, the first EOF (Fig. 3.4a) exhibits weakly positive weights in many different predominantly cloud-free regions, such as the global deserts.

The influence of the surface and cloud is also clearly evident in the first EOF. There are generally larger weights over the ocean than the land, and the largest weights occur in regions of persistent cloud (e.g., marine stratocumulus regions and the intertropical convergence zone (ITCZ)). The larger diurnal variations over the oceans can be seen by comparing the global-mean diurnal cycle of TOA albedo separated over land and ocean explicitly (Fig. 3.6a). The reason for these differences is revealed by examining the diurnal cycle in the albedo defined at the surface (Fig. 3.6b); we find the albedo over land surfaces is larger and diurnally constant. The erosion of the U-shape by brighter surfaces can be seen in Fig. 3.5b, and the SZA dependence of the surface albedo itself follows directly from the set-up of surface albedo in the model, which is Lambertian over land, but uses a modified version of the parametrisation from *Barker and Li* [1995] over the ocean. Similarly, the larger diurnal variations in the presence of cloud can be seen by comparing the global-mean diurnal cycles of all-sky (Fig. 3.6a) and clear-sky (Fig. 3.6c) TOA albedo. The differences are particularly evident over land, where the diurnal range in global mean albedo reduces from 0.11 in the all-sky field to 0.07 in the clear-sky field. This is consistent with the sharp contrast in the EOF over land (Fig. 3.4a) between predominantly cloudy regions, such as along the ITCZ over central Africa, and predominantly clear-sky regions, such as immediately north of the ITCZ over Africa. Note that the U-shape can also become weaker as the mean cloudiness of a region increases because the amount of radiation scattered to space per unit optical depth decreases with increasing cloud optical depth. Over both land and ocean surfaces, cloud introduces a more rapid change in the TOA albedo close to midday when the incoming solar radiation is most intense.

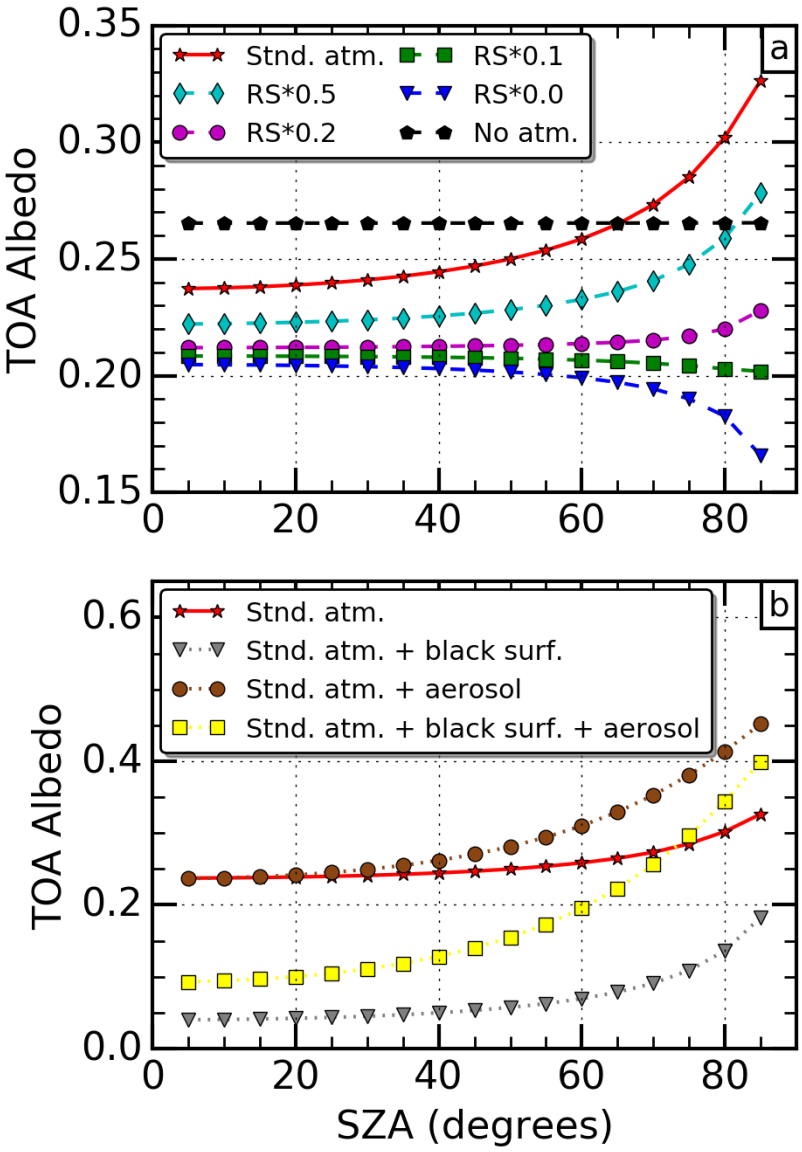

Figure 3.5. Simulation of top-of-atmosphere (TOA) albedo as a function of solar zenith angle (SZA). The dashed lines (a) represent atmospheres where a scaling factor has been applied to the Rayleigh scattering (RS). The dotted lines (b) represent atmospheres where either aerosols are included, or the surface albedo is set to zero (black surf.), or both. The solid red line with star marker appearing in both plots represents the standard atmosphere (Stnd. atm.) with no modifications. All simulations assume a US62 standard atmosphere over a Lambertian vegetated surface unless otherwise stated. When aerosols are included, their optical depth is set to 1 at 550 nm and their optical properties are typical of rural aerosols. Details of the aerosol optical properties and the tool used to perform these calculations, the Discrete Ordinate Radiative Transfer (DISORT) model Santa Barbara DISORT Atmospheric Radiative Transfer, are given by *Ricchiazzi et al.* [1998].

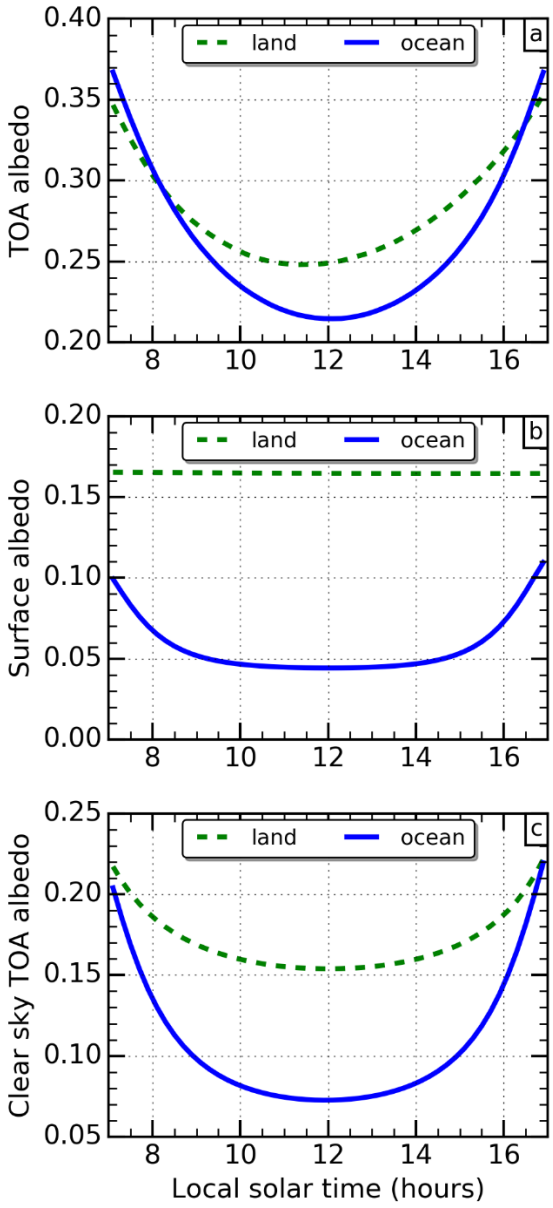

Figure 3.6. The diurnal cycle of global mean albedo for September 2010 in the Met Office model for (a) top-of-atmosphere (TOA) all-sky, (b) surface and (c) TOA clear-sky albedo, separated over land (green dashed line) and ocean (blue solid line).

The second EOF of the TOA albedo diurnal cycle (Fig. 3.4b) contains many smaller scale features similar to those of the second EOF for OLR. In fact, zooming in to the Maritime Continent region again (Fig. 3.7) reveals very similar patterns. The corresponding PC (Fig. 3.4d), however, is reversed in sign when compared with the second PC for OLR. This is consistent with the enhanced reflection from convective

clouds that develop over land during the late afternoon and over the oceans in the early morning. This acts to skew the TOA albedo diurnal cycle to earlier in the day over land (minimum around 11:20 local solar time) and later in the day over the oceans (minimum around 12:10), which is evident in Fig. 3.6a. This spatio-temporal pattern explains just 6.7 % of the total variance.

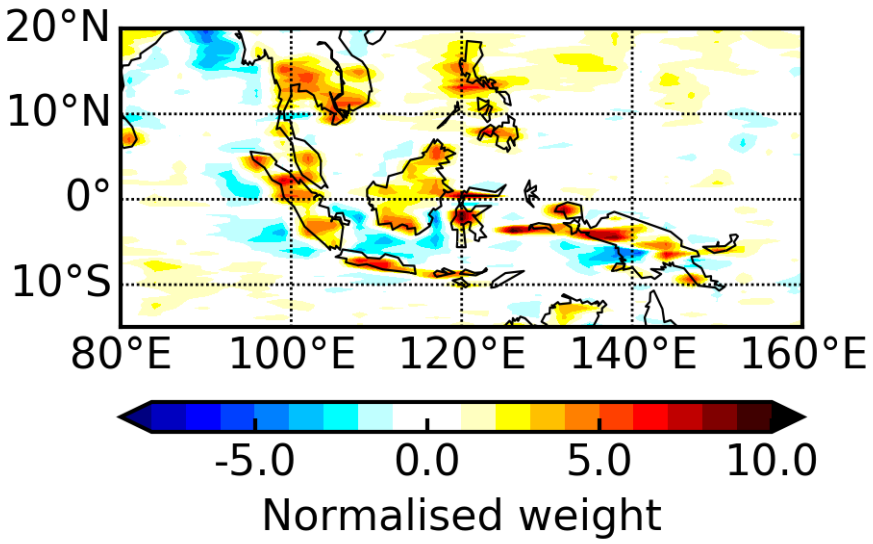

Figure 3.7. A zoom-in of Fig. 3.4b showing the second empirical orthogonal function over the Maritime Continent region bounded by 15° S–20° N and 80–160° E.

Although the patterns in the second EOFs of TOA albedo and OLR are remarkably similar in the Maritime Continent region, there are obvious differences in other regions. In particular, the marine stratocumulus regions located to the west of continental land masses exhibit negative weights in the TOA albedo EOF that do not appear in the OLR EOF. This signal appears to be related to the diurnal development and dissipation of marine stratocumulus clouds themselves, and is not apparent in the OLR since these variations occur close to the surface. The diurnal cycle of these clouds has been well characterised by ship track observations [*Burleyson et al.*, 2013] and more extensive field campaigns [*Boutle and Abel*, 2012] as having a maximum thickness overnight/during the morning and a minimum thickness during the afternoon/evening induced by solar absorption of the cloud layer, a process that is relatively well represented in weather and climate models [*Pfeifroth et al.*, 2012] and which appears to be captured by the model here. The fact that the diurnal cycles of convective cloud (e.g., in the Maritime Continent region) and marine stratocumulus cloud (e.g., to the

west of continental land masses) are present in the same pattern of variability is noteworthy in itself. Their opposite sign suggests that they are leading to compensating effects: the enhanced reflection from the development of convective cloud in the afternoon is compensated by the reduced reflection from dissipating marine stratocumulus cloud.

3.4.2.2 From GERB observations

Finally, we present a PCA of TOA albedo using GERB observations (Fig. 3.8) and compare it with results from the model data, noting that the modelled patterns are similar when subsampled over the GERB FOV (not shown). The leading pattern of variability remains very dominant, explaining 79.5 % of the variance. The first EOF (Fig. 3.8a) matches the patterns in the model data well, repeating the larger positive weights over the ocean, the south-east Atlantic marine stratocumulus region and equatorial Africa. The northward migration of the ITCZ between September (model fields) and July (GERB observations) is evident over Africa. The first PC (Fig. 3.8c) also matches the model's diurnally symmetric timing of this pattern associated with the SZA dependence.

The second pattern of variability, explaining 15.1 % of the variance, consists of an EOF (Fig. 3.8b) that contains similar features to those in the second EOF of OLR in the study by *Comer et al.* [2007] attributed to convective cloud development. However, just like the equivalent model EOF, this EOF also contains negative weights around the west coast of southern and central Africa and the south-east Atlantic related to the diurnal cycle of marine stratocumulus cloud. These patterns provide observational support that the compensating influences of convective and marine boundary layer cloud evolution on the TOA albedo are robust. The positive peak of the second PC (Fig. 3.8d), however, is shifted to slightly later in the day compared with the model results. The later timing of peak convection in reality compared to the model could be what is pulling the observational PC to later in the day, but the marine stratocumulus variations appear to follow the shift as well, suggesting that the stratocumulus could also be breaking up too early in the model. Unrealistic breaking up of marine stratocumulus in the Met Office model has been previously documented by *Allan et al.* [2007]. One consequence of this shift is that the peak in the second PC of TOA albedo appears to fall outside the 07:00–17:00 time window over which the albedo is defined

in the observations. In summary, the processes controlling the dominant patterns of variability in the diurnal cycle of TOA albedo appear to be consistent between the model and GERB observations.

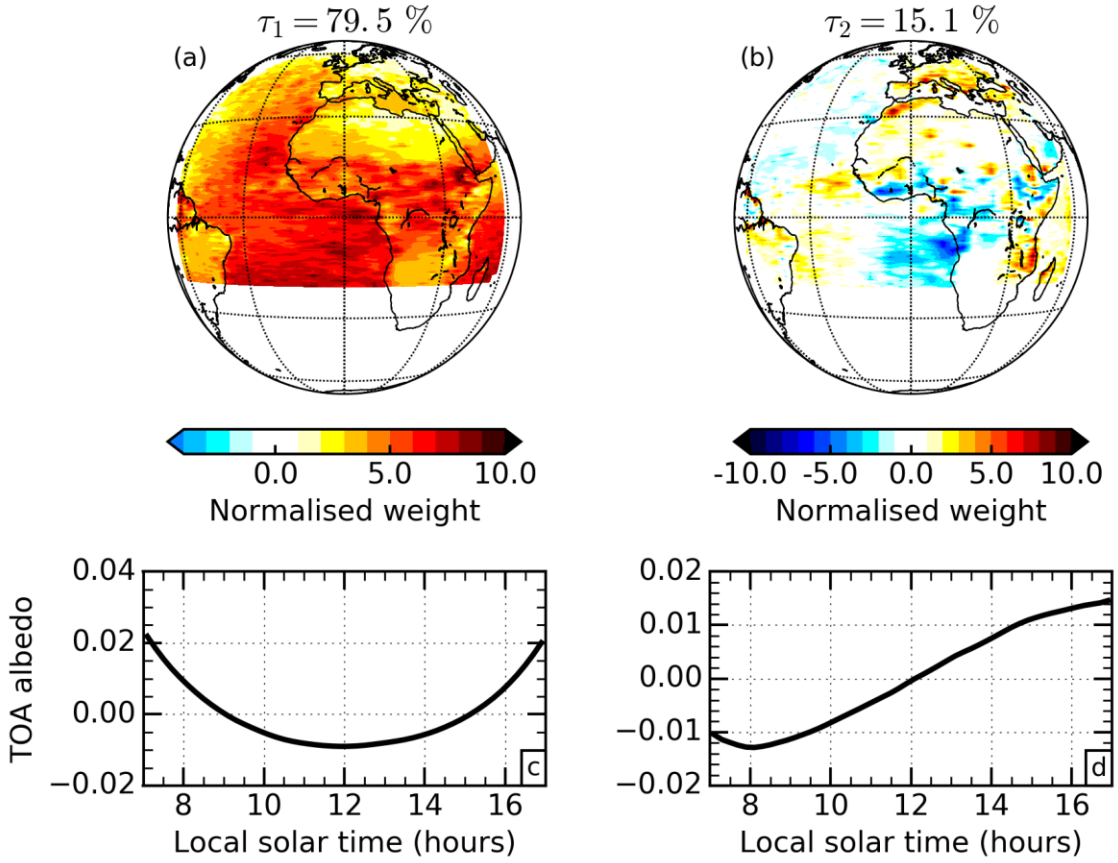

Figure 3.8. Principal component analysis of the top-of-atmosphere (TOA) albedo diurnal cycle for July 2006 in observations from the Geostationary Earth Radiation Budget instrument. The empirical orthogonal functions (a and b) and principal components (c and d) are presented for the first (a and c) and second (b and d) most dominant patterns of variability. The percentage variance explained by each mode is stated above the corresponding empirical orthogonal function.

The presence of distinctly different cloud variations in the same EOF is insightful in this case, but equally highlights a weakness in the PCA method for identifying unique physical processes. That is to say, if two or more physically independent processes are occurring approximately in phase, or indeed with opposing phase as is the case here, they become statistically linearly related and will be incorporated into the same pattern of variability. The unique identification of such processes then relies on revealing the

spatial and temporal coupling of the dominant patterns with other relevant geophysical variables, as examined next.

3.4.3 Coupled patterns of diurnal variability in EOR and other geophysical variables

The physical interpretation of the dominant pattern of variability in modelled TOA albedo was supported by additional surface albedo and clear-sky TOA albedo data fields as well as offline radiative transfer calculations. Thus far, however, the interpretation of the other modelled patterns presented in Sect. 3.4.1 and Sect. 3.4.2 (i.e., the two leading OLR patterns and the second TOA albedo pattern) has been limited to analysis of the EOFs and PCs alone, with the exception of some simplified calculations for the dominant OLR pattern. We now build a stronger argument for relating those statistical patterns to physical behaviour by assessing their extent of coupling with diurnal variability in other model variables directly related to the previously suggested behaviour.

3.4.3.1 OLR

The cross-correlation of the first PC of OLR and the first PC of the modelled surface temperature field reveals a very high and near-simultaneous correlation (Table 3.1, row 1), demonstrating that the temporal structures of these patterns are highly coupled. The reported lag time of −0.2 h represents a single 12 min model time step and the correlation is almost identical at no lag, so the lag of −0.2 h rather than 0 h likely has no physical relevance and the patterns can be considered to be simultaneously varying. Spatially, the first PC of OLR is highly correlated with the diurnal cycle of surface temperature at each grid point over land (Fig. 3.9a), indicating the spatial patterns are also highly coupled. Near the poles the diurnal cycle is poorly defined, leading to the spurious negative correlations. Over ocean there is no correlation because the model sea surface temperatures are prescribed from a fixed daily field and do not exhibit diurnal variability. This could be addressed in future work by considering a configuration of the model that is coupled to the ocean. If this was done we would expect some positive correlation over the oceans due to solar heating of the ocean surface, but the amplitude of the diurnal surface temperature change would be much weaker than that over land.

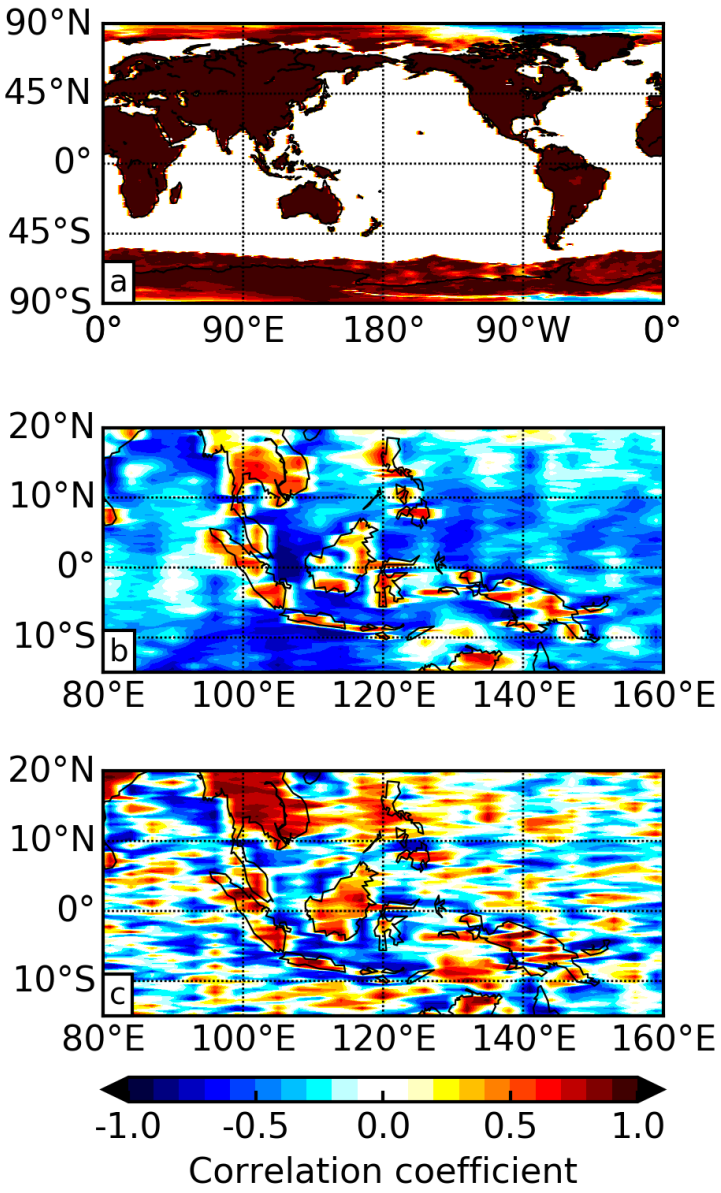

Figure 3.9. Heterogeneous correlation maps for (a) the first principal component of outgoing long-wave radiation and global surface temperature, (b) the second principal component of outgoing long-wave radiation and cloud liquid water path in the Maritime Continent region (reversed in sign to aid comparisons) and (c) the second principal component of top-of-atmosphere albedo and cloud liquid water path in the Maritime Continent region.

The cross-correlation of the second PC of OLR with the first PCs of modelled variables that are related to convective cloud development (LWP, IWP and CTH) reveals very high correlations but with substantial lag times (Table 3.1, rows 2– 4). A lag between

these variables is expected during convective cloud development, and the order in which the lags occur is consistent with the life cycle of a convective system. As locally driven convection initiates, water will begin to condense and cloud will develop at warm lower levels, causing the LWP to build first and the longest lag time. Once the convection breaks through the freezing level, further cloud development will mostly consist of ice crystals and the IWP will build, leading to a relatively shorter lag time. All the while, the vertical extent of the cloud is increasing and, as the convective system matures and produces an anvil, the CTH will reach a maximum, providing the shortest lag time. At this stage, as the convection dies and the CTH begins to reduce, one may expect the OLR to respond immediately but, curiously, a 3 h lag remains between the maximum correlation of OLR PC2 and CTH PC1.

Table 3.1. Maximum correlation coefficient and time lag at which it occurs from a cross-correlation between principal components (PCs) of modelled outgoing long-wave radiation (OLR) and PCs of modelled surface temperature, cloud liquid water path (LWP), cloud ice water path (IWP) and cloud top height (CTH).

	Correlation coefficient	Time lag (hours)
OLR PC1 vs. surface temperature PC1	0.998	–0.2
OLR PC2 vs. LWP PC1	–0.983	4.6
OLR PC2 vs. IWP PC1	–0.978	3.4
OLR PC2 vs. CTH PC1	–0.969	3.0

A possible explanation for this remaining lag is provided by considering the changes in the environment of the upper troposphere after the convection dissipates. As the anvil cloud horizontally entrains into surrounding clear-sky regions it will evaporate, leading to an increase in upper tropospheric humidity (UTH). Using 1 year of long-wave water vapour (6.7 μm) and window (11 μm) channel radiances from multiple geostationary satellites spanning global longitude, *Tian et al.* [2004] showed that deep convection in the tropics acts to moisten the upper troposphere via the evaporation of anvil clouds generated by deep convection. This increase in UTH can be prevalent over large spatial

extents and will delay the increase in OLR after the convective cloud has dissipated due to continued absorption of the more intense radiation originating from warmer, lower altitudes. The radiative heating that this provides leads to an increase in atmospheric stability and limits further cloud development, providing an important radiative-convective feedback mechanism for the diurnal cycle [*Stephens et al.*, 2008]. The study by *Tian et al.* [2004] suggested a lag of approximately 6 h between high cloud cover and UTH. In a similar but more spatially and temporally limited analysis, *Soden* [2000] suggested a lag time of approximately 2 h. In fact, the lag can be quite uncertain as it depends on the initial state of the atmosphere and spatial scale of convection [*Ingram*, 2015]. The 3 h lag found here falls between these values and suggests that diurnal variations in OLR due to convective activity may remain tied to the UTH even when the convective cloud itself has dissipated.

To assess the spatial correlations we return to the Maritime Continent region where we know there are strong diurnal cycles in convective activity. The second PC of OLR correlated with the diurnal cycle of LWP at each grid point (Fig. 3.9b) shows the highest correlations in the same regions as the largest weights in the second OLR EOF. This indicates that this pattern of OLR variability is highly coupled to diurnal cloud development in these regions, as expected. Similar patterns are seen for IWP and CTH.

3.4.3.2 TOA albedo

The cross-correlation of the second PC of TOA albedo with the first PCs of LWP, IWP and CTH reveals systematically higher correlations than the corresponding OLR correlations (Table 3.2). The order of the lag times amongst the cloud variables is maintained, but the lag times are shorter and only a 1 h lag remains between the TOA albedo and CTH. Unlike the OLR, the TOA albedo will not continue to respond in a similar way to the cloudy atmosphere once the cloud evaporates and the UTH increases. In fact, the opposite will occur as more solar radiation is absorbed in the humid environment. Remember that the second TOA albedo PC is also controlled by marine stratocumulus cloud that will not moisten the upper troposphere and may reduce the time lag between the variations in TOA albedo and CTH. The implication of this differing radiation response is that the diurnal changes in TOA albedo due to cloud development and dissipation are sharper and more immediate. Conversely, the OLR response is spread over a larger time and occurs later.

Table 3.2. Same as Table 3.1, but for modelled top-of-atmosphere (TOA) albedo.

	Correlation coefficient	Time lag (hours)
TOA albedo PC2 vs. LWP PC1	0.997	2.8
TOA albedo PC2 vs. IWP PC1	0.990	1.8
TOA albedo PC2 vs. CTH PC1	0.998	1.0

Similar to the second PC of OLR, the spatial correlation of the second PC of TOA albedo with the diurnal cycle of LWP at each grid point in the Maritime Continent region (Fig. 3.9c) shows the highest correlations in the same regions as the largest weights in the second TOA albedo EOF. Again, similar patterns are seen for the IWP and CTH in this region. In marine stratocumulus regions, however (not shown), the correlations are high for LWP but not for the other variables, demonstrating the value of assessing the extent of coupling with different data fields to identify unique physical processes. A schematic diagram summarising the dominant processes controlling the OLR and TOA albedo, and their relation to other variables, is provided in Fig. 3.10.

3.4.3.3 Lag times in GERB and SEVIRI observations

We finally present the equivalent correlations and lag times in GERB observations of OLR and TOA albedo and SEVIRI observations of CTH for July 2006, with an emphasis on qualitative comparisons with the model results due to the different time periods and spatial regions considered. The intention is to identify whether the correlations and lag times are broadly consistent, to build confidence that the model is capable of capturing the physics of diurnal evolution.

The observations (Table 3.3), just like the model (Tables 3.1 and 3.2), show that the magnitude of the maximum correlation coefficient with the CTH PC is larger for TOA albedo PC2 than OLR PC2. The lag time between the OLR PC2 and the CTH PC is 0.8 h longer in the observations than the model. For the TOA albedo, the lag time is the same. This supports the model finding that the TOA albedo responds more rapidly to cloud development than OLR and, if anything, suggests that the difference is even larger than the model indicates.

Table 3.3. Same as Table 3.1, but for OLR and TOA albedo retrieved from Geostationary Earth Radiation Budget (GERB) observations, and CTH retrieved from Spinning Enhanced Visible and InfraRed Imager (SEVIRI) observations.

	Correlation coefficient	Time lag (hours)
GERB OLR PC2 vs. SEVIRI CTH PC2	–0.961	3.8
GERB TOA albedo PC2 vs. SEVIRI CTH PC2	0.992	1.0

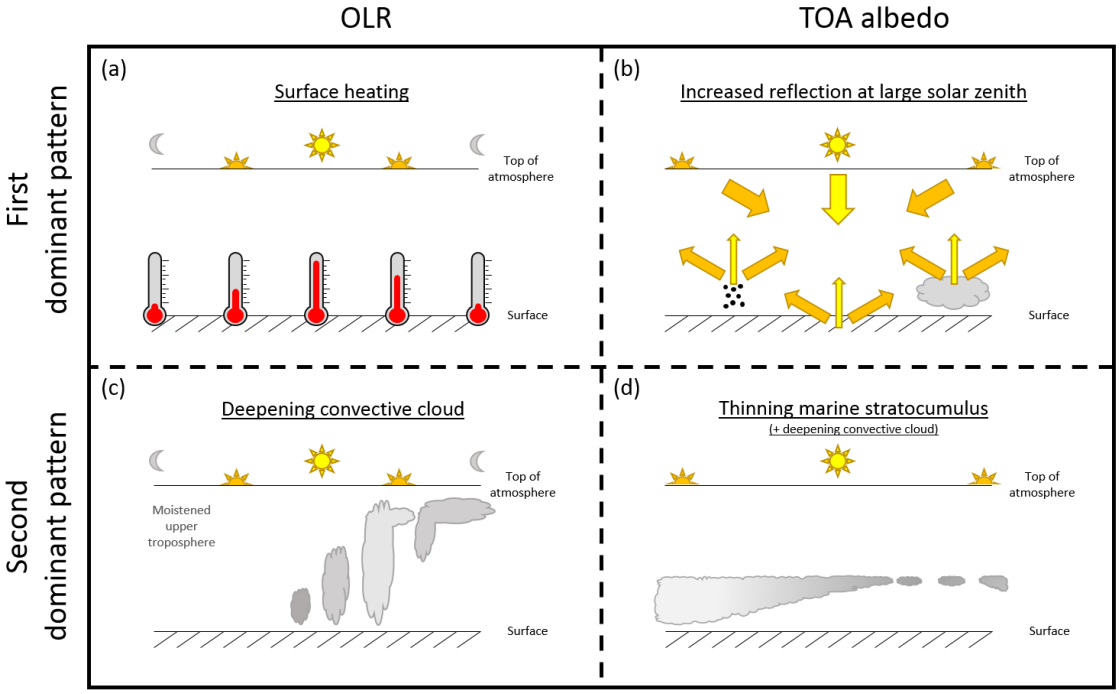

Figure 3.10. A schematic diagram showing the processes that control the first (a and b) and second (c and d) most dominant patterns in the diurnal variability of the outgoing long-wave radiation (OLR) (a and c) and top-of-atmosphere (TOA) albedo (b and d). Different arrow and Sun colours illustrate the change in solar zenith angle during the diurnal cycle and should not be interpreted as a change in wavelength. The separation of aerosol, surface and cloud reflection in the top right panel is for illustrative purposes only and does not relate to different parts of the diurnal cycle.

3.5 Summary (published abstract)

A globally complete, high temporal resolution and multiple-variable approach is employed to analyse the diurnal cycle of Earth's outgoing energy flows. This is made possible via the use of Met Office model output for September 2010 that is assessed alongside regional satellite observations throughout. Principal component analysis applied to the long-wave component of modelled outgoing radiation reveals dominant diurnal patterns related to land surface heating and convective cloud development, respectively explaining 68.5 % and 16.0 % of the variance at the global scale. The total variance explained by these first two patterns is markedly less than previous regional estimates from observations, and this analysis suggests that around half of the difference relates to the lack of global coverage in the observations. The first pattern is strongly and simultaneously coupled to the land surface temperature diurnal variations. The second pattern is strongly coupled to the cloud water content and height diurnal variations, but lags the cloud variations by several hours. We suggest that the mechanism controlling the delay is a moistening of the upper troposphere due to the evaporation of anvil cloud. The short-wave component of modelled outgoing radiation, analysed in terms of albedo, exhibits a very dominant pattern explaining 88.4 % of the variance that is related to the angle of incoming solar radiation, and a second pattern explaining 6.7 % of the variance that is related to compensating effects from convective cloud development and marine stratocumulus cloud dissipation. Similar patterns are found in regional satellite observations, but with slightly different timings due to known model biases. The first pattern is controlled by changes in surface and cloud albedo, and Rayleigh and aerosol scattering. The second pattern is strongly coupled to the diurnal variations in both cloud water content and height in convective regions but only cloud water content in marine stratocumulus regions, with substantially shorter lag times compared with the long-wave counterpart. This indicates that the short-wave radiation response to diurnal cloud development and dissipation is more rapid, which is found to be robust in the regional satellite observations. These global, diurnal radiation patterns and their coupling with other geophysical variables demonstrate the process-level understanding that can be gained using this approach and highlight a need for global, diurnal observing systems for Earth outgoing radiation in the future.

4 CHAPTER FOUR: Short-wave spectral radiation budget signatures and their physical controls

4.0 Statement of publication status

The material in this chapter has been prepared for publication, and will be submitted to a scientific journal in the near future. I will be the lead author of the manuscript. All figures and tables were generated by myself, and I led and finalised the scientific writing. I take full responsibility for the results. Other authors that will be listed on this publication have helped in the supply of radiative transfer tools and satellite observations, were involved in discussions of the methods and provided valuable feedback on the results. The following reference will be associated with the manuscript:

Gristey, J. J., J. C. Chiu, R. J. Gurney, K. P. Shine, S. Havemann, J.-C. Thelen, and P. G. Hill. (2018). Short-wave spectral radiation budget signatures and their physical controls.

The content of this chapter differs from the article prepared for publication in the following ways:

- The abstract is moved to the end of the chapter to provide a concise summary;
- The conclusions and summary are excluded from this chapter and are incorporated into Chapter 5;
- For consistency with the thesis structure, the numbers of the section headings, equations, figures and tables are updated, and minor format changes are applied.

Note that the introduction of this chapter contains minor overlaps with Chapter 1, but is included for completeness.

4.1 Introduction

Knowledge of the total reflected solar radiation (RSR) by Earth is vital for quantification of the global energy budget, and therefore essential for monitoring, predicting and understanding how our climate is evolving. As a result, RSR has been observed from satellites in its broadband form by dedicated energy budget missions for decades [*Barkstrom*, 1984; *Kyle et al.*, 1993; *Wielicki et al.*, 1996; *Harries et al.*, 2005]. These observations have revealed fundamental climate parameters such as the planetary

brightness [*Vonder Haar and Suomi*, 1971], have been extensively used in the understanding of climate forcing and feedbacks [*Futyan et al.*, 2005; *Loeb et al.*, 2007; *Brindley and Russell*, 2009; *Dessler*, 2013; *Ansell et al.*, 2014], and applied to evaluate and improve climate models [*Forster and Gregory*, 2006; *Tett et al.*, 2013b, 2013a; *Hartmann and Ceppi*, 2014].

Although the RSR has most commonly been observed in its broadband (i.e., spectrally integrated) form, it is fundamentally an intricate spectral quantity. Such intricacy results from wavelength specific interactions between the incoming solar radiation and various atmospheric gases, aerosols, clouds and the surface. Since it is often precisely these atmospheric and surface properties that we seek to understand from RSR measurements, the spectral dimension contains a vast amount of relevant information [*Feldman et al.*, 2011b; *Coddington et al.*, 2012; *King and Vaughan*, 2012]. The vast information content is not surprising given that specific wavelengths within the spectrum have been widely utilised in retrieval algorithms. However, observation and application of the entire spectrum for identifying underlying properties and processes of the Earth system important for the energy budget has arguably been underexploited.

A key motivation for further observation and application of spectrally resolved RSR is that processes leading to compensating spectral effects can become masked in a broadband measurement [*Hansen et al.*, 2005]. A good example of this is the observed symmetry in hemispherical albedo that has long been known [*Ramanathan*, 1987] but has become somewhat of a hot topic in recent years [*Voigt et al.*, 2013, 2014, *Stephens et al.*, 2015, 2016; *Haywood et al.*, 2016]. Essentially, the annual-mean broadband albedo of the Northern and Southern Hemisphere is identical, within measurement uncertainty, because reflection from a higher fraction of relatively bright land mass in the Northern Hemisphere is counteracted by reflection from a higher fraction of relatively bright clouds in the Southern Hemisphere. Although no differences can be detected in the hemispherical broadband albedo, clear differences do exist in the hemispherical spectral albedo [*Stephens et al.*, 2015]. These differences are due to the differing spectral reflectance properties of clouds and the surface. The spectral hemispherical albedo therefore clearly demonstrates the additional value of spectrally resolved information for revealing the signature of underlying properties that can become masked in equivalent broadband measurements, and warrants further investigation.

This study aims to identify detailed RSR spectral signatures, their relation to the underlying physical properties of the Earth system, and provide a route forward for using the entire spectrum to monitor the evolution of these properties. Central to achieving this aim is the computation of RSR spectra from satellite derived atmospheric and surface properties. Spectral features can then be directly related to the properties that produced them, building on previous work that has speculated on the physical cause of observed spectral structures in the outgoing short-wave radiance spectrum using knowledge of interactions between radiation and the Earth system [*Roberts et al.*, 2011]. Additionally, since the atmospheric and surface properties are observationally based, the spectral signatures are not subject to model biases, as could be the case in work that has looked at understanding the variability in spectral reflectance using scene properties derived from model simulations [*Roberts et al.*, 2013, 2014].

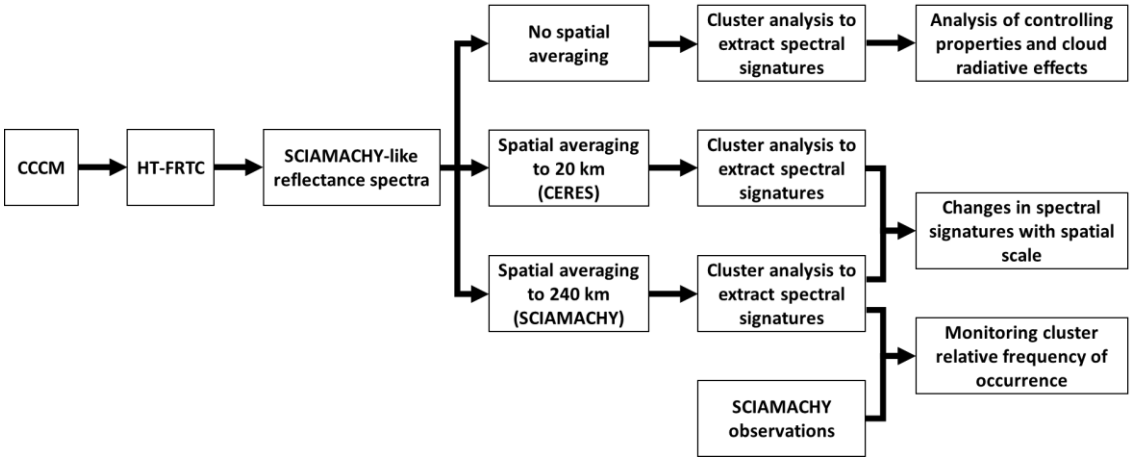

Figure 4.1. Workflow of this study. Scene properties derived from CloudSat-CALIPSO-CERES-MODIS (CCCM) are used as input for the Havemann-Taylor Fast Radiative Transfer Code (HT-FRTC) to compute SCIAMACHY-like reflectance spectra. The computations are spatially averaged to various relevant scales, and spectral signatures are extracted via clustering. At the finest spatial scale, a detailed analysis of the spectral signatures and their controlling properties is performed. Variations with spatial scale are also revealed, and signatures at 240 km spatial scale are used to monitor variability in SCIAMACHY observations. SCIAMACHY is the SCanning Imaging Absorption spectroMeter for Atmospheric CHartographY, CALIPSO is the Cloud-Aerosol Lidar and Infrared Pathfinder Satellite Observations, CERES is the Clouds and the Earth's Radiant Energy System and MODIS is the Moderate Resolution Imaging Spectroradiometer.

The remainder of this manuscript details the experiments performed to identify, understand and utilise the spectral signatures of RSR. The satellite datasets and radiative transfer tools used to compute and understand spectral variability are described alongside the method of extracting spectral signatures and relating them to physical properties in Sect. 4.2. The results are presented in Sect. 4.3. Specifically, distinct spectral signatures from computations, their controlling properties, and their relation to the short-wave cloud radiative effect (SWCRE) are revealed (Sect. 4.3.1), the variation of these signatures with the spatial scale of the computed spectra is examined (Sect. 4.3.2), and the utility of the identified signatures for understanding the variability in real spectral reflectance observations is investigated (Sect. 4.3.3). Finally, a brief summary is provided in Sect. 4.4. An overview of this workflow is provided in Fig. 4.1.

4.2 Data and methodology

4.2.1 Observed hyperspectral reflectance from SCIAMACHY

The SCanning Imaging Absorption spectroMeter for Atmospheric CHartographY (SCIAMACHY) was a hyperspectral imaging spectrometer that flew on the Sun-synchronous Environmental Satellite (ENVISAT) from 2002–2012, crossing the equator at 10:00 local time. It measured the incoming and reflected solar spectrum from the ultra-violet to the near-infrared at wavelengths of 214–2386 nm, with spectral resolution between 0.22 nm and 1.48 nm depending on the spectral region [*Gottwald and Bovensmann*, 2011]. The primary objective of SCIAMACHY was to perform global measurements for trace gas retrieval in the troposphere and stratosphere, but the measurements have also been used to detect cloud and aerosol properties [*Kokhanovsky et al.*, 2005; *von Hoyningen-Huene et al.*, 2007]. The narrow spectral bands used for trace gas retrieval are available with relatively short measurement integration times, leading to spatial resolution of around 26 × 30 km. However, the full spectrum is only available with longer measurement integration times, giving a nadir footprint of around 30 × 240 km.

In this study, we extract version 8 SCIAMACHY nadir observations and examine their variability alongside radiative transfer computations. The SCIAMACHY measures a spectral radiance, $I_{\lambda,\mathrm{SCIA}}$, but, to remove the spectral shape and magnitude of the

incoming solar spectrum, we extract a spectral reflectance, $R_{\lambda,\mathrm{SCIA}}$. This spectral reflectance is calculated within the SCIAMACHY product as

$$R_{\lambda,\mathrm{SCIA}} = \frac{\pi I_{\lambda,\mathrm{SCIA}}}{S_{\lambda,\mathrm{SCIA}} \cos(\theta)}, \quad (4.1)$$

Where $S_{\lambda,\mathrm{SCIA}}$ is the observed SCIAMACHY incoming solar irradiance that is updated daily; θ is the solar zenith angle; and an assumption of isotropic radiation has been made. The radiation variables are all a function of wavelength, λ.

Several exclusions and modification are applied to the extracted data. Firstly, because the upper end of the SCIAMACHY spectrum suffered from unreliable optical throughput due to ice deposits on the detectors [*Gottwald and Bovensmann*, 2011], we exclude that end of spectrum and focus on the spectral range from 250–1750 nm only. Secondly, spurious signal within this spectral range is filtered out by removing reflectance associated with large differences (> 20 %) at neighbouring wavelengths. This threshold is found to effectively remove the spurious signal while retaining the sharpest real spectral variability at the SCIAMACHY native spectral resolution. Finally, the SCIAMACHY spectral reflectance are gridded back to a consistent 1 nm spectral resolution. This has been shown to be ample resolution to retain the variance contributions from the dominant components of spectral variability [*Roberts et al.*, 2011].

4.2.2 Computed hyperspectral reflectance

4.2.2.1 Input from A-Train satellite observations

To improve understanding of the physical controls on spectral RSR variability, radiative transfer computations of SCIAMACHY-like reflectance spectra are performed using input derived from Afternoon-Train (A-Train) satellite measurements. Specifically, we use release B1 of the CloudSat-CALIPSO-CERES-MODIS (CCCM) product [*Kato et al.*, 2010, 2011], which collocates irradiance derived from the Clouds and the Earth's Radiant Energy System (CERES) with cloud, aerosol and surface properties retrieved from the CloudSat Cloud Profiling Radar (CPR), the Cloud-Aerosol Lidar and Infrared Pathfinder Satellite Observations (CALIPSO) Cloud-Aerosol Lidar with Orthogonal Polarization (CALIOP), and the Moderate Resolution Imaging Spectroradiometer (MODIS). The product was designed to provide detailed

cloud and aerosol profiles that agree better with the observed radiative fluxes and thus is well suited for process studies.

Among these sensors, the CERES has the largest footprint size of ~20 km. Within each CERES footprint, up to 16 groups (henceforth referred to as "CCCM groups") containing either clear-sky or different vertical profiles of cloud are determined, based on their cloud boundaries (see *Kato et al.* [2010] for details). For each CCCM group that contains cloud, the mean cloud properties from the CPR, CALIOP and MODIS at a spatial resolution of 1 km are combined, using the method described in *Bodas-Salcedo et al.* [2016], resulting in liquid/ice water content and effective radii profiles at a vertical resolution of ~240 m. Other than the cloud profiles, all properties are horizontally uniform across the CERES footprint. These properties include vertical profiles of aerosol extinction derived from CALIOP and MODIS, surface spectral reflectance derived from MODIS and vertical profiles of atmospheric temperature and gases that are added to the CCCM dataset from the Goddard Earth Observing System Model (GEOS) reanalysis.

To understand radiative signatures under a variety of surface, atmospheric and cloud conditions, we extracted the CCCM data for all seasons in 2010, and for the region bounded by 20° W to 20° E and 0° N to 30° N, henceforth referred to as "West Africa". The year of 2010 was chosen because the West African monsoon was particularly active during this year (see Fig. 4.14a), providing the possibility to extract a diverse range of atmospheric signatures across the West Africa region. The West Africa region was chosen because it has attracted substantial scientific interest in recent years due to complex atmospheric physics, poor climate model performance and a growing population [*Knippertz et al.*, 2015; *Hill et al.*, 2016, 2018; *Hannak et al.*, 2017]. The diverse surface types in West Africa (from dark ocean, to vegetated surface, to bright desert) and comprehensive cloud systems (from marine boundary layer clouds, to multi-layer clouds, to deep convective clouds [*Stein et al.*, 2011]) also provide variety to ensure the representativeness of our spectral signature extraction. One important physical property not represented in this region is snow-covered surfaces. It is expected that the dataset described by *Bodas-Salcedo et al.* [2016] will be extended globally in the future to address this issue.

For the data in West Africa that are used here, several exclusions are applied. Firstly, only the daytime observations are selected given that it is only the short-wave reflectance that we compute. Secondly, if the cloud phase and temperature profiles are unphysical (i.e., water cloud at temperatures below 233 K and ice cloud at temperatures above 273 K), that cloud group is excluded from the analysis. Thirdly, if the fraction of the CERES footprint occupied by a cloud group is less than 10 %, the vertical profile of ice and liquid water content is found to be unreliable, so that cloud group is excluded. When cloud groups are excluded, the CERES footprint is considered to contain only the remaining cloud groups with their relative field-of-view fraction maintained. Finally, surface reflectance is not provided over ocean by the CCCM product, so a spectrally flat surface reflectance of 0.2 is used for any computations over an ocean surface.

4.2.2.2 Fast radiative transfer code

Using the detailed scene properties provided by CCCM as input, the corresponding SCIAMACHY-like reflectance spectra are computed by a fast radiative transfer code, called the Havemann-Taylor Fast Radiative Transfer Code (HT-FRTC) [*Havemann et al.*, 2018]. The HT-FRTC is a diverse code that can be applied throughout the electromagnetic spectrum from the ultraviolet to the microwave. The speed, which is necessary to avoid prohibitive computation time for a large number of hyperspectral computations, relies on the generation of principal components during an initial training phase.

During the training phase, monochromatic radiances are computed at very high spectral resolution, similar to that of conventional line-by-line models, for a diverse range of atmospheric and surface properties. The atmospheric properties are from the European Reanalysis (ERA) Interim [*Dee et al.*, 2011] and are randomly combined with surface properties from the Advanced Spaceborne Thermal Emission and Reflection Radiometer (ASTER) spectral library [*Baldridge et al.*, 2009]. A principal component analysis is applied to these monochromatic computations to extract the principal components that represent most of the spectral variability. Each principal component is a high resolution spectrum. The leading 300 principal components are retained here.

Once the training phase is complete, the HT-FRTC is called with the CCCM atmospheric and surface properties as input, and seeks principal component scores, or weights, of each of the 300 principal components. To do this, a limited set of

monochromatic radiance computations are performed using the CCCM input at specific wavelengths. The specific wavelengths are pre-selected using a clustering algorithm that identifies wavelengths with similar variations. These limited computations are then used as predictors for the principal component scores by performing a regression of the limited computations on to the principal components. Finally, to provide a realistic constraint for the spectral characteristics of an instrument, the principal components are averaged over the spectral response functions of the SCIAMACHY instrument. Using the principal component scores and the averaged principal components, a SCIAMACHY-like radiance spectrum is re-constructed.

As discussed in Sect. 4.2.1, we are interested in reflectance spectra, rather than radiance spectra. The computed SCIAMACHY-like reflectance spectrum at a given cloud group in the CCCM dataset, $R_{\lambda,CCCM-1km}$, is given by

$$R_{\lambda,CCCM-1km} = \frac{\pi I_{\lambda,CCCM-1km}}{s^* S_{\lambda,0}\, cos(\theta)}, \tag{4.2}$$

where $I_{\lambda,CCCM-1km}$ is the computed SCIAMACHY-like outgoing radiance spectrum at the top-of-atmosphere for a given CCCM group; s^* is a factor close to unity that accounts for variations in the Earth-Sun distance; and $S_{\lambda,0}$ is the incoming solar irradiance spectrum from *Kurucz and Bell* [1995] used in HT-FRTC and is averaged over the SCIAMACHY spectral response functions. Similar to Eq. (4.1), an isotropic assumption is made, and the radiation variables are all a function of wavelength, λ, that extends from 250–1750 nm and is gridded at a 1 nm spectral resolution, consistent with the real SCIAMACHY observations described in Sect. 4.2.1.

Since the set of $R_{\lambda,\mathrm{CCCM-1km}}$ spectra are based on cloud profiles at the best spatial resolution, we will discuss their characteristics and associated controlling factors in more detail in Sect. 4.3.1. However, as mentioned earlier, the SCIAMACHY has a much coarser horizontal resolution of 240 km, and thus averaging of computed spectra is required to better match SCIAMACHY observations. We first calculate the mean reflectance for each CERES footprint at a horizontal resolution of around 20 km, $R_{\lambda,\mathrm{CCCM-20km}}$, by summing up the computations for individual CCCM groups weighted by their fraction, F, i.e.,

$$R_{\lambda,CCCM-20km} = \sum_{i=1}^{M} F_i \times R_{\lambda,CCCM-1km,i}, \quad (4.3)$$

where i and M represent the index of the group and the total number of CCCM groups, respectively. By averaging $R_{\lambda,\mathrm{CCCM-20km}}$ over twelve consecutive CERES footprints that form a long strip of around 240 km, the mean $R_{\lambda,\mathrm{CCCM-240km}}$ represents spectra at the SCIAMACHY spatial resolution and is given by

$$R_{\lambda,CCCM-240km} = \frac{\sum_{j=1}^{12} R_{\lambda,CCCM-20km_j}}{12}, \quad (4.4)$$

where j is the CERES footprint index. Only cases where 12 consecutive CERES footprints are available are included, which is sometimes not possible if entire CERES footprints are excluded (see Sect. 4.2.2.1), or if the edge of the West Africa domain is reached. Each new $R_{\lambda,CCCM-240km}$ is started from a new $R_{\lambda,CCCM-20km}$ such that all computed SCIAMACHY-like reflectance spectra at the SCIAMACHY footprint scale are independent. Equations (4.3) and (4.4) introduce inhomogeneity in the along-track direction only, therefore, homogeneity remains in the cross-track direction.

Note that while CCCM provides information on seven common aerosol species (soluble and insoluble particles, small and large dust particles, sulfuric acid, sea salt, and soot), only four of them (large dust particles, small dust particles, sulphate, and sea salt) are used in our radiative transfer computations, since their optical properties have been included in the training phase of the radiative transfer code. Training for other aerosol types is in progress, which will allow inclusion of all aerosol types in the future.

4.2.3 Radiative signature clustering

To identify distinct spectral signatures, a k-means clustering algorithm [*Anderberg*, 1973] is applied to the computed SCIAMACHY-like reflectance spectra. The k-means clustering works here by minimising the distance between a pre-defined number of clusters, represented by cluster centroids, and a set of spectra. This technique has been widely used for identifying clusters of CloudSat reflectivity profiles in the tropics [*Zhang et al.*, 2007; *Young*, 2015] and identifying "weather states" from joint cloud top height-cloud optical depth histograms [*Jakob and Tselioudis*, 2003; *Williams and Tselioudis*, 2007; *Williams and Webb*, 2009; *Oreopoulos et al.*, 2014]. However, cluster

analysis applied to short-wave reflectance spectra, allowing objective identification of scenes based purely on radiative signature, has not been presented previously. Compared to cluster analyses that are based on measurements or retrieval at select wavelengths, the advantage of using the entire spectrum is to capture all important features for controlling the total RSR together.

The appropriateness of cluster numbers and their relationships with the underlying atmospheric and surface properties are evaluated using the CCCM input. Specifically, the atmospheric and surface properties used in the computed SCIAMACHY-like reflectance spectra belonging to each cluster are separated. Knowing the exact atmospheric and surface properties used for each computation provides an opportunity to investigate the precise controlling properties of the spectra, not possible from spectral reflectance observations alone.

As well as performing cluster analysis on the computed SCIAMACHY-like reflectance spectra from each CCCM group (i.e., $R_{\lambda,\mathrm{CCCM-1km}}$ from Eq. (4.2)), we also perform cluster analysis on the computed SCIAMACHY-like reflectance spectra averaged over spatial scales of 20 km (i.e., $R_{\lambda,\mathrm{CCCM-20km}}$ from Eq. (4.3)) and 240 km (i.e., $R_{\lambda,\mathrm{CCCM-240km}}$ from Eq. (4.4)), to examine how the results change with spatial scale. Using the clusters at the 240 km scale, that is similar to the footprint of the SCIAMACHY instrument, we next seek to gain insight into the controlling properties of real SCIAMACHY spectral reflectance observations. Specifically, we assign SCIAMACHY observations to the clusters and monitor changes in the relative frequency of occurrence of the clusters with time. Each SCIAMACHY observation is assigned to the cluster for which the root-mean-square difference (RMSD) between the cluster centroid and the SCIAMACHY observation is smallest. The RMSD is defined as

$$RMSD = \sqrt{\frac{\sum_{\lambda=1}^{N}(R_{\lambda,SCIA} - R_{\lambda,CCCM-240km,centroid})^2}{N}}, \qquad (4.5)$$

where $R_{\lambda,\mathrm{CCCM-240km,centroid}}$ is a given centroid from the cluster analysis of $R_{\lambda,\mathrm{CCCM-240km}}$; and N is the total number of wavelengths.

Finally, we note that if the clusters are separated by different cloud regimes (which is sometimes the case, as will be shown in Sect. 4.3.1), the cluster centroids will be

associated with the signature of the SWCRE. Understanding and monitoring the SWCRE is crucial for determining the impact of cloud in current and future climate, so we consider quantifying the average SWCRE of clusters associated with different cloud regimes to be a useful exercise. Using radiative transfer, the spectral SWCRE of a given CCCM group, denoted $SWCRE_{\lambda,\mathrm{CCCM-1km}}$, is quantified explicitly by re-computing all of the SCIAMACHY-like radiance spectra with the cloud removed, $I_{\lambda,\mathrm{CCCM-1km,cloud\ free}}$. The corresponding cloud-free SCIAMACHY-like reflectance spectra, $R_{\lambda,\mathrm{CCCM-1km,cloud\ free}}$, are calculated in the same way as before using Eq. (4.2), but with $I_{\lambda,\mathrm{CCCM-1km,cloud\ free}}$ instead of $I_{\lambda,\mathrm{CCCM-1km}}$. The spectral SWCRE, in reflectance space, are then given as

$$SWCRE_{\lambda,\mathrm{CCCM-1km}} = R_{\lambda,\mathrm{CCCM-1km}} - R_{\lambda,\mathrm{CCCM-1km,cloud\ free}}, \quad (4.6)$$

and the spectrally integrated SWCRE in units of W m^{-2}, denoted $SWCRE_{all,\mathrm{CCCM-1km}}$, are given as

$$SWCRE_{all,\mathrm{CCCM-1km}} = \pi \int_1^N I_{\lambda,\mathrm{CCCM-1km}} d\lambda - \pi \int_1^N I_{\lambda,\mathrm{CCCM-1km,cloud\ free}} d\lambda. \quad (4.7)$$

Using Eq. (4.3) and (4.4), but starting with $R_{\lambda,\mathrm{CCCM-1km,cloud\ free}}$ instead of $R_{\lambda,\mathrm{CCCM-1km,}}$, an equivalent set of cloud-free reflectance spectra are generated at the spatial scales of 20 and 240 km. Similarly, the spectral and spectrally integrated SWCRE at these spatial scales are given by Eq. (4.6) and (4.7), but replacing the subscript 1 km with 20 and 240 km, respectively. We present the mean spectral and spectrally integrated SWCRE of all computed SCIAMACHY-like reflectance spectra belonging to each cluster, at each spatial scale.

4.3 Results

4.3.1 Clusters of computed reflectance spectra

4.3.1.1 Spectral signatures and their controlling properties

Clustering of more than 90,000 computed SCIAMACHY-like reflectance spectra for individual CCCM groups over West Africa leads to the 10 centroids shown in Fig. 4.2. We have found that the choice of 10 clusters works appropriately to separate signatures emerging from the surface, liquid cloud and ice cloud. For all clusters, gas absorptions are evident; for example, there are relatively broad water vapour absorption bands

around 0.93, 1.13 and 1.39 μm, and sharp oxygen A and B absorption bands centred at 0.762 and 0.688 μm, respectively. As expected, the cluster analysis not only captures the differences in the magnitude of the spectrum (e.g., the 'darker' spectrum in cluster 5 versus the 'brighter' spectrum in cluster 10), but also the shape (e.g., the relatively flat spectrum in cluster 4 versus the largely swinging spectrum in cluster 9). These distinct spectral differences are associated with the underlying controlling properties, which are discussed in detail next.

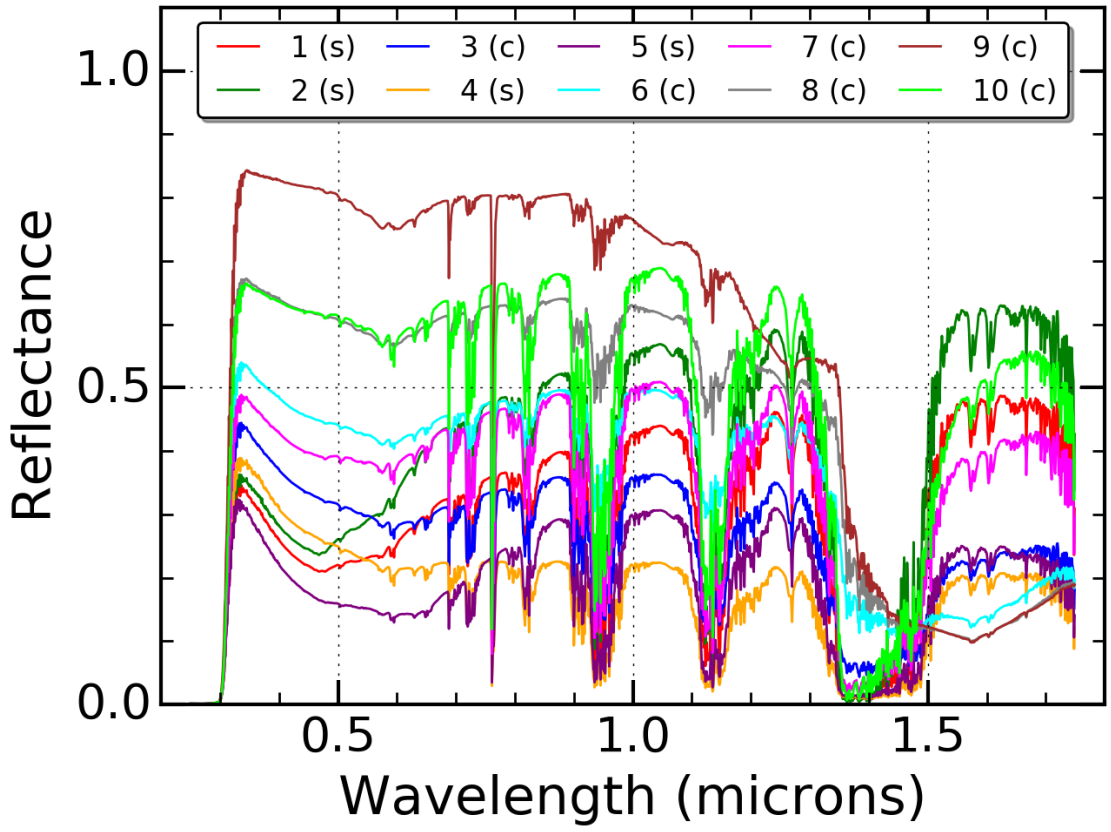

Figure 4.2. Cluster centroids of top-of-atmosphere reflectance spectra. Ten clusters are shown, based on 90,917 computed SCIAMACHY-like reflectance spectra that are re-gridded to a 1 nm spectral resolution. Input for the computations is derived from Afternoon-Train satellite observations over West Africa in 2010. Computations are performed using the Havemann-Taylor Fast Radiative Transfer Code. The clusters are numbered in the legend according to their population, from most to least populated, and are designated as either surface (s) or cloud (c); further details are provided in Table 4.1. SCIAMACHY is the SCanning Imaging Absorption spectroMeter for Atmospheric CHartographY.

Table 4.1. Summary of the 10 clusters presented in Fig. 4.2 and their dominating properties. Based on 90,917 computed SCIAMACHY-like reflectance spectra over West Africa in 2010.

Cluster number	Number of spectra	Assigned colour	Comment on controlling property	Designated as surface or cloud dominated?
1	12408	Red	Desert	Surface
2	11882	Green	Bright desert (sand dunes)	Surface
3	11528	Blue	Vertically distributed but optically thin cloud, mostly ice, over dark surface	Cloud
4	10816	Orange	Ocean	Surface
5	9258	Purple	Vegetation	Surface
6	9045	Cyan	Ice cloud	Cloud
7	8487	Magenta	Vertically distributed but optically thin cloud, mostly liquid	Cloud
8	8267	Grey	Optically thick ice cloud	Cloud
9	5872	Brown	Very optically thick ice cloud	Cloud
10	3354	Lime	Liquid cloud	Cloud

The clusters fall into two broad categories: those dominated by surface reflectance (henceforth "surface clusters") and those dominated by cloud reflectance (henceforth "cloud clusters"); see Table 4.1. As shown in Fig. 4.3–4.5, the surface clusters (Clusters 1, 2, 4 and 5) tend to have relatively small spread in surface reflectance, are highly constrained to certain locations, and contain very little cloud. Cluster 1, with the largest sample size, represents signatures mainly associated with desert surface reflectance that increases from 0.2 in the visible to 0.5 in the near-infrared (Fig. 4.3a). The standard deviation of surface reflectance in this cluster is less than 0.1 at all wavelengths. As shown in Fig. 4.4a, spectra from Cluster 1 predominantly originate from outskirts and rocky hamada of the Sahara desert (i.e., elevated stone plateaus where most of the sand has been removed by deflation), with notable gaps over brighter surfaces containing sand dunes. Data points over these sand dunes missed by Cluster 1 are captured by Cluster 2 (Fig. 4.4b), where the shape of the surface reflectance spectrum is similar to that in Cluster 1, but with a larger magnitude (Fig. 4.3b). In contrast to Clusters 1 and 2 that represent signatures from bright surfaces, Clusters 4 and 5 represent signatures from darker ocean and vegetation surfaces, respectively, as confirmed by locations of the spectra in Fig. 4.4d and e. Not surprisingly, the ocean surface represented by cluster 4 has a spectrally flat surface reflectance value of 0.2 (Fig. 4.3d), resulting from the default value used due to the lack of surface albedo retrieval from MODIS (see Sect. 4.2.2.1). The vegetated surface represented by Cluster 5 exhibits a sudden jump in surface reflectance around 0.67 μm (Fig. 4.3e), commonly referred to as the "red edge". Overall, all of these surface clusters have mean vertically integrated cloud water content less than 10 g m^{-2} (Fig. 4.5a, b, d and e), allowing the underlying surface to be the primary factor that controls the top-of-atmosphere reflectance spectra.

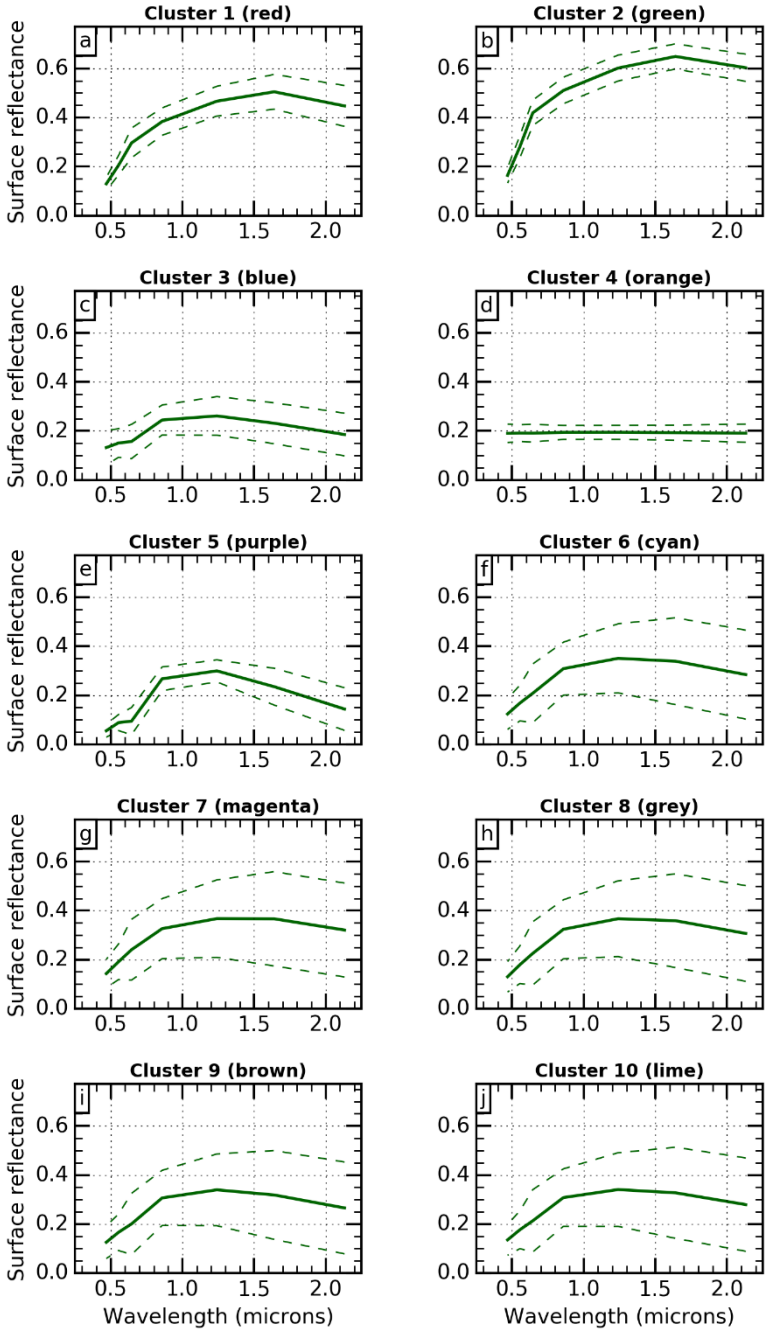

Figure 4.3. The mean surface spectral reflectance used in computed SCIAMACHY-like reflectance spectra belonging to each of the 10 clusters presented in Fig. 4.2. The corresponding cluster number and assigned colour is given above each plot. The dashed lines represent one standard deviation either side of the mean. SCIAMACHY is the SCanning Imaging Absorption spectroMeter for Atmospheric CHartographY.

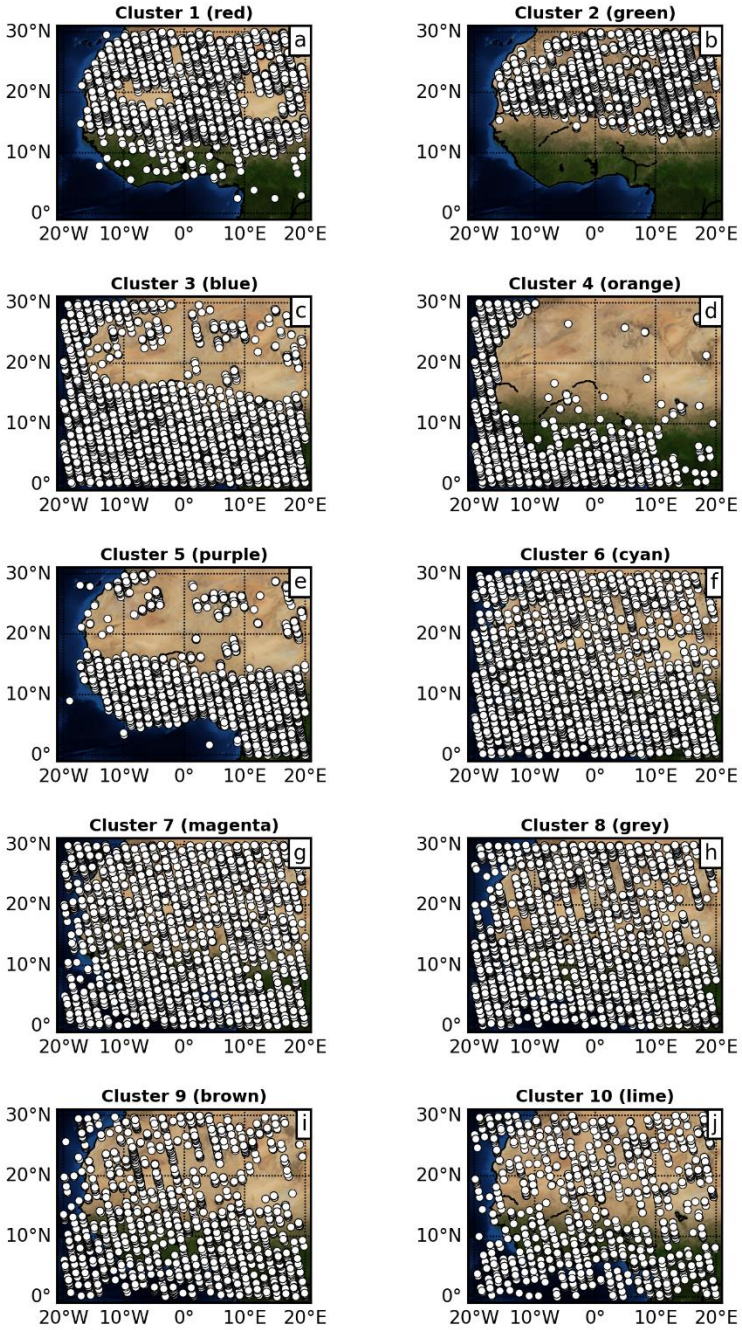

Figure 4.4. The location of the computed SCIAMACHY-like reflectance spectra belonging to each of the 10 clusters presented in Fig. 4.2. Each location is represented by a white dot. The background map is based on the true-colour "blue marble" image [*Stockli et al.*, 2005]. The corresponding cluster number and assigned colour is given above each plot. SCIAMACHY is the SCanning Imaging Absorption spectroMeter for Atmospheric CHartographY.

In contrast, the cloud clusters (Clusters 3, 6–10) all contain a substantial amount of cloud water on average, can be less well constrained by location and therefore typically exhibit large spread in spectral surface reflectance. Let us start by examining the centroids of Clusters 6, 8 and 9 (Fig. 4.2), which are associated with relatively large reflectance up until 1.3 μm but with a rather different spectral shape in the region between 1.3 and 1.7 μm compared to other centroids. Since ice absorption is much stronger than liquid absorption around 1.6 μm and much weaker around 1.4 microns [*Pilewskie and Twomey*, 1987], the reduced reflectance around 1.6 μm and increased reflectance around 1.4 microns for these centroids indicates the presence of ice clouds. This is confirmed by their average cloud profiles (Fig. 4.5f, h and i), revealing predominantly ice cloud with varying ice water paths that peak in ice water content at ~11 km altitudes.

Compared to the aforementioned clusters dominated by ice clouds, the centroid of Cluster 10 has similar magnitudes of reflectance up until 1.3 μm, but lower around 1.4 μm and higher around 1.6 μm (Fig. 4.2). The generally large reflectance throughout the spectrum and opposite spectral signature to ice cloud between 1.3 and 1.7 μm in Cluster 10 indicates the presence of liquid clouds and the absence of ice clouds, as confirmed by Fig. 4.5j.

The centroids of Clusters 3 and 7 have similar spectral shapes to that of Cluster 10, but with a generally smaller magnitude (Fig. 4.2), indicating that clouds are optically thinner in these two clusters than Cluster 10. The lower reflectance in the ice absorption band in Cluster 3 than Cluster 7 also suggests that Cluster 3 contains more ice cloud on average, while cluster 7 contains more liquid cloud. Given that the cloud is optically thinner on average in these two clusters, it is possible that the surface reflectance can still have a substantial influence on the top-of-atmosphere spectral signature. Evidence for this is provided by the location of the spectra in Cluster 3 (Fig. 4.4c), which avoid the brightest desert surfaces. Cluster 7 is not as constrained by location (Fig. 4.4g). It is likely that Cluster 3 is more constrained by location than Cluster 7 because it contains more ice cloud with strong absorption around 1.6 microns, which coincides with the brightest spectral region of desert surface reflectance.

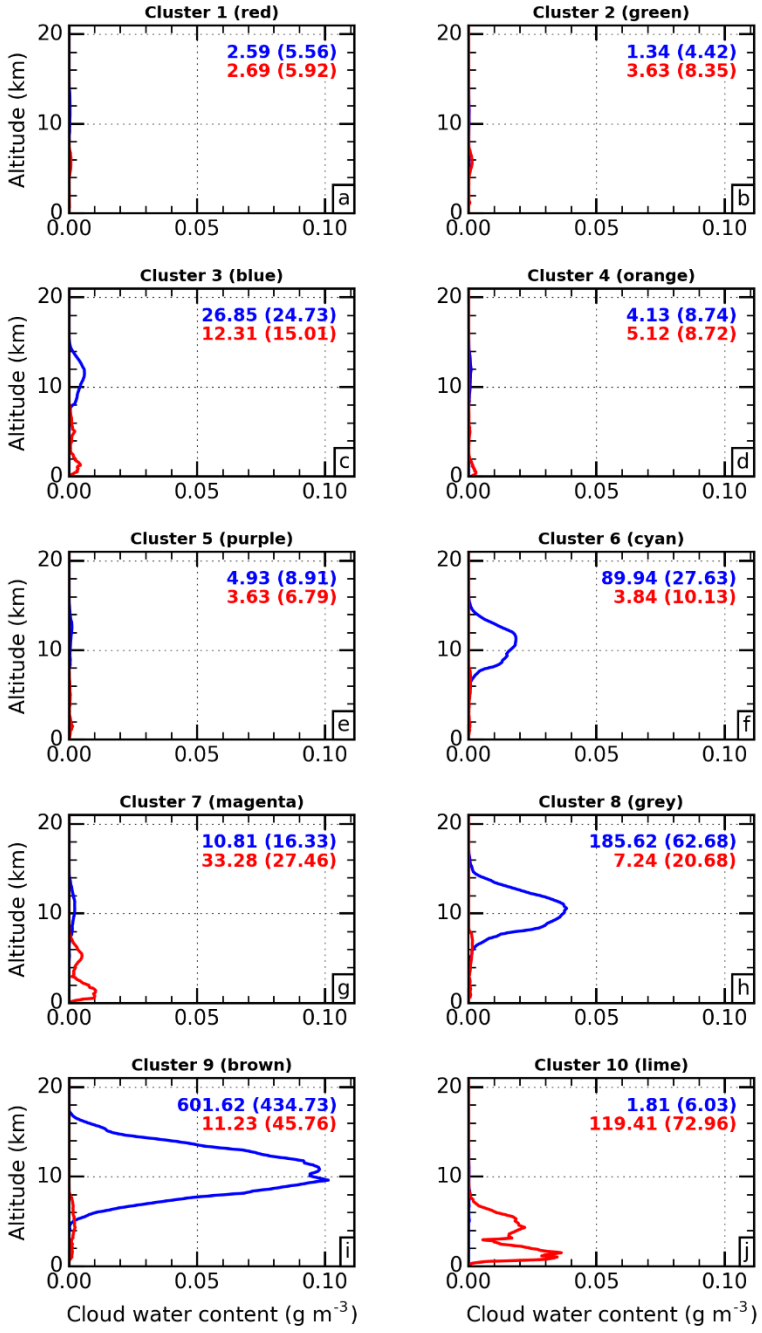

Figure 4.5. The mean vertical profile of ice (blue) and liquid (red) cloud water content used in computed SCIAMACHY-like reflectance spectra belonging to each of the 10 clusters presented in Fig. 4.2. The vertically integrated ice and liquid water content for the mean cloud vertical profile of each cluster is displayed on each plot, along with the standard deviation of individual vertically integrated liquid and ice water contents in brackets, both in g m^{-2}. The corresponding cluster number and assigned colour is given above each plot. SCIAMACHY is the SCanning Imaging Absorption spectroMeter for Atmospheric CHartographY.

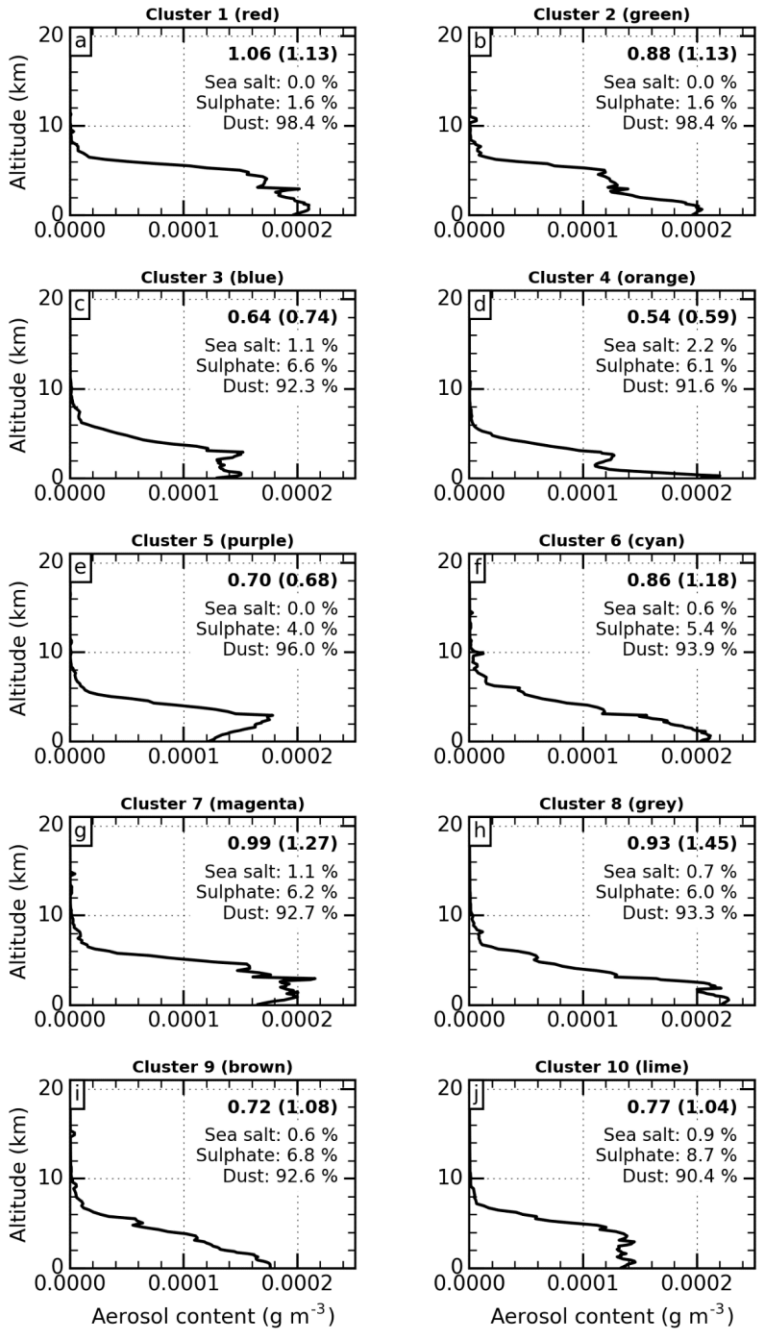

Figure 4.6. The mean vertical profile of aerosol content used in computed SCIAMACHY-like reflectance spectra belonging to each of the 10 clusters presented in Fig. 4.2. The vertically integrated aerosol content for the mean aerosol vertical profile of each cluster is displayed on each plot, along with the standard deviation of individual vertically integrated aerosol contents in brackets, both in g m^{-2}. Sea salt, sulphate and dust are included, and their mean relative percentage, by mass, is also displayed on each plot. The corresponding cluster number and assigned colour is given above each plot. SCIAMACHY is the SCanning Imaging Absorption spectroMeter for Atmospheric CHartographY.

Similar to the average vertical profiles of cloud, the average vertical profiles of aerosol are also shown for each cluster in Fig. 4.6. However, it appears that of the 10 clusters extracted, none of them are dominated by aerosol-radiation interactions. The mean total aerosol loading for each cluster, in g m^{-2}, is within one standard deviation either side of the mean for any other cluster. Any differences that do exist in the aerosol profiles appear to be a by-product of the location of the spectra that is, as discussed, mostly controlled by the surface reflectance properties. For example, the highest mean percentage of sea salt is found in Cluster 4, but this is because Cluster 4 is predominantly controlled by low ocean surface reflectance. The absence of aerosol signature in our cluster analysis is perhaps surprising given that the region of West Africa is associated with diverse aerosol types and loadings [*Knippertz et al.*, 2015]. However, note that of the aerosol types considered here, the variety is dominated by dust, which constitutes over 90 % of the mean aerosol loading for all clusters (Fig. 4.6).

4.3.1.2 Cloud radiative effects of each cluster

Given that the clusters are typically distinguished by either surface signatures, or signatures that are related to different cloud structures, the computed SCIAMACHY-like reflectance spectra within these clusters should therefore exhibit, on average, distinct spectral SWCRE. Figure 4.7 shows the mean spectral SWCRE associated with each cluster. As expected, SWCRE are small throughout the spectrum for surface clusters, due to their low cloud amount. The mean broadband SWCRE in all of the surface clusters is less than 30 W m^{-2}.

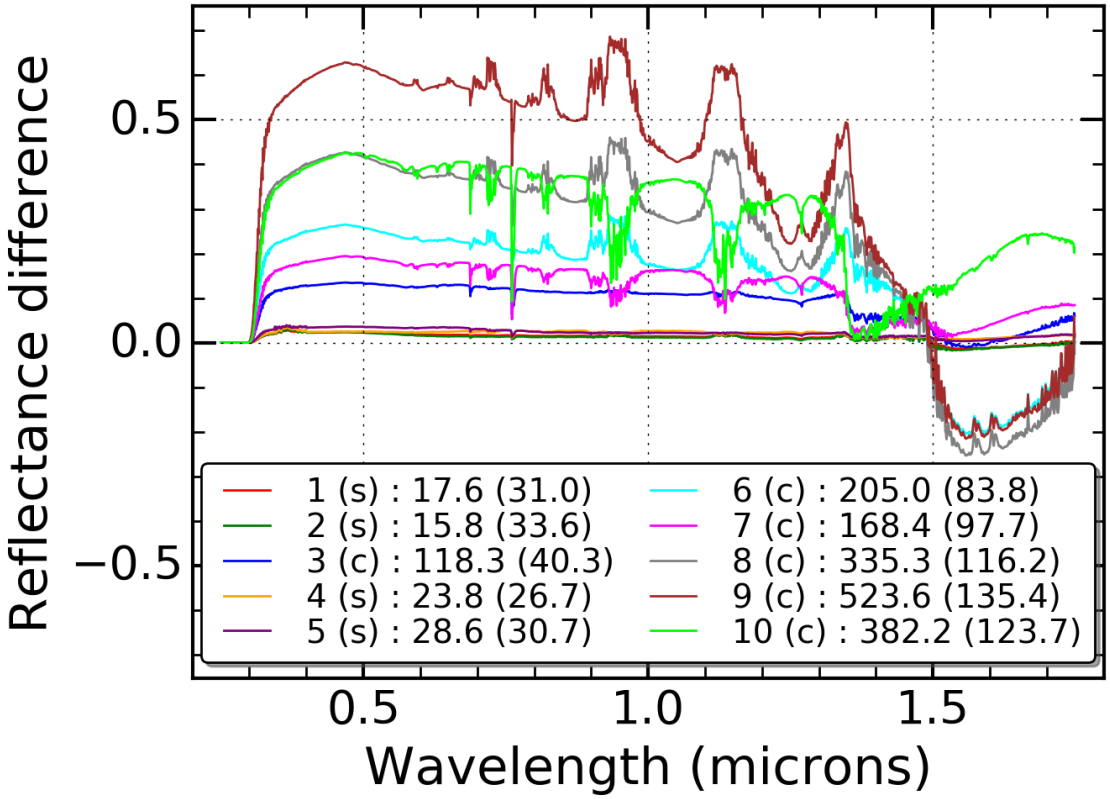

Figure 4.7. The mean spectral short-wave cloud radiative effect (SWCRE) for computed SCIAMACHY-like reflectance spectra belonging to each of the 10 clusters presented in Fig. 4.2. In the legend, each label is separated by a colon. To the left of the colon is the cluster number and its designation as either surface (s) or cloud (c). To the right of the colon is the mean spectrally integrated SWCRE, and its standard deviation in brackets, both in W m^{-2}. Positive SWCRE represents an increase in reflected solar radiation when clouds are present. SCIAMACHY is the SCanning Imaging Absorption spectroMeter for Atmospheric CHartographY.

For cloud clusters, a number of key features are found. Firstly, the mean broadband SWCREs range between 110–170 W m^{-2} for clusters with relatively optically thin clouds (e.g., Clusters 3 and 7), and from 200 to over 500 W m^{-2} for clusters with relatively optically thick clouds (e.g., Clusters 6, 8, 9 and 10). It should be noted that the stated values of the broadband SWCRE strongly depend on the amount of incoming solar radiation, but the Sun-synchronous orbit of the A-Train satellites with an equator crossing of around 13:30 local time provides some consistency over the West Africa region considered. Secondly, and perhaps most pertinent for the spectral SWCRE, is the large swing from positive to negative SWCRE for clusters associated with ice cloud (Clusters 6, 8 and 9). The presence of large positive and negative SWCRE for these

three clusters demonstrates the value of monitoring SWCRE spectrally; in the spectrally integrated values that could be obtained from an equivalent broadband measurement, the large differences in SWCRE from different parts of the spectrum partly compensate. This can make the SWCRE from two distinctly different cloud regimes appear quite similar (e.g., the mean spectrally integrated SWCRE for Clusters 6 and 7 are within 40 W m^{-2}). By utilising the spectral dimension, the signature of SWCRE becomes much larger, and therefore easier to detect. Finally, the SWCRE in water vapour absorption bands have reversed directions (i.e., bump versus dip) among clusters. When ice clouds at high altitudes are present (Clusters 6, 8 and 9), solar radiation is reflected back to space by the ice clouds before it ever gets the chance to interact with the large water vapour concentrations in the lower troposphere. As a result, the difference in water vapour absorption between computations with and without cloud is large, leading to a bump in the spectral SWCRE. Conversely, for lower level clouds that have significant water vapour above, radiation can still experience substantial water vapour absorption in the presence of clouds, reducing the SWCRE and causing a dip. Therefore, the reversal in direction of the SWCRE in water vapour absorption bands for the different clusters is typically related to the vertical positioning of the cloud, rather than variability in water vapour itself.

The mean cloud vertical structures and their spectral SWCRE, as presented in Fig. 4.5 and 4.7, represent an alternative approach to monitoring SWCRE by cloud structure. Other recent studies have calculated SWCRE for cloud structures that are pre-separated using their boundaries [*Oreopoulos et al.*, 2017; *Hill et al.*, 2018]. Specifically, these studies use the classification scheme described by *Tselioudis et al.* [2013] that allows for any combination of low 'L', mid 'M', or high 'H' level cloud separated at the pressure boundaries of 680 and 440 hPa. Cloud can either exist in each layer in isolation or extend across the pressure levels (denoted by an 'x' between letters), leading to 12 possible cloud types (henceforth "TRZK cloud types"; see Fig. 3 in *Hill et al.* [2018]), plus clear-sky. Using TRZK cloud types, these studies revealed the importance of various cloud vertical structures for the SWCRE, but the cloud boundaries are somewhat arbitrary and the optical thickness of the clouds is not considered. Another widely used cloud classification scheme that uses cloud optical thickness and cloud top height to define cloud types is the International Satellite Cloud Climatology Project (ISCCP) system [*Rossow and Schiffer*, 1999]. However, ISCCP

cloud types still require thresholds to be defined for the cloud top height boundaries, and it has been shown that the ISCCP cloud types do not always conform to these boundaries [*Mace and Wrenn*, 2013]. Instead, our approach objectively identifies cloud regimes using their spectral radiative signature alone. These cloud regimes may not be as aesthetically pleasing as those separated by vertical structure but, since no prior assumptions are required, we argue this is a more robust way to define cloud types for SWCRE investigations.

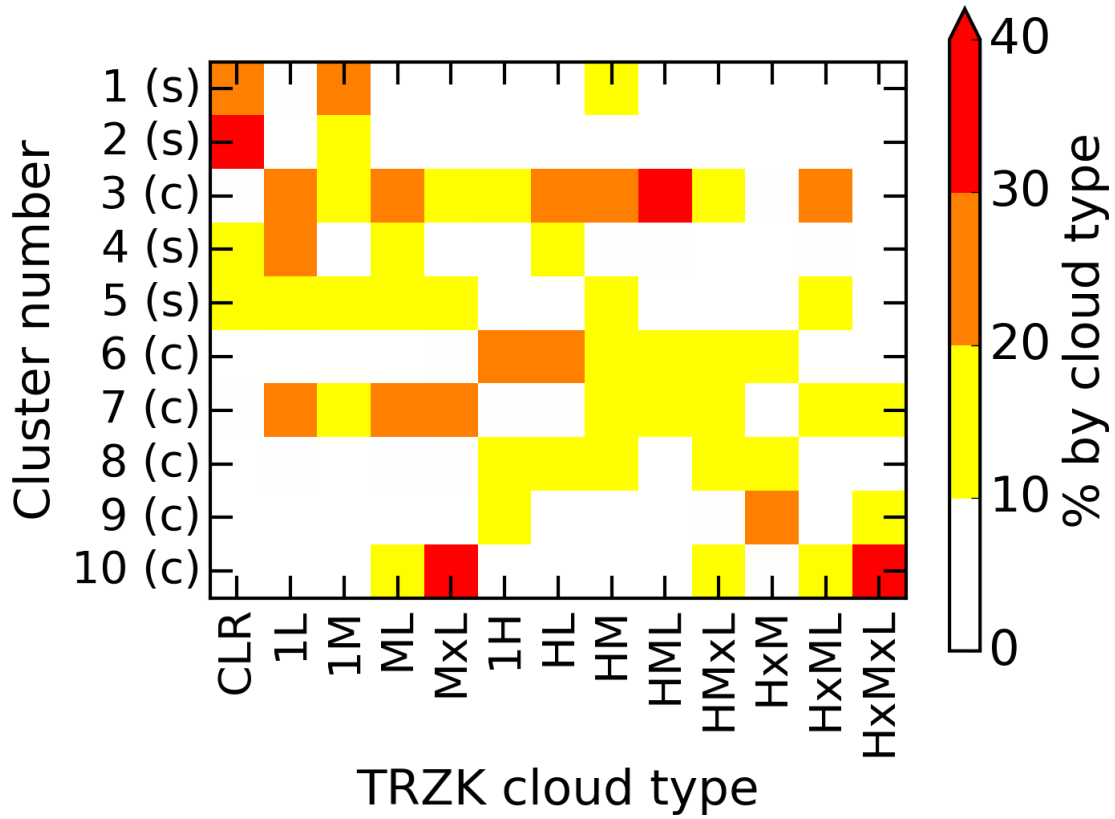

Figure 4.8. The distribution of cloud type, as defined in *Tselioudis et al.* [2013] ("TRZK cloud type"), and clear-sky 'CLR' amongst each of the 10 clusters presented in Fig. 4.2. Each cloud type is considered in isolation, such that each column adds up to 100 %. The TRZK cloud type classification allows for any combination of low 'L', mid 'M', or high 'H' level cloud separated at the pressure boundaries of 680 and 440 hPa. An 'x' between letters denotes that the cloud extends across the pressure levels. The cluster designation as either surface (s) or cloud (c) is given next to the cluster number.

The spatial domain considered in the study by *Hill et al.* [2018] falls entirely within the West Africa domain considered here, so we conclude this section by comparing the 12

TRZK cloud types and their SWCRE (Fig. 5a in *Hill et al.* [2018]), with our clusters. Firstly, the range in mean spectrally integrated SWCRE for our cloud clusters is larger (~400 W m^{-2}) than for the TRZK cloud types (~330 W m^{-2}) even though we have half the number of categories (i.e., 6 cloud clusters verses 12 TRZK cloud types). We expect this is predominantly because clouds with different optical thickness will typically lead to a different magnitude of top-of-atmosphere reflectance, which is an important factor separating our cluster centroids. In contrast, clouds with very different optical thicknesses can belong to the same TRZK cloud type as long as the geometric cloud boundaries are similar, which will bring the magnitude of the mean SWCRE for each TRZK cloud type closer together. Secondly, when each CCCM group is assigned to a TRZK cloud type using the cloud boundaries in the CCCM group, we find that many of the TRZK cloud types are widely spread amongst our clusters (Fig. 4.8). Types 1M, ML, HM and HMxL are distributed with at least 10 % of their frequency amongst five or more clusters. Only three TRZK cloud types (MxL, HML and HxMxL) have a frequency of more than 30 % in any individual cluster. Surprisingly, the HxMxL type, often associated with deep convection, most commonly falls into Cluster 10 that has virtually no ice cloud on average (Fig. 4.5j). Clear-sky only has distributions above 10 % for the surface clusters, as expected. Finally, we note that our Cluster 9 has a larger spectrally integrated mean SWCRE (523.6 W m^{-2}) than any of the TRZK cloud types as calculated by *Hill et al.* [2018]. This is despite the lower amounts of incoming solar radiation on average for our study; the region in *Hill et al.* [2018] only extends to 10 °N, compared with 30 °N here, and they only consider the summer months of June-September, compared with the entire annual cycle here. This serves as further evidence that the cloud regimes identified from spectral radiative signature alone exhibit an improved variety of SWCRE.

4.3.2 Variations with spatial scale

The distinct underlying surface and cloud properties associated with clusters of computed SCIAMACHY-like reflectance spectra present an exciting opportunity to map between spectral observations and physical phenomena. However, the results presented in Sect. 4.3.1 are based on one-dimensional, and therefore horizontally homogeneous, radiative transfer. Before proceeding with assigning real observations to clusters derived from computations, it remains to determine the sensitivity of the cluster analysis results to variations in the spatial scale of the computed spectra. This

sensitivity analysis is performed at two relevant spatial scales: the CERES footprint of around 20 km that the CCCM data are stored at, and the SCIAMACHY footprint of around 240 km for which real spectral reflectance observations are available. In addition, these spatial scales are likely to be more relevant to the modelling community because 20 km is of similar order-of-magnitude to the resolution of current numerical weather prediction models, and 240 km is of similar order-of-magnitude to the resolution of current climate models. Rather than analyse individual clusters in detail again, as was done in Sect. 4.3.1, the aim of this section is to determine whether the cluster centroids from spectra averaged over larger spatial scales change substantially and if they are still associated with distinct physical properties.

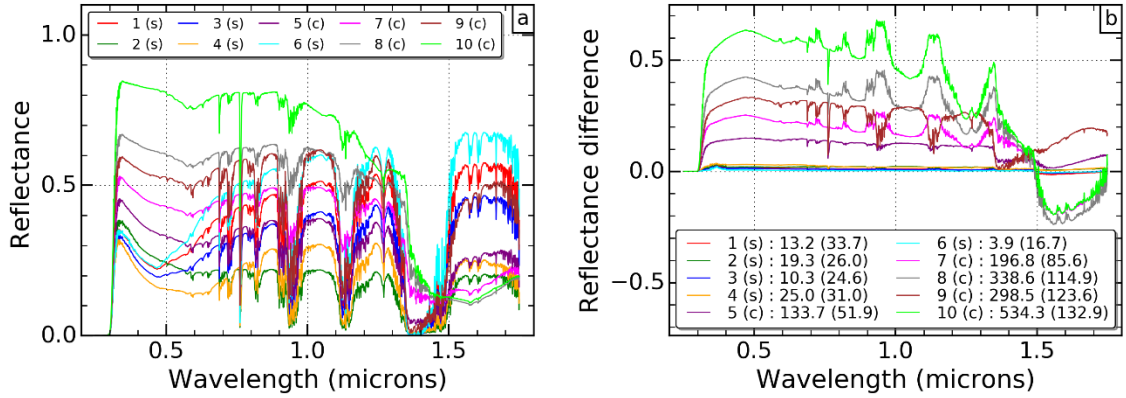

Figure 4.9. (a) Cluster centroids of top-of-atmosphere reflectance spectra and (b) their mean spectral short-wave cloud radiative effect (SWCRE). These plots are similar to Fig. 4.2 and 4.7, respectively, but instead are based on 39,375 computed SCIAMACHY-like reflectance spectra that have been averaged over a CERES footprint size of around 20 km. The clusters are numbered in the legends of (a) and (b) according to their population, from most to least populated, and are designated as either surface (s) or cloud (c). Additionally, to the right of the colon in the legend of (b) is the mean spectrally integrated SWCRE for each cluster, along with the standard deviation in brackets, both in W m^{-2}. SCIAMACHY is the SCanning Imaging Absorption spectroMeter for Atmospheric CHartographY, and CERES is the Clouds and the Earth's Radiant Energy System.

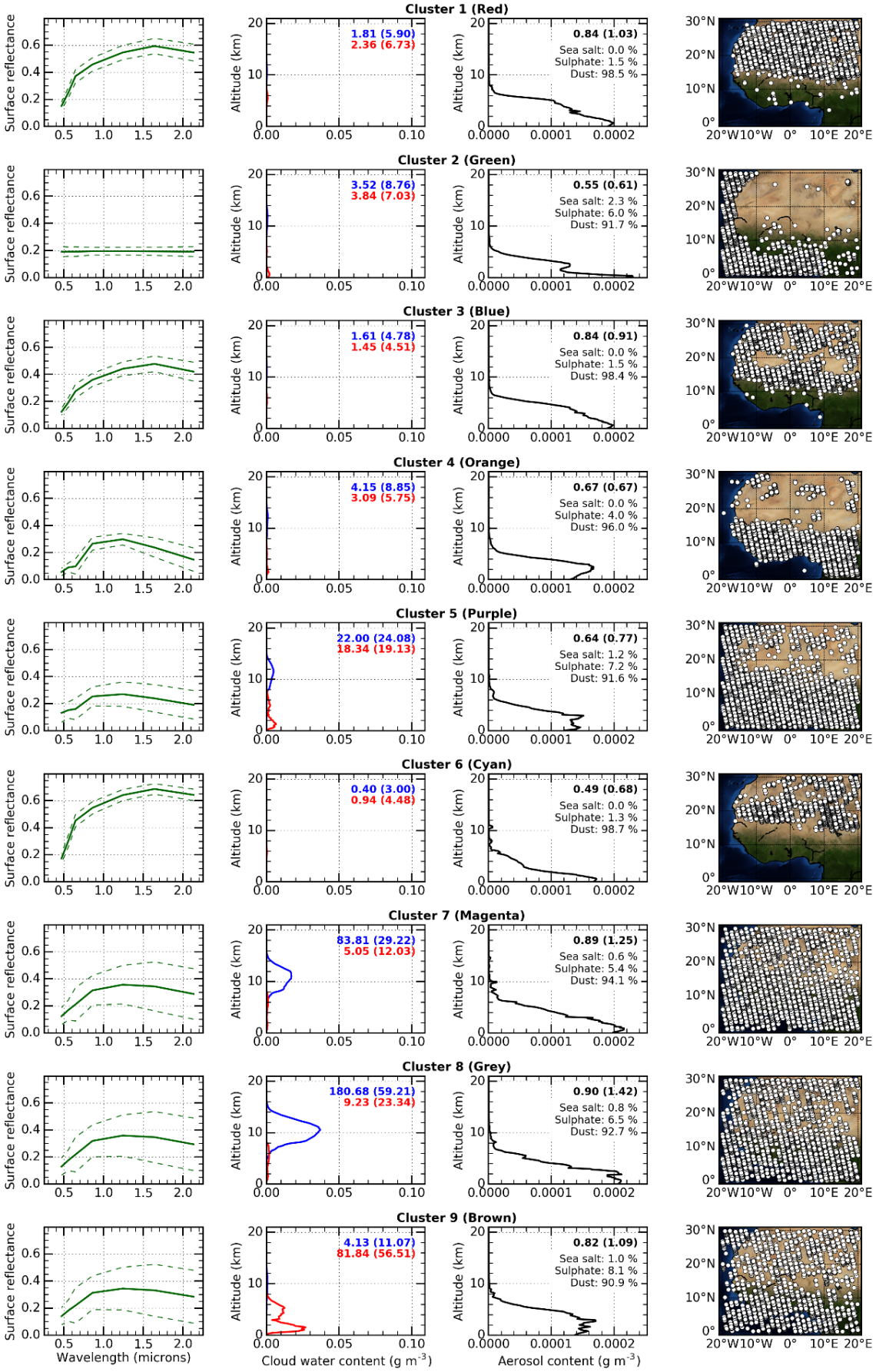

[Figure continues on next page]

[Figure continues from previous page]

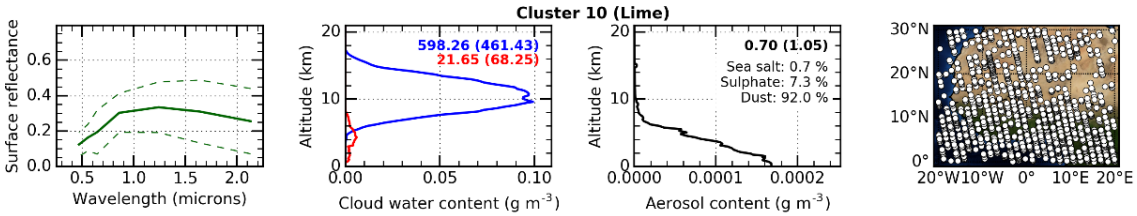

Figure 4.10. The mean scene properties used in computed SCIAMACHY-like reflectance spectra that have been averaged over a CERES footprint size of around 20 km and belong to each of the 10 clusters presented in Fig. 4.9a. The first column shows the mean spectral surface reflectance (similar to Fig. 4.3), second column the mean vertical profile of cloud water content (similar to Fig. 4.5), third column the mean vertical profile of aerosol content (similar to Fig. 4.6) and fourth column the location of the spectra (similar to Fig. 4.4). The corresponding cluster number and assigned colour is given above each row of plots. SCIAMACHY is the SCanning Imaging Absorption spectroMeter for Atmospheric CHartographY, and CERES is the Clouds and the Earth's Radiant Energy System.

The results of cluster analysis applied to computed SCIAMACHY-like reflectance spectra averaged over the CERES footprint of around 20 km are shown in Fig. 4.9 and 4.10. The number of spectra used in the cluster analysis is more than halved, from 90,917 to 39,375. This is a result of many CERES footprints consisting of single CCCM groups (most commonly clear-sky), and fewer footprints with many CCCM groups representing a high diversity of cloud structures. The cluster centroids (Fig. 4.9a) and mean spectral SWCREs (Fig. 4.9b) are broadly similar to those from Sect. 4.3.1. For example, cluster centroids representing ice and liquid cloud absorption features between 1.3 and 1.7 μm are present and various broadband magnitudes of cluster centroids exist. Likewise, the spectral SWCREs exhibit similar shapes and the spectrally integrated SWCREs are of a similar range of magnitudes.

Most notably, however, one of the cloud clusters has switched to a surface cluster, as evidenced by the five clusters in Fig. 4.9b with substantial SWCRE. Examining the controlling properties of the clusters at 20 km spatial scale (Fig. 4.10), we find that the cloud clusters that were associated with vertically distributed cloud (original Clusters 3 and 7) appear to have combined, and the surface cluster associated with bright desert (original Cluster 2) has split. This could be because clusters that were associated with

vertically distributed clouds contained contributions from a high diversity of cloud structures (Fig. 4.8) and, by averaging over 20 km, this high diversity is suppressed. As can be expected, changes in relative cluster populations has changed the order that clusters appear, resulting in surface clusters becoming Clusters 1–4 and 6, and cloud clusters becoming Clusters 5 and 7–10. Despite these differences, it is still generally the case that the spectral signatures are associated with consistent and distinct physical properties when averaged over 20 km (CERES footprint) scales.

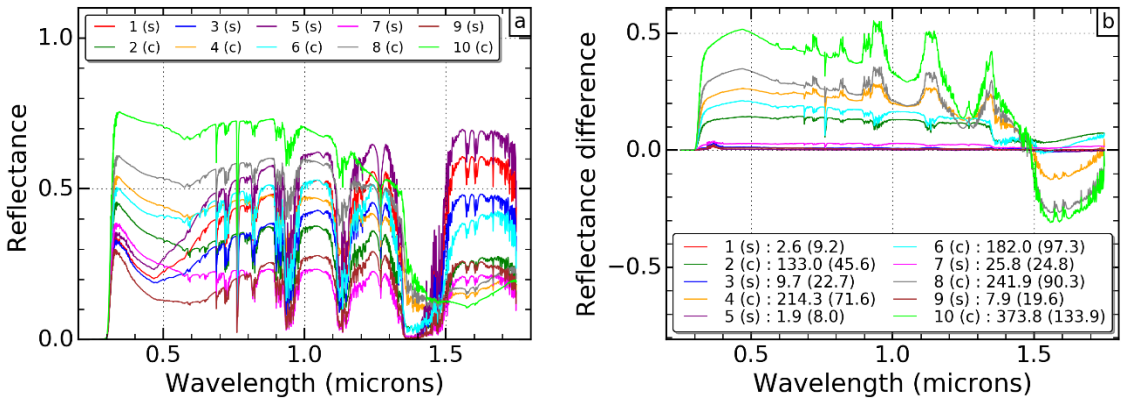

Figure 4.11. (a) Cluster centroids of top-of-atmosphere reflectance spectra and (b) their mean spectral short-wave cloud radiative effect (SWCRE). These plots are similar to Fig. 4.2 and 4.7, respectively, but instead are based on 534 computed SCIAMACHY-like reflectance spectra that have been averaged over a SCIAMACHY footprint size of around 240 km. The clusters are numbered in the legends of (a) and (b) according to their population, from most to least populated, and are designated as either surface (s) or cloud (c); further details are provided in Table 4.2. Additionally, to the right of the colon in the legend of (b) is the mean spectrally integrated SWCRE for each cluster, along with the standard deviation in brackets, both in W m^{-2}. SCIAMACHY is the SCanning Imaging Absorption spectroMeter for Atmospheric CHartographY.

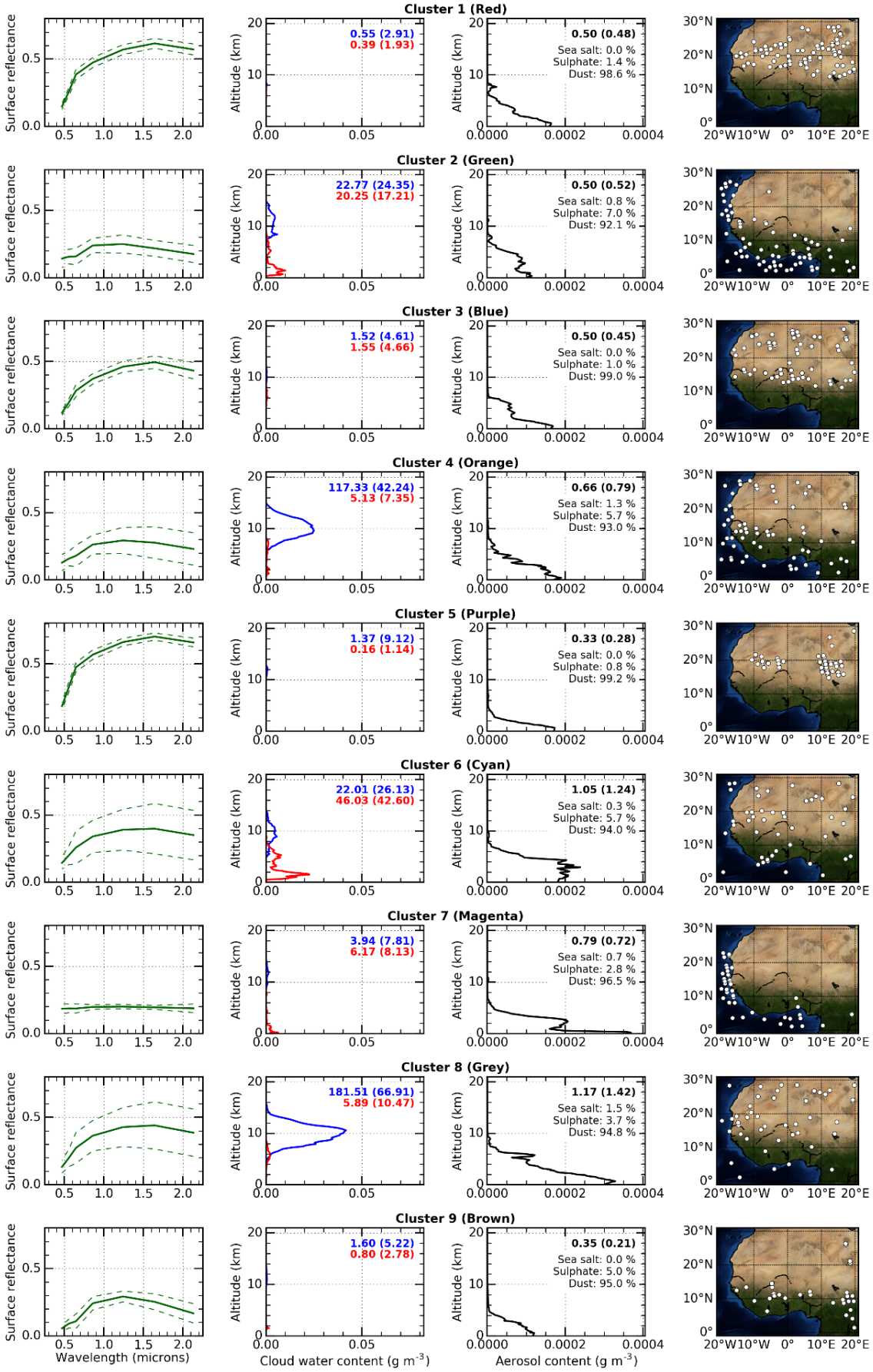

[Figure continues on next page]

[Figure continues from previous page]

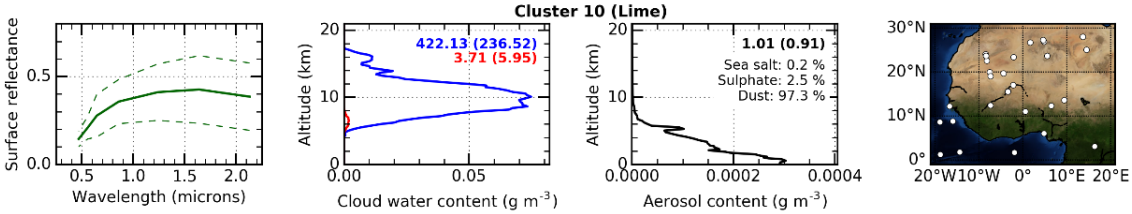

Figure 4.12. The mean scene properties used in computed SCIAMACHY-like reflectance spectra that have been averaged over a SCIAMACHY footprint size of around 240 km and belong to each of the 10 clusters presented in Fig. 4.11a. The first column shows the mean spectral surface reflectance (similar to Fig. 4.3), second column the mean vertical profile of cloud water content (similar to Fig. 4.5), third column the mean vertical profile of aerosol content (similar to Fig. 4.6) and fourth column the location of the computed spectra (similar to Fig. 4.4). The corresponding cluster number and assigned colour is given above each row of plots. SCIAMACHY is the SCanning Imaging Absorption spectroMeter for Atmospheric CHartographY.

The results of cluster analysis applied to computed SCIAMACHY-like reflectance spectra averaged over the SCIAMACHY footprint size of around 240 km are shown in Fig. 4.11 and 4.12. As expected from the coarse resolution and the need for consecutive CERES footprints (see Sect. 4.2.2.2), the sample size is reduced dramatically from the original 90,917 spectra down to 534. However, by searching for the same number of clusters, we found spectral signatures at the 240 km resolution exhibit remarkably similar features to those based on 1 and 20 km resolutions. As was the case for the 20 km resolution, the cluster centroids at the 240 km resolution (Fig. 4.11a) still represent ice and liquid cloud absorption features between 1.3 and 1.7 μm and various broadband reflectance magnitudes amongst clusters. The shape of the spectral SWCREs are also similar to those at 1 and 20 km (Fig. 4.11b), but note this time that the magnitudes of reflectance difference are not as large. This is supported by the spectrally integrated SWCRE values for each cluster that reach a maximum of 373.8 W m^{-2}, compared with over 500 W m^{-2} at both 1 km and 20 km scales. A reduction in the maximum magnitude of the SWCRE is not surprising, since the very optically thick clouds controlling these signatures are unlikely to persist over 240 km, while the fact that relatively large SWCRE is still revealed by clustering is promising.

The split of five surface and five cloud clusters is maintained from 20 km to 240 km, but when examining the controlling properties (Fig. 4.12) we do find some further subtle changes. At the 240 km scale, it appears that the cloud clusters that were associated with liquid cloud (original Cluster 10) and vertically distributed cloud mostly consisting of liquid water (original Cluster 7) combine. This gives way for the splitting of the cluster that was associated with bright desert (original Cluster 2), as was the case at the 20 km spatial scale. Again, as expected, changes in relative cluster populations have changed the order that clusters appear, coincidently resulting in all surface clusters becoming odd numbers, and all cloud clusters becoming even numbers. It is worth emphasising at this stage that, despite some subtle differences, the cluster signatures and controlling properties are remarkably similar between 240 km and 1 km resolutions. This demonstrates that, over an undoubtedly mixed scene, spectral signatures from individual dominating properties within that scene can still be detected, which is very encouraging for observational studies. These signatures and properties at the 240 km scale are used again in the next section so are summarised in Table 4.2 for convenience.

Table 4.2. Summary of the 10 clusters presented in Fig. 4.11a and their dominating properties. Based on 534 computed SCIAMACHY-like reflectance spectra over West Africa in 2010 that have been averaged over a SCIAMACHY footprint size of around 240 km.

Cluster number	Number of spectra	Assigned colour	Comment on controlling property	Designated as surface or cloud dominated?
1	87	Red	Desert	Surface
2	73	Green	Vertically distributed but optically thin cloud over dark surface	Cloud
3	64	Blue	Desert boundary	Surface
4	63	Orange	Ice cloud	Cloud
5	55	Purple	Bright desert (sand dunes)	Surface
6	46	Cyan	Vertically distributed but optically thin cloud, mostly liquid	Cloud
7	44	Magenta	Ocean	Surface
8	44	Grey	Optically thick ice cloud	Cloud
9	30	Brown	Vegetation	Surface
10	28	Lime	Very optically thick ice cloud	Cloud

4.3.3 Tracking variability in SCIAMACHY observations

To assess the extent to which spectral clustering can be used to monitor changes in atmospheric and surface properties from real spectral reflectance observations, SCIAMACHY observations are next assigned to the clusters obtained from computed SCIAMACHY-like reflectance spectra at the SCIAMACHY footprint scale (Fig. 4.11 and 4.12; Table 4.2), and the relative frequency of occurrence of the clusters is examined over time. To clarify, all cluster numbers referred to from this point forward correspond to those at the 240 km spatial scale described in Table 4.2. We choose two time periods over which to examine cluster relative frequency of occurrence: the annual cycle during 2010, and the West African monsoon seasons of 2003 and 2004. The annual cycle is chosen because the progression of the West African monsoon over the region considered here is associated with large seasonal changes in precipitation (Fig. 4.13a), and 2010 was an active monsoon year (Fig. 4.14a). Likewise, the West African monsoon seasons of 2003 and 2004 are chosen because these consecutive years exhibited the largest swing in Sahel precipitation, excluding 2010 (Fig. 4.14a). Consecutive years are used to avoid issues with instrument drift, and excluding 2010 enables us to test whether the method of assigning observations to clusters leads to useful results outside of the time period that the cluster analysis was performed. Since the precipitation changes over these various time periods only provide an indication of atmospheric activity, this section aims to identify whether these precipitation changes are strongly linked to changes in the surface and cloud regimes defined by reflectance spectra.

The annual cycle of rainfall over West Africa tends to be concentrated in two regions and occur in two different time periods (Fig. 4.13a). Firstly, intense convection and high rainfall amounts around the Gulf of Guinea (focused just below 5° N) occur in May–June, driven by sea surface temperature seasonality in the tropical eastern Atlantic. Secondly, an intense rain belt develops over the interior of the West African continent (focused just above 10° N) persisting from July–September, primarily associated with the inter-tropical convergence zone [*Gu and Adler*, 2004]. These two rainfall peaks are embedded within the larger West African monsoon circulation that is generally considered to be active from June–October [*Cornforth*, 2012]. The relative frequency of occurrence of both cloud and surface clusters, based on SCIAMACHY observations over West Africa in 2010, does not appear to represent the two rainfall

peaks suggesting that the cloud cover does not change as drastically as the precipitation between the two time periods, but it does follow the overall West African monsoon seasonality closely (Fig. 4.13b). On average, cloud clusters have higher relative frequency of occurrence from June–October than any other months during the year. Consequently, the relative frequency of occurrence averaged for surface clusters is lower from June–October than any other months during the year.

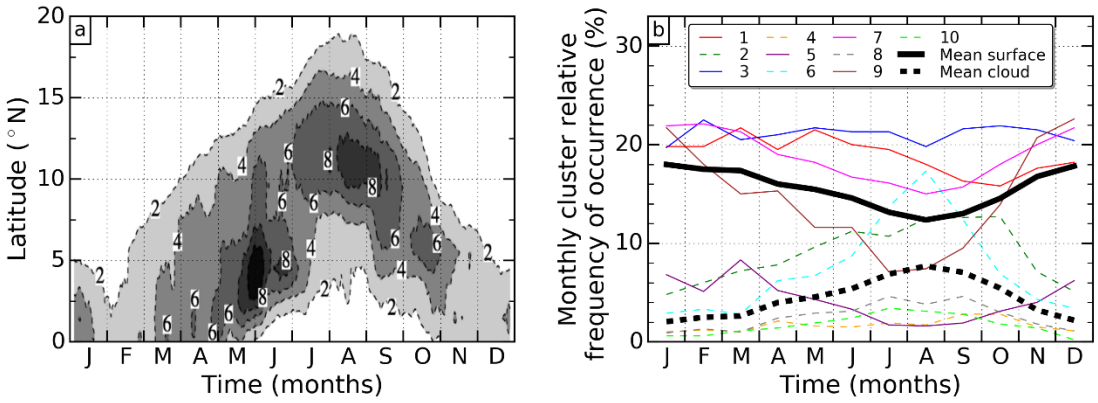

Figure 4.13. (a) The annual cycle of West African monsoon rainfall in mm day^{-1}, presented as a 10-day running mean (adapted from *Gu and Adler* [2004]). Data are from the Tropical Rainfall Measuring Mission 3B42 product 1998–2003, averaged between 9.5° W and 9.5° E. (b) Monthly cluster relative frequency of occurrence for the annual cycle of SCIAMACHY spectral reflectance observations over West Africa in 2010. The clusters used are described in Table 4.2 and are numbered in the legend, with surface clusters indicated by solid lines, and cloud clusters by dash lines. The mean of the surface and cloud clusters is represented by thick black lines. SCIAMACHY is the SCanning Imaging Absorption spectroMeter for Atmospheric CHartographY.

Examining individual cloud clusters, we find that they all exhibit West African monsoon seasonality to some extent. However, the change in the average of the cloud clusters is primarily driven by Clusters 2 and 6 that are both associated with vertically distributed cloud. These two clusters have an annual range in relative frequency of occurrence of 7.9 and 14.5 %, respectively. As previously discussed, clusters associated with vertically distributed cloud contain diverse vertical structures, which is typical of the West African monsoon [*Stein et al.*, 2011]. Of the clusters associated with ice cloud (Clusters 4, 8 and 10) the largest annual ranges are from Clusters 8 and 10 that are

associated with the optically thickest ice cloud, also consistent with the key role of convective storms during the monsoon [*Marsham et al.*, 2013].

For the surface clusters, the decrease in relative frequency of occurrence during the monsoon season is primarily driven by Cluster 9, which has an annual range of 15.5 % and is associated with vegetated surface signature. Rather than variations in the surface properties themselves, we expect this large annual range is mostly associated with location. The reason is that densely vegetated areas are almost entirely located from 0–15° N in the West Africa region, and this is precisely where the monsoon rains progress (Fig. 4.13a). In other words, the spectra over these surfaces become controlled by cloud signatures during the monsoon season, reducing the frequency of vegetation dominated spectra. A similar argument can be made for Cluster 7 that is associated with ocean surface signature, since most of the ocean area is in the southern part of the domain. The annual ranges in relative frequency of occurrence are generally lower for clusters associated with desert surface signature (Clusters 1, 3 and 5) since desert surface is, conversely, mostly located in the northern part of the domain where the West African monsoon is of lesser relevance. Note that despite the pronounced annual cycles of individual clusters, surface clusters remain most frequent on average year-round.

While the West African monsoon season was relatively active during 2003, as indicated by anomalously high Sahel precipitation, it was relatively inactive in 2004, as indicated by anomalously low Sahel precipitation (Fig. 4.14a). The difference in cluster relative frequency of occurrence between 2003 and 2004, based on SCIAMACHY observations over West Africa from June–October, appears to capture this inter-annual variability well (Fig. 4.14b). Every individual cloud cluster has a higher relative frequency of occurrence in 2003, and every individual surface cluster has a higher relative frequency of occurrence in 2004.

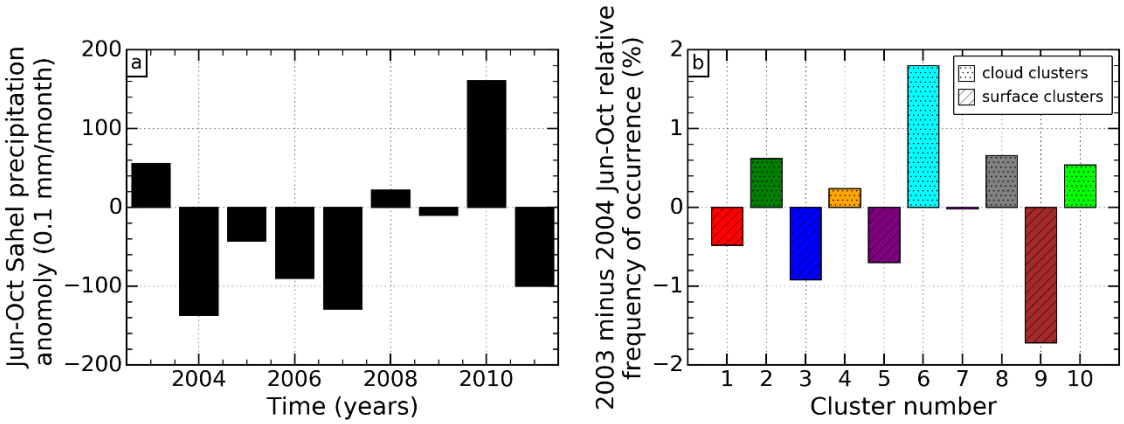

Figure 4.14. (a) Sahel precipitation anomalies for the years coinciding with SCIAMACHY observations in June–October (derived from *Mitchell* [2013]). Anomaly is relative to 1900–2013, for the region bounded by 20° W to 10° E and 10° to 20° N. Data are gridded rain gauge anomalies from the National Oceanic and Atmospheric Administration National Climatic Data Center. (b) Difference in cluster relative frequency of occurrence between 2003 and 2004 for SCIAMACHY spectral reflectance observations in June–October over West Africa. The clusters used are described in Table 4.2, with surface clusters represented by hatching with diagonal lines and cloud clusters by hatching with dots. SCIAMACHY is the SCanning Imaging Absorption spectroMeter for Atmospheric CHartographY.

Examining individual clusters, we find that the largest change in relative frequency of occurrence is represented by the same clusters that were most important in the annual cycle for 2010. Cluster 6, associated with vertically distributed cloud, has a relative frequency of occurrence that is 1.8 % larger in 2003 than 2004, while other cloud clusters have smaller magnitude changes but consistent sign. Cluster 9, associated with vegetated surface signature, has a relative frequency of occurrence that is 1.7 % smaller in 2003 than 2004, while other surface clusters also have smaller magnitude changes but consistent sign. This consistency in cluster relative frequency of occurrence between 2003 and 2004 and throughout 2010 provides evidence that the detected inter-annual variability is associated with West African monsoon variability, and that assigning observations to clusters can work successfully if applied outside of the time period over which the clustering is performed.

4.4 Summary

The spectrum of solar radiation emerging at the top of the atmosphere is rich with Earth system information. This spectral information can become masked in traditional broadband satellite measurements, limiting the signal available to detect and monitor the properties controlling variability in the reflected solar radiation and therefore the global energy budget. To identify distinct spectral signatures and directly relate them to the underlying physical properties controlling their structure, over 90,000 solar reflectance spectra are computed over West Africa in 2010. The computations are performed with a fast radiative transfer code using atmospheric and surface properties derived from a diverse combination of Afternoon-Train satellite observations, and the spectral characteristics of the SCanning Imaging Absorption spectroMeter for Atmospheric CHartographY (SCIAMACHY) instrument. Cluster analysis applied to the computed spectra reveals spectral signatures related to distinct surface properties such as vegetation, ocean and desert, and distinct cloud regimes determined by their spectral short-wave cloud radiative effect (SWCRE). The mean spectrally integrated SWCREs range from close to zero for the surface clusters, up to more that 500 W m^{-2} for cloud clusters. This method of identifying cloud regimes and their SWCREs offers an alternative way to define cloud type for SWCRE applications, and does not require any prior assumptions. The direct link between physical properties and distinct spectral signatures extracted from clustering presents an excellent opportunity to understand the underlying properties controlling real spectral reflectance observations. By assigning SCIAMACHY observations over West Africa to the calculated spectral clusters, the relative frequency of occurrence of the clusters is monitored over time. During the annual cycle of 2010 the cloud clusters are most populated during the active West African monsoon season of June–October, with one cluster related to vertically distributed cloud increasing its relative frequency of occurrence by 14.5 %. Likewise, all cloud clusters have a higher relative frequency of occurrence during the relatively active monsoon season of 2003, compared with the relatively inactive monsoon season of 2004. Overall, the distinct underlying physical properties controlling spectral signatures, as extracted by clustering of reflectance spectra from radiative transfer computations, show great promise for monitoring evolution of the Earth system directly from solar spectral reflectance observations.

5 CHAPTER FIVE: Summary, conclusions and future work

5.1 Summary and conclusions

The flux of radiation exiting at the top of the atmosphere, referred to in this thesis as Earth outgoing radiation (EOR), constitutes a vital component of the Earth's energy budget. Since EOR is inherently connected to the rapidly evolving scene from which the radiation originates and exhibits large regional variations, it is of paramount importance that we can monitor EOR at a sufficient frequency and spatial scale for weather and climate studies. Achieving these criteria remains challenging using traditional satellite measurement techniques; either a low number of expensive instruments in low-earth orbit that lack frequent sampling or instruments in geostationary orbit that do not permit global coverage. However, explosive development in small satellite technology and sensor miniaturisation has paved a potentially viable route for measurements to be made from a constellation of identical satellites in different orbits. This offers an exciting new opportunity to make observations of EOR with global coverage, high temporal resolution, and possibly with high spectral resolution for the first time. Despite the potential of the constellation approach for EOR observations, a thorough assessment of its capabilities and the scientific advances that it could enable have not previously been fully explored.

To address this issue directly, the primary objective of this thesis was to determine the extent to which a constellation of small satellites could enhance global EOR observations and explore the associated science that could be provided. To achieve this objective, three science questions were put forward:

- *Science question 1. Can a feasible constellation of satellites enhance observations of Earth's outgoing energy flows?*
- *Science question 2. What controls the diurnal cycle of global outgoing radiation?*
- *Science question 3. How can spectrally resolved outgoing short-wave radiation be used to fingerprint the Earth system?*

These questions were addressed in Chapters 2, 3 and 4, respectively. The key conclusions and answers to each of these questions, based on the results presented in this thesis, are summarised in the remainder of this section.

Science question 1. Can a feasible constellation of satellites enhance observations of Earth's outgoing energy flows?

The capability of a new constellation concept to determine global EOR with sufficient temporal resolution and accuracy for weather and climate studies has been investigated. Specifically, criteria of global hourly coverage at a 1000 km spatial scale and a global mean accuracy better than 0.6 W m^{-2} were set. These criteria would allow for tracking of fast-evolving synoptic phenomena and their diurnal variability at an accuracy sufficient to resolve the sign of the estimated long term energy imbalance at the top-of-atmosphere, possibly making EOR observations suitable for assimilation into numerical weather prediction and for weather forecast verification. Capitalising on technology revolutions in small satellites and sensor miniaturisation, the proposed baseline constellation to achieve these criteria comprises 36 identical wide-field-of-view (WFOV) radiometers, evenly distributed in six non-Sun-synchronous orbit planes. The WFOV feature is desirable to provide global coverage over a short time scale while minimising the data downlink volume. To investigate the errors associated with the baseline constellation, and the error growth with spatial resolution and time scale, a recovery method was developed and extensive simulation experiments were performed.

The baseline constellation provided sufficient 5 s instantaneous WFOV measurements for a stable recovery of hourly outgoing irradiance fields at both planetary and synoptic scales. At a spatial resolution of 1000 km, assuming isotropic radiation and perfect calibrations, the mean hourly global errors averaged for 1 day are 0.16 ± 0.45 W m^{-2} and -0.13 ± 0.15 W m^{-2} for short-wave and long-wave irradiance, respectively. These results are very much improved when compared with current observational products but are based on simplified radiance fields and idealised instrument characteristics. To identify the influence of these simplifications and changes in the constellation setup, a series of sensitivity tests were performed.

Firstly, the influence of the anisotropic nature of the radiance field was investigated by generating a new set of simulated measurements using angular distribution models that take into account the directional effects of the solar-viewing geometry, the surface type, and the meteorology of the scene. The global mean outgoing short-wave irradiance could be recovered to within 0.56 W m^{-2} of that in the control experiment by randomly accounting for the meteorological influences on the angular distribution. This method

significantly increases regional errors, but low regional errors can be obtained by assuming that the radiation is isotropic during the recovery process, which kept the root-mean-square error to within 6 % of the control experiment. It is also possible to reduce the error by incorporating angular distribution models directly into the core of the recovery method, but in that case, ancillary observations will be needed to help classify the scene and determine its associated angular distribution model.

Secondly, the impact of a systematic calibration error of 0.5 W m^{-2} was tested, with and without random instrument noise up to 0.5 W m^{-2}. A systematic calibration error of 0.5 W m^{-2} was found to have the largest individual impact of 0.63 W m^{-2} on the recovered short-wave and long-wave irradiance, while random instrument noises tend to have a negligible impact. Overall, the recovery errors in hourly global means due to compounding sources of uncertainty grow linearly, and thus, one can adjust the total error estimate linearly if the actual calibration errors are smaller or larger than the tested value.

Thirdly, the recovery errors in hourly global mean irradiance increase with decreasing number of satellites. Since irradiance fields in the short-wave tend to be more inhomogeneous and evolve faster than that in the long-wave, the recovery errors grow faster in the short-wave when the number of satellites is reduced. When a reduction in the number of satellites is necessary in reality, the results suggest that keeping the same number of satellites per orbital plane but reducing the total number of orbit planes would be more effective to retain the observation capability in measuring global mean outgoing irradiance.

Finally, it is noted that other constellation configurations beyond those that were tested are possible, including hosted payloads on commercial satellites or a single dedicated launch with differing satellite drift to deploy the constellation. Likewise, other orbital altitudes are possible; a high orbital altitude of 780 km is deliberately assumed to maximise the satellite footprint, but small satellites are actually often deployed in lower orbits to reduce fuel use and therefore mass during deployment. Global mean irradiance fields using various configurations can be similarly obtained using the recovery method, although it is envisaged that some modification or prior constraints may be necessary to ensure a stable recovery. Nevertheless, the simulation experiments demonstrate the great potential of a new constellation concept for monitoring global

Earth energy flows in the climate system at a time scale shorter than monthly, which is challenging to achieve using existing radiation budget measurements.

Science question 2. What controls the diurnal cycle of global outgoing radiation?

One of the greatest attributes of the satellite constellation concept for EOR is the ability to capture the diurnal cycle, a fundamental forcing cycle for our weather and climate. While the potential of a viable constellation for capturing this diurnal variability has been revealed during the aforementioned simulation experiments, the underlying processes controlling this variability at the global scale remain elusive. To provide insight into what these processes might be, and their relative importance, the diurnal cycle has been assessed using global output of Earth's outgoing energy flows in September 2010 from the Met Office Unified Model. While the characteristics of the diurnal cycle will depend on the model chosen, models have the unique ability to generate spatially complete, high temporal resolution data fields for a wide variety of geophysical variables simultaneously, unrivalled by current observations. Dominant patterns of variability have been extracted from the emitted-thermal and reflected-solar components of the outgoing energy flows and the extent of coupling of these patterns with the variability in other relevant geophysical variables examined.

The two dominant patterns of diurnal variability in the emitted long-wave component are found to be consistent with solar heating of the land surface and development of convective cloud, respectively. The first pattern is highly coupled with variations in the surface temperature and the second pattern is highly coupled with variations in cloud water and height, further supporting the physical attributions. These patterns represent the first fully global estimates of the dominant patterns of diurnal variability in the emitted radiation from our planet, but are similar to those found in previous studies that used spatially limited satellite observations. The amount of variance explained by the two dominant patterns here is 68.5 and 16.0 %, respectively, totalling 84.5 %. This is markedly less than that previously found in observations over Africa, Europe and surrounding waters, with around half of the difference resulting from the different spatial regions considered. This demonstrates the importance of complete global coverage if revealing the relative importance of diurnal processes controlling the long-wave component of the global energy budget is of interest.

The two dominant patterns of diurnal variability in the reflected short-wave component, calculated in terms of albedo, are found to be consistent with a dependence on the angle of the incoming solar radiation and the development of both convective and marine stratocumulus cloud, respectively. The dependence due to the angle of the incoming solar radiation explains 88.4 % of the diurnal variance alone, and is found to be a result of contributions from changing surface and cloud albedo, as well as enhanced scattering from aerosols and atmospheric molecules. Atmospheric absorption acts to reverse the enhanced scattering at larger solar zenith angles, but is around an order of magnitude less influential than the scattering under typical clear-sky conditions. For the second pattern related to cloud development, the spatial variability is very similar to the equivalent long-wave pattern in convective regions and is also strongly coupled to the variability in cloud water and height in these regions. However, there are substantial additional sources of compensating variability in marine stratocumulus regions, demonstrating why both the long-wave and short-wave components are required together for revealing all important diurnal radiative processes. This second pattern only explains 6.7 % of the total variance, suggesting that cloud development and dissipation are relatively less important in controlling the diurnal variability of reflected short-wave radiation. The equivalent patterns from geostationary satellite observations centred over Africa are also presented, which repeat the dominance and features of the first modelled pattern and the presence of compensating convective and marine cloud variations in the second modelled pattern. The timing of the pattern related to cloud variations is slightly later in the observations, consistent with previous findings, but the presence of the patterns indicates that the physical processes dominating the diurnal variability in the modelled reflected solar radiation (RSR) are robust.

The strong coupling between radiation and cloud variability is only achieved with significant lag times between the variables. The lag times between convective patterns in emitted long-wave radiation and cloud variables paint a coherent picture. Initial development of low-altitude liquid cloud is followed later by development of ice cloud at higher altitudes, which is in turn followed by development of high-level anvil cloud. Evaporation of this anvil cloud into the surroundings moistens the upper troposphere and appears to delay the long-wave radiation response to the reduction in cloud height by several hours. For the short-wave pattern related to cloud development, the lag times with the same cloud variables are substantially shorter. The moist upper troposphere

does not continue to enhance the RSR once the convective cloud dissipates, and the additional influence of marine stratocumulus cloud pulls the pattern closer to the cloud variations. The result is that the short-wave radiation response to diurnal cloud development and dissipation is sharper and more immediate than the long-wave response, which is supported by the equivalent patterns in satellite observations.

Interpreted from a broader perspective, these results demonstrate that a multi-variable, high temporal resolution and complete coverage approach can lead to an enhanced understanding of processes in the Earth system. This highlights an important gap in the current observing system and points to a need for observing systems capable of observing everything, everywhere, all of the time. The patterns identified in this study can help refine sampling strategies to maximise diurnal information obtained from such observations. These observations could then be used to evaluate and improve the performance of the models, fully supporting the call for global, diurnal observing systems for EOR in the future.

Science question 3. How can spectrally resolved outgoing short-wave radiation be used to fingerprint the Earth system?

Exploring the temporal dimension of EOR has proved to be effective in revealing process information related to the diurnal cycle, but there is another dimension of EOR that also contains dense information and could also potentially be captured by a future satellite constellation: the spectral dimension. The spectral dimension has been intentionally overlooked thus far to maintain relevance of the results with current observing systems and ongoing technology demonstrations. However, EOR is fundamentally an intricate spectral quantity, and the spectral signature of EOR offers vast potential to improve understanding of the underlying physical properties controlling variability in EOR. While there are multiple current observing systems monitoring spectrally-resolved emitted-thermal radiation, and hence relatively many studies examining its variability, analogous work examining spectrally-resolved RSR is less well developed. To improve understanding of the spectral dimension of RSR, over 90,000 top-of-atmosphere solar reflectance spectra have been computed over West Africa in 2010 using atmospheric and surface properties derived from Afternoon-Train satellite observations. These computations are performed with a fast radiative transfer code and assume the spectral characteristics of the SCanning Imaging Absorption

spectroMeter for Atmospheric CHartographY (SCIAMACHY). By clustering the computed reflectance spectra, 10 clusters, each representing a spectral signature, are extracted and the underlying properties associated with each spectral signature are examined.

The most common extracted spectral signatures are associated with surface reflectance properties. Specifically, signatures related to vegetation, ocean and desert surfaces are found, as evidenced by the location of the spectra corresponding to each signature and their mean surface spectral reflectance. Similarly, signatures representing distinct cloud regimes are detected, each related to either liquid cloud, different optical thicknesses of ice cloud or different vertical distributions of optically thin cloud. Each of these signatures representing cloud regimes are primarily distinguished by their spectral short-wave cloud radiative effect (SWCRE) that, importantly, can exhibit positive and negative SWCRE in different spectral regions, leading to partly compensating influences in equivalent broadband measurements. The mean spectrally integrated SWCRE associated with the signatures ranges from close to zero for the surface signatures, up to more than 500 W m^{-2} for cloud signatures, which is substantially larger than the ranges presented in other recent studies that have examined the SWCRE of various cloud vertical structures. In fact, cloud vertical structures are found to be widely distributed amongst the extracted signatures. Since the cloud regimes and their SWCREs identified in this work are based on spectral radiative signature alone, this method is suggested as an improved way to define cloud types for SWCRE investigations that does not require prior assumptions.

The link between spectral signatures and underlying physical properties extracted from clustering of computed reflectance spectra presents an excellent opportunity to understand the underlying properties controlling real spectral reflectance observations. First, however, to investigate any changes in these links with variations in the spatial scale (i.e., inhomogeneity) of the observations, spectral signatures are extracted again from computations averaged over 20 km and 240 km. These scales are relevant to current energy budget missions and available spectral reflectance observations from SCIAMACHY, and also numerical weather prediction and climate modelling, respectively. The spectral signatures and their controlling properties are found to remain remarkably distinct at these spatial scales, suggesting that the dominating

properties controlling spectral variability can still emerge at these spatial scales despite an undoubtedly mixed scene, which is extremely encouraging for observational studies.

By assigning real SCIAMACHY reflectance observations over West Africa to the spectral signatures identified at the 240 km spatial scale, the relative frequency of occurrence of the signatures is monitored over time. During the annual cycle of 2010, the relative frequency of occurrence of the signatures associated with cloud reflectance are, on average, highest during the active West African monsoon season of June–October. Similarly, signatures associated with surface are, on average, lowest during this season. One signature related to vertically distributed cloud has an annual range in relative frequency of occurrence of 14.5 % that matches the seasonality of the West African monsoon. Similarly, all cloud signatures are found to have a higher relative frequency of occurrence during the relatively active monsoon season of 2003, compared with the relatively inactive monsoon season of 2004. The individual signatures with the largest changes between these years were the same signatures with the largest changes throughout 2010, providing further evidence that the change in top-of-atmosphere spectral RSR between the years was associated with variability in the West African monsoon circulation.

Overall, the distinct underlying physical properties found to control spectral signatures has revealed the value of the spectral dimension for understanding the controls on the top-of-atmosphere RSR. The utility of the extracted signatures for monitoring intra-annual and inter-annual variability associated with the West African monsoon has been demonstrated, and presents an alternative route forward for monitoring evolution of the Earth system directly from solar spectral reflectance observations, without the need for simultaneous observations from highly advanced active sensors or retrieval.

5.2 Future work

Add further realistic and specific engineering constraints to simulation experiments

The simulation experiments presented in Chapter 2 were based on somewhat simplified instrument characteristics. Although the influence of varying the instrument characteristics was assessed over a range of different possibilities, it was not clear where a realistic instrument would fit into this range. As the first results from the

Radiometer Assessment using Vertically Aligned Nanotubes (RAVAN) instrument (i.e., a real instrument that has been in orbit) are now being processed, a much better indication of the specific instrument characteristics will soon be possible. These instrument characteristics include factors such as the angular and spectral response, random noise, systematic bias and drift. It would be useful to repeat the simulation experiments by incorporating these specific characteristics determined from RAVAN, to provide a more precise estimate of what is possible from a satellite constellation in reality.

As well as the characteristics of the instrument, the characteristics of the satellite on which the instrument is hosted can also have an important influence on the simulated observations. The results presented in this thesis make no assumption about the type of satellite that the instrument flies on, but it is most likely that any future constellation would be launched on a series of small satellites, each similar to the 3U CubeSat that RAVAN was hosted on. There are, therefore, lessons to be learned from the satellite characteristics determined from the RAVAN demonstration. For example, how accurately can the satellite be pointed at nadir (i.e., attitude control), how stable is the orbit of the satellite, what is the power available on a satellite of this size, how good is the thermal control on a satellite of this size, what is the lifetime of individual satellites (that partly governs the fuel demands) and what limitations are there on the transmission of data collected from the satellite. These are all factors that can be incorporated into the simulation experiments to some extent and would, again, improve the realism of the results. In summary, future work will benefit from collaboration with engineers to better constrain the various assumptions made during the simulation experiments and lead to more targeted results.

Extend simulation experiments to spectrally resolved measurements

The value and potential of spectrally resolved observations, as demonstrated in Chapter 4, was investigated independent of constellation sampling. A natural next step would be to determine exactly how spectral information could be utilised from a specific constellation of satellites. One way to achieve this is by repeating the simulation experiments for spectrally resolved observations, rather than broadband observations as was the case in Chapter 1.

Extension of the simulation experiments to spectrally resolved observations would constitute a substantial additional body of work, and several challenges lie ahead. Firstly, only spectral RSR has been investigated in this thesis. It may, therefore, be useful to start by performing a similar analysis to that done in Chapter 4 for the spectral outgoing long-wave radiation (OLR). The spectral signatures of RSR and OLR could then be used in synergy to understand the spectral variability in the total EOR, which is likely to yield further information given that some processes influence the both regions of the spectrum, other processes are more important in the long-wave, and the OLR signatures provide the opportunity to investigate spectral variability at night. Secondly, the scientific goal of further spectral simulation experiments would be subtly different, focused around process understanding as well as monitoring the total energy budget. Thirdly, although SCIAMACHY has provided a useful guide for spectral instrument characteristics, a hyperspectral energy budget instrument specifically suited for constellation deployment has not been developed and tested, as is the case with broadband measurements and RAVAN. Any results from these further simulation experiments would therefore be more distant from application in reality. Fourthly, while spectral detector technology is evolving rapidly, reducing the need for cooling of the detectors, it remains the case that measurements without cooling can be made better at some wavebands than others. It may therefore be useful to consider some sort of blended approach with existing observations during a practical deployment. Finally, the required spectral irradiance model output would increase the already challenging demand on data storage by several orders of magnitude.

Investigate spectral signatures at the global scale with all aerosol types included

Although the spectral signatures revealed in Chapter 4 were sufficient to reveal distinct atmospheric and surface properties, they were fundamentally limited by two factors. Firstly, the satellite data used for the radiative transfer simulations was only available over the region bounded by 20° W to 20° E and 0° N to 30° N, so the results presented are only capable of capturing the spectral RSR variability of that region. Secondly, the radiative transfer simulations were not able to incorporate all of the aerosol types included in the satellite data. Importantly, there were no absorbing aerosols included in the simulations, which could be important over the region considered due to biomass burning in Southern and Central Africa.

Fortunately, it should be possible to overcome both of these limitations in the near future. The Met Office is working to extend the satellite observations to the global scale. Likewise, a further training run of the radiation code is currently underway at the Met Office that will be capable of including all aerosol types included in the satellite dataset. Future work could therefore extend the spectral signature extraction to the global scale with all relevant radiative signatures included. This would open up many more possibilities for the tracking short-wave spectral signatures that could be made from a satellite constellation, such as investigating whether the small inter-annual variability in global albedo exists in the spectral dimension, and monitoring hemispherical cloud radiative effects to provide insights into the controls of the symmetry in hemispheric albedo.

Use RSR spectral clustering to monitor cloud radiative effect

Of the spectral signatures presented in Chapter 4, the ones that were associated with cloud properties all exhibited a distinct spectral SWCRE. These distinct spectral SWCRE not only existed for signatures extracted from computed reflectance spectra at the finest spatial resolution, but also for the computed reflectance spectra averaged over a 240 km spatial scale. This suggests that SCIAMACHY observations may contain spectral information sufficient for quantifying SWCRE.

To examine the possibility of extracting SWCRE from SCIAMACHY observations, future work could consider using the extracted spectral signatures from computed reflectance spectra and their computed SWCRE to map between real SCIAMACHY observations and their SWCRE, similar to what has already been done with the relative frequency of occurrence of the signatures. However, since the SWCRE is an exact quantity, care must be taken. For example, once a given SCIAMACHY spectral reflectance observation has been assigned to a particular computed spectral signature, the standard deviation of SWCRE for individual computed spectra belonging to that extracted signature was sometimes found to be relatively large. One option is to then search the individual computed spectra belonging to that extracted signature, and find the one with the lowest root-mean-square difference to the given observation, and use the computed SWCRE of that spectrum. However, there is no guarantee that the observed and computed spectra will be similar enough, so some threshold root-mean-square difference may need to be introduced, beyond which the SWCRE is considered

to be unreliable. Sensitivity studies could be performed using computed spectra from other time periods, with known SWCRE, to evaluate the success of the approach.

6 REFERENCES

Allan, R. P., C. Liu, N. G. Loeb, M. D. Palmer, M. Roberts, D. Smith, and P.-L. Vidale. (2014). Changes in global net radiative imbalance 1985-2012. *Geophysical Research Letters*, **41(15)**, 5588–5597. https://doi.org/10.1002/2014GL060962

Allan, R. P., A. Slingo, S. F. Milton, and M. E. Brooks. (2007). Evaluation of the Met Office global forecast model using Geostationary Earth Radiation Budget (GERB) data. *Quarterly Journal of the Royal Meteorological Society*, **133(629)**, 1993–2010. https://doi.org/10.1002/qj.166

Anderberg, M. R. (1973). *Cluster analysis for applications*. New York: Academic Press.

Ansell, C., H. E. Brindley, Y. Pradhan, and R. Saunders. (2014). Mineral dust aerosol net direct radiative effect during GERBILS field campaign period derived from SEVIRI and GERB. *Journal of Geophysical Research: Atmospheres*, **119(7)**, 4070–4086. https://doi.org/10.1002/2013JD020681

Bakalian, F., H. Ritchie, K. Thompson, and W. Merryfield. (2010). Exploring Atmosphere–Ocean Coupling Using Principal Component and Redundancy Analysis. *Journal of Climate*, **23(18)**, 4926–4943. https://doi.org/10.1175/2010JCLI3388.1

Baldridge, A. M., S. J. Hook, C. I. Grove, and G. Rivera. (2009). The ASTER spectral library version 2.0. *Remote Sensing of Environment*, **113(4)**, 711–715. https://doi.org/10.1016/J.RSE.2008.11.007

Bandeen, W. R., R. A. Hanel, J. Licht, R. A. Stampfl, and W. G. Stroud. (1961). Infrared and reflected solar radiation measurements from the Tiros II meteorological satellite. *Journal of Geophysical Research*, **66(10)**, 3169–3185. https://doi.org/10.1029/JZ066i010p03169

Barker, H. W., and Z. Li. (1995). Improved Simulation of Clear-Sky Shortwave Radiative Transfer in the CCC-GCM. *Journal of Climate*, **8(9)**, 2213–2223. https://doi.org/10.1175/1520-0442(1995)008<2213:ISOCSS>2.0.CO;2

Barkstrom, B. R. (1984). The Earth Radiation Budget Experiment (ERBE). *Bulletin of the American Meteorological Society*, **65(11)**, 1170–1185.

https://doi.org/10.1175/1520-0477(1984)065<1170:TERBE>2.0.CO;2

Barnhart, D. J., T. Vladimirova, and M. N. Sweeting. (2009). Satellite Miniaturization Techniques for Space Sensor Networks. *Journal of Spacecraft and Rockets*, **46(2)**, 469–472. https://doi.org/10.2514/1.41639

Benas, N., S. Finkensieper, M. Stengel, G.-J. van Zadelhoff, T. Hanschmann, R. Hollmann, and J. F. Meirink. (2017). The MSG-SEVIRI-based cloud property data record CLAAS-2. *Earth System Science Data*, **9(2)**, 415–434. https://doi.org/10.5194/essd-9-415-2017

Bender, F. A.-M., H. Rodhe, R. J. Charlson, A. M. L. Ekman, and N. Loeb. (2006). 22 views of the global albedo—comparison between 20 GCMs and two satellites. *Tellus A: Dynamic Meteorology and Oceanography*, **58(3)**, 320–330. https://doi.org/10.1111/j.1600-0870.2006.00181.x

Betts, A. K. (2002). Evaluation of the diurnal cycle of precipitation, surface thermodynamics, and surface fluxes in the ECMWF model using LBA data. *Journal of Geophysical Research*, **107(D20)**, 8045. https://doi.org/10.1029/2001JD000427

Bingham, B., Q. Young, and S. Whitmore. (2008). Large Constellation Development using Small Satellites. In *AIAA/USU Conference on Small Satellites*. Retrieved from https://digitalcommons.usu.edu/smallsat/2008/all2008/62

Bjornsson, H., and S. A. Venegas. (1997). *A manual for EOF and SVD analyses of climatic data*. Montreal. Retrieved from http://www.geog.mcgill.ca/gec3/wp-content/uploads/2009/03/Report-no.-1997-1.pdf

Bodas-Salcedo, A., P. G. Hill, K. Furtado, K. D. Williams, P. R. Field, J. C. Manners, P. Hyder, and S. Kato. (2016). Large Contribution of Supercooled Liquid Clouds to the Solar Radiation Budget of the Southern Ocean. *Journal of Climate*, **29(11)**, 4213–4228. https://doi.org/10.1175/JCLI-D-15-0564.1

Boutle, I. A., and S. J. Abel. (2012). Microphysical controls on the stratocumulus topped boundary-layer structure during VOCALS-REx. *Atmospheric Chemistry and Physics*, **12(6)**, 2849–2863. https://doi.org/10.5194/acp-12-2849-2012

Bretherton, C. S., C. Smith, and J. M. Wallace. (1992). An Intercomparison of Methods

for Finding Coupled Patterns in Climate Data. *Journal of Climate*, **5(6)**, 541–560. https://doi.org/10.1175/1520-0442(1992)005<0541:AIOMFF>2.0.CO;2

Brindley, H. E., and R. J. Bantges. (2016). The Spectral Signature of Recent Climate Change. *Current Climate Change Reports*, **2(3)**, 112–126. https://doi.org/10.1007/s40641-016-0039-5

Brindley, H. E., and J. E. Russell. (2009). An assessment of Saharan dust loading and the corresponding cloud-free longwave direct radiative effect from geostationary satellite observations. *Journal of Geophysical Research*, **114(D23)**, D23201. https://doi.org/10.1029/2008JD011635

Burleyson, C. D., S. P. de Szoeke, S. E. Yuter, M. Wilbanks, and W. A. Brewer. (2013). Ship-Based Observations of the Diurnal Cycle of Southeast Pacific Marine Stratocumulus Clouds and Precipitation. *Journal of the Atmospheric Sciences*, **70(12)**, 3876–3894. https://doi.org/10.1175/JAS-D-13-01.1

Charney, J. G. (1975). Dynamics of deserts and drought in the Sahel. *Quarterly Journal of the Royal Meteorological Society*, **101(428)**, 193–202. https://doi.org/10.1002/qj.49710142802

Church, J. A., N. J. White, L. F. Konikow, C. M. Domingues, J. G. Cogley, E. Rignot, J. M. Gregory, M. R. van den Broeke, A. J. Monaghan, and I. Velicogna. (2011). Revisiting the Earth's sea-level and energy budgets from 1961 to 2008. *Geophysical Research Letters*, **38(18)**, L18601. https://doi.org/10.1029/2011GL048794

Coddington, O., J. L. Lean, P. Pilewskie, M. Snow, and D. Lindholm. (2016). A Solar Irradiance Climate Data Record. *Bulletin of the American Meteorological Society*, **97(7)**, 1265–1282. https://doi.org/10.1175/BAMS-D-14-00265.1

Coddington, O., P. Pilewskie, and T. Vukicevic. (2012). The Shannon information content of hyperspectral shortwave cloud albedo measurements: Quantification and practical applications. *Journal of Geophysical Research: Atmospheres*, **117(D4)**, D04205. https://doi.org/10.1029/2011JD016771

Comer, R. E., A. Slingo, and R. P. Allan. (2007). Observations of the diurnal cycle of outgoing longwave radiation from the Geostationary Earth Radiation Budget

instrument. *Geophysical Research Letters*, **34(2)**, L02823. https://doi.org/10.1029/2006GL028229

Cornforth, R. (2012). Overview of the West African Monsoon 20111. *Weather*, **67(3)**, 59–65. https://doi.org/10.1002/wea.1896

Costa, S. M. S., and K. P. Shine. (2012). Outgoing Longwave Radiation due to Directly Transmitted Surface Emission. *Journal of the Atmospheric Sciences*, **69(6)**, 1865–1870. https://doi.org/10.1175/JAS-D-11-0248.1

Crisp, N. H., K. Smith, and P. Hollingsworth. (2015). Launch and deployment of distributed small satellite systems. *Acta Astronautica*, **114**, 65–78. https://doi.org/10.1016/J.ACTAASTRO.2015.04.015

Dai, A., and K. E. Trenberth. (2004). The Diurnal Cycle and Its Depiction in the Community Climate System Model. *Journal of Climate*, **17(5)**, 930–951. https://doi.org/10.1175/1520-0442(2004)017<0930:TDCAID>2.0.CO;2

Dee, D. P., S. M. Uppala, A. J. Simmons, P. Berrisford, P. Poli, S. Kobayashi, U. Andrae, M. A. Balmaseda, G. Balsamo, P. Bauer, P. Bechtold, A. C. M. Beljaars, L. van de Berg, J. Bidlot, N. Bormann, C. Delsol, R. Dragani, M. Fuentes, A. J. Geer, L. Haimberger, S. B. Healy, H. Hersbach, E. V. Hólm, L. Isaksen, P. Kållberg, M. Köhler, M. Matricardi, A. P. McNally, B. M. Monge-Sanz, J.-J. Morcrette, B.-K. Park, C. Peubey, P. de Rosnay, C. Tavolato, J.-N. Thépaut, and F. Vitart. (2011). The ERA-Interim reanalysis: configuration and performance of the data assimilation system. *Quarterly Journal of the Royal Meteorological Society*, **137(656)**, 553–597. https://doi.org/10.1002/qj.828

Deser, C., and M. L. Blackmon. (1993). Surface Climate Variations over the North Atlantic Ocean during Winter: 1900–1989. *Journal of Climate*, **6(9)**, 1743–1753. https://doi.org/10.1175/1520-0442(1993)006<1743:SCVOTN>2.0.CO;2

Dessler, A. E. (2013). Observations of Climate Feedbacks over 2000–10 and Comparisons to Climate Models. *Journal of Climate*, **26(1)**, 333–342. https://doi.org/10.1175/JCLI-D-11-00640.1

Dewitte, S., and N. Clerbaux. (2017). Measurement of the Earth Radiation Budget at the Top of the Atmosphere—A Review. *Remote Sensing*, **9(11)**, 1143.

https://doi.org/10.3390/rs9111143

Dewitte, S., N. Clerbaux, A. Ipe, E. Baudrez, and J. Moreels. (2017). Dual view Geostationary Earth Radiation Budget from the Meteosat Second Generation satellites. In *EGU General Assembly* (Vol. 19, p. 6607). Vienna. Retrieved from http://adsabs.harvard.edu/abs/2017EGUGA..19.6607D

Dickinson, R. E. (1985). Climate Sensitivity. *Advances in Geophysics*, **28**, 99–129. https://doi.org/10.1016/S0065-2687(08)60221-6

Dines, W. H. (1917). The heat balance of the atmosphere. *Quarterly Journal of the Royal Meteorological Society*, **43(182)**, 151–158. https://doi.org/10.1002/qj.49704318203

Dodson, J. B., and P. C. Taylor. (2016). Sensitivity of Amazonian TOA flux diurnal cycle composite monthly variability to choice of reanalysis. *Journal of Geophysical Research: Atmospheres*, **121(9)**, 4404–4428. https://doi.org/10.1002/2015JD024567

Doelling, D. R., C. Haney, R. Bhatt, B. Scarino, and A. Gopalan. (2018). Geostationary Visible Imager Calibration for the CERES SYN1deg Edition 4 Product. *Remote Sensing*, **10(2)**, 288. https://doi.org/10.3390/rs10020288

Doelling, D. R., N. G. Loeb, D. F. Keyes, M. L. Nordeen, D. Morstad, C. Nguyen, B. A. Wielicki, D. F. Young, and M. Sun. (2013). Geostationary Enhanced Temporal Interpolation for CERES Flux Products. *Journal of Atmospheric and Oceanic Technology*, **30(6)**, 1072–1090. https://doi.org/10.1175/JTECH-D-12-00136.1

Doelling, D. R., M. Sun, L. T. Nguyen, M. L. Nordeen, C. O. Haney, D. F. Keyes, and P. E. Mlynczak. (2016). Advances in Geostationary-Derived Longwave Fluxes for the CERES Synoptic (SYN1deg) Product. *Journal of Atmospheric and Oceanic Technology*, **33(3)**, 503–521. https://doi.org/10.1175/JTECH-D-15-0147.1

Donlon, C. J., M. Martin, J. Stark, J. Roberts-Jones, E. Fiedler, and W. Wimmer. (2012). The Operational Sea Surface Temperature and Sea Ice Analysis (OSTIA) system. *Remote Sensing of Environment*, **116**, 140–158. https://doi.org/10.1016/j.rse.2010.10.017

Dudok de Wit, T., G. Kopp, C. Fröhlich, and M. Schöll. (2017). Methodology to create

a new total solar irradiance record: Making a composite out of multiple data records. *Geophysical Research Letters*, **44(3)**, 1196–1203. https://doi.org/10.1002/2016GL071866

Edwards, J. M., and A. Slingo. (1996). Studies with a flexible new radiation code. I: Choosing a configuration for a large-scale model. *Quarterly Journal of the Royal Meteorological Society*, **122(531)**, 689–719. https://doi.org/10.1002/qj.49712253107

Feldman, D. R., C. A. Algieri, W. D. Collins, Y. L. Roberts, and P. A. Pilewskie. (2011a). Simulation studies for the detection of changes in broadband albedo and shortwave nadir reflectance spectra under a climate change scenario. *Journal of Geophysical Research: Atmospheres*, **116(D24)**, D24103. https://doi.org/10.1029/2011JD016407

Feldman, D. R., C. A. Algieri, J. R. Ong, and W. D. Collins. (2011b). CLARREO shortwave observing system simulation experiments of the twenty-first century: Simulator design and implementation. *Journal of Geophysical Research*, **116(D10)**, D10107. https://doi.org/10.1029/2010JD015350

Finkensieper, S., J.-F. Meirink, G.-J. van Zadelhoff, T. Hanschmann, N. Benas, M. Stengel, P. Fuchs, R. Hollmann, and M. Werscheck. (2016). CLAAS-2: CM SAF CLoud property dAtAset using SEVIRI – Edition 2, Satellite Application Facility on Climate Monitoring. Darmstadt. https://doi.org/10.5676/EUM_SAF_CM/CLAAS/V002

Forster, P. M. F., and J. M. Gregory. (2006). The Climate Sensitivity and Its Components Diagnosed from Earth Radiation Budget Data. *Journal of Climate*, **19(1)**, 39–52. https://doi.org/10.1175/JCLI3611.1

Futyan, J. M., and J. E. Russell. (2005). Developing Clear-Sky Flux Products for the Geostationary Earth Radiation Budget Experiment. *Journal of Applied Meteorology*, **44(9)**, 1361–1374. https://doi.org/10.1175/JAM2291.1

Futyan, J. M., J. E. Russell, and J. E. Harries. (2005). Determining cloud forcing by cloud type from geostationary satellite data. *Geophysical Research Letters*, **32(8)**, L08807. https://doi.org/10.1029/2004GL022275

Georgieva, E., K. Priestley, B. Dunn, R. Cageao, A. Barki, J. Osmundsen, C. Turczynski, and N. Abedin. (2015). Radiation Budget Instrument (RBI) for JPSS-2. In *Conference on Characterization and Radiometric Calibration for Remote Sensing (CALCON)*. Retrieved from https://digitalcommons.usu.edu/calcon/CALCON2015/All2015Content/2

Gnevyshev, M. N. (1977). Essential features of the 11-year solar cycle. *Solar Physics*, **51(1)**, 175–183. https://doi.org/10.1007/BF00240455

Gottwald, M., and H. Bovensmann (Eds.). (2011). *SCIAMACHY - Exploring the Changing Earth's Atmosphere*. Dordrecht: Springer Netherlands. https://doi.org/10.1007/978-90-481-9896-2

Gray, L. J., J. Beer, M. Geller, J. D. Haigh, M. Lockwood, K. Matthes, U. Cubasch, D. Fleitmann, G. Harrison, L. Hood, J. Luterbacher, G. A. Meehl, D. Shindell, B. van Geel, and W. White. (2010). SOLAR INFLUENCES ON CLIMATE. *Reviews of Geophysics*, **48(4)**, RG4001. https://doi.org/10.1029/2009RG000282

Green, R. O., G. P. Asner, D. R. Thompson, P. Mouroulis, M. L. Eastwood, and S. Chien. (2017). A SmallSat Approach for Global Imaging Spectroscopy of the Earth SYSTEM Enabled by Advanced Technology. In *AGU Fall Meeting*. New Orleans. Retrieved from https://agu.confex.com/agu/fm17/meetingapp.cgi/Paper/275809

Gristey, J. J., J. C. Chiu, R. J. Gurney, S.-C. Han, and C. J. Morcrette. (2017). Determination of global Earth outgoing radiation at high temporal resolution using a theoretical constellation of satellites. *Journal of Geophysical Research: Atmospheres*, **122(2)**, 1114–1131. https://doi.org/10.1002/2016JD025514

Gruber, A. (1977). *Determination of the earth-atmosphere radiation budget from NOAA satellite data*. *Tech. Rep. NESS 76*. Washington D.C. Retrieved from http://adsabs.harvard.edu/abs/1977dear.rept.....G

Gruber, A., and A. F. Krueger. (1984). The Status of the NOAA Outgoing Longwave Radiation Data Set. *Bulletin of the American Meteorological Society*, **65(9)**, 958–962. https://doi.org/10.1175/1520-0477(1984)065<0958:TSOTNO>2.0.CO;2

Gruber, A., and J. S. Winston. (1978). Earth-Atmosphere Radiative Heating Based on

NOAA Scanning Radiometer Measurements. *Bulletin of the American Meteorological Society*, **59(12)**, 1570–1573. https://doi.org/10.1175/1520-0477(1978)059<1570:EARHBO>2.0.CO;2

Gu, G., and R. F. Adler. (2004). Seasonal Evolution and Variability Associated with the West African Monsoon System. *Journal of Climate*, **17(17)**, 3364–3377. https://doi.org/10.1175/1520-0442(2004)017<3364:SEAVAW>2.0.CO;2

Gupta, S. K., J. T. Suttles, S. N. Tiwari, and C. S. Vemuru. (1985). Infrared limb-darkening effects for the earth-atmosphere system. *AIAA Journal*, **23(3)**, 405–409. https://doi.org/10.2514/3.8927

Haigh, J. D., K. Matthes, and A. Hanslmeier. (2015). The Impact of Solar Variability on Climate. In J. Lilensten, T. Dudok de Wit, & K. Matthes (Eds.), *Earth's climate response to a changing Sun* (p. 360). EDP Sciences.

Han, S.-C., D. D. Rowlands, S. B. Luthcke, and F. G. Lemoine. (2008). Localized analysis of satellite tracking data for studying time-variable Earth's gravity fields. *Journal of Geophysical Research*, **113(B6)**, B06401. https://doi.org/10.1029/2007JB005218

Hannak, L., P. Knippertz, A. H. Fink, A. Kniffka, and G. Pante. (2017). Why Do Global Climate Models Struggle to Represent Low-Level Clouds in the West African Summer Monsoon? *Journal of Climate*, **30(5)**, 1665–1687. https://doi.org/10.1175/JCLI-D-16-0451.1

Hansen, J., L. Nazarenko, R. Ruedy, M. Sato, J. Willis, A. Del Genio, D. Koch, A. Lacis, K. Lo, S. Menon, T. Novakov, J. Perlwitz, G. Russell, G. A. Schmidt, and N. Tausnev. (2005). Earth's energy imbalance: confirmation and implications. *Science*, **308(5727)**, 1431–1435. https://doi.org/10.1126/science.1110252

Harries, J. E., J. E. Russell, J. A. Hanafin, H. Brindley, J. Futyan, J. Rufus, S. Kellock, G. Matthews, R. Wrigley, A. Last, J. Mueller, R. Mossavati, J. Ashmall, E. Sawyer, D. Parker, M. Caldwell, P. M. Allan, A. Smith, M. J. Bates, B. Coan, B. C. Stewart, D. R. Lepine, L. A. Cornwall, D. R. Corney, M. J. Ricketts, D. Drummond, D. Smart, R. Cutler, S. Dewitte, N. Clerbaux, L. Gonzalez, A. Ipe, C. Bertrand, A. Joukoff, D. Crommelynck, N. Nelms, D. T. Llewellyn-Jones, G. Butcher, G. L. Smith, Z. P. Szewczyk, P. E. Mlynczak, A. Slingo, R. P. Allan, and

M. A. Ringer. (2005). The Geostationary Earth Radiation Budget Project. *Bulletin of the American Meteorological Society*, **86(7)**, 945–960. https://doi.org/10.1175/BAMS-86-7-945

Harrison, E. F., P. Minnis, and G. Gibson. (1983). Orbital and cloud cover sampling analyses for multisatellite earth radiation budget experiments. *Journal of Spacecraft and Rockets*, **20(5)**, 491–495. https://doi.org/10.2514/3.25634

Hartmann, D. L. (1993). Radiative Effects of Clouds on Earth's Climate. In P. V. Hobbs (Ed.), *Aerosol--cloud--climate interactions*. Academic Press.

Hartmann, D. L., and P. Ceppi. (2014). Trends in the CERES Dataset, 2000–13: The Effects of Sea Ice and Jet Shifts and Comparison to Climate Models. *Journal of Climate*, **27(6)**, 2444–2456. https://doi.org/10.1175/JCLI-D-13-00411.1

Hastie, T., R. Tibshirani, and J. H. Friedman. (2009). *The elements of statistical learning : data mining, inference, and prediction*. New York: Springer-Verlag. https://doi.org/10.1007/978-0-387-84858-7

Hathaway, D. H. (2015). The Solar Cycle. *Living Reviews in Solar Physics*, **12(1)**, 4. https://doi.org/10.1007/lrsp-2015-4

Havemann, S., J.-C. Thelen, J. P. Taylor, and R. C. Harlow. (2018). The Havemann-Taylor Fast Radiative Transfer Code (HT-FRTC): a multipurpose code based on Principal Components. *Submitted to Journal of Quantitative Spectroscopy and Radiative Transfer*.

Haywood, J. M., A. Jones, N. Dunstone, S. Milton, M. Vellinga, A. Bodas-Salcedo, M. Hawcroft, B. Kravitz, J. Cole, S. Watanabe, and G. Stephens. (2016). The impact of equilibrating hemispheric albedos on tropical performance in the HadGEM2-ES coupled climate model. *Geophysical Research Letters*, **43(1)**, 395–403. https://doi.org/10.1002/2015GL066903

Hegerl, G. C., E. Black, R. P. Allan, W. J. Ingram, D. Polson, K. E. Trenberth, R. S. Chadwick, P. A. Arkin, B. B. Sarojini, A. Becker, A. Dai, P. J. Durack, D. Easterling, H. J. Fowler, E. J. Kendon, G. J. Huffman, C. Liu, R. Marsh, M. New, T. J. Osborn, N. Skliris, P. A. Stott, P.-L. Vidale, S. E. Wijffels, L. J. Wilcox, K. M. Willett, and X. Zhang. (2015). Challenges in Quantifying Changes in the

Global Water Cycle. *Bulletin of the American Meteorological Society*, **96(7)**, 1097–1115. https://doi.org/10.1175/BAMS-D-13-00212.1

Hill, P. G., R. P. Allan, J. C. Chiu, A. Bodas-Salcedo, and P. Knippertz. (2018). Quantifying the contribution of different cloud types to the radiation budget in southern West Africa. *Journal of Climate*. https://doi.org/10.1175/JCLI-D-17-0586.1

Hill, P. G., R. P. Allan, J. C. Chiu, and T. H. M. Stein. (2016). A multisatellite climatology of clouds, radiation, and precipitation in southern West Africa and comparison to climate models. *Journal of Geophysical Research: Atmospheres*, **121(18)**, 10,857-10,879. https://doi.org/10.1002/2016JD025246

Hourdin, F., T. Mauritsen, A. Gettelman, J.-C. Golaz, V. Balaji, Q. Duan, D. Folini, D. Ji, D. Klocke, Y. Qian, F. Rauser, C. Rio, L. Tomassini, M. Watanabe, and D. Williamson. (2017). The Art and Science of Climate Model Tuning. *Bulletin of the American Meteorological Society*, **98(3)**, 589–602. https://doi.org/10.1175/BAMS-D-15-00135.1

House, F. B., A. Gruber, G. E. Hunt, and A. T. Mecherikunnel. (1986). History of satellite missions and measurements of the Earth Radiation Budget (1957–1984). *Reviews of Geophysics*, **24(2)**, 357–377. https://doi.org/10.1029/RG024i002p00357

Hucek, R. R., P. Ardanuy, and H. L. Kyle. (1990). The Constrained Inversion of Nimbus-7 Wide Field-of-View Radiometer Measurements for the Earth Radiation Budget. *Journal of Applied Meteorology*, **29(11)**, 1085–1103. https://doi.org/10.1175/1520-0450(1990)029<1085:TCIONW>2.0.CO;2

Hucek, R. R., H. L. Kyle, and P. E. Ardanuy. (1987). Nimbus 7 earth radiation budget wide field of view climate data set improvement: 1. The Earth albedo from deconvolution of shortwave measurements. *Journal of Geophysical Research*, **92(D4)**, 4107. https://doi.org/10.1029/JD092iD04p04107

Ingram, J. (2015). *Quantifying the spatial and temporal response of UTH and OLR to deep convection over Tropical Africa*. Imperial College London. Retrieved from https://spiral.imperial.ac.uk:8443/handle/10044/1/29430

Itterly, K. F., and P. C. Taylor. (2014). Evaluation of the Tropical TOA Flux Diurnal Cycle in MERRA and ERA-Interim Retrospective Analyses. *Journal of Climate*, **27(13)**, 4781–4796. https://doi.org/10.1175/JCLI-D-13-00737.1

Jacobowitz, H., H. V. Soule, H. L. Kyle, and F. B. House. (1984). The Earth Radiation Budget (ERB) Experiment: An overview. *Journal of Geophysical Research: Atmospheres*, **89(D4)**, 5021–5038. https://doi.org/10.1029/JD089iD04p05021

Jakob, C., and G. Tselioudis. (2003). Objective identification of cloud regimes in the Tropical Western Pacific. *Geophysical Research Letters*, **30(21)**, 2082. https://doi.org/10.1029/2003GL018367

Johnson, G. C., J. M. Lyman, and N. G. Loeb. (2016). Improving estimates of Earth's energy imbalance. *Nature Climate Change*, **6(7)**, 639–640. https://doi.org/10.1038/nclimate3043

Kato, S., F. G. Rose, S. Sun-Mack, W. F. Miller, Y. Chen, D. A. Rutan, G. L. Stephens, N. G. Loeb, P. Minnis, B. A. Wielicki, D. M. Winker, T. P. Charlock, P. W. Stackhouse, K.-M. Xu, and W. D. Collins. (2011). Improvements of top-of-atmosphere and surface irradiance computations with CALIPSO-, CloudSat-, and MODIS-derived cloud and aerosol properties. *Journal of Geophysical Research*, **116(D19)**, D19209. https://doi.org/10.1029/2011JD016050

Kato, S., S. Sun-Mack, W. F. Miller, F. G. Rose, Y. Chen, P. Minnis, and B. A. Wielicki. (2010). Relationships among cloud occurrence frequency, overlap, and effective thickness derived from CALIPSO and CloudSat merged cloud vertical profiles. *Journal of Geophysical Research*, **115(D4)**, D00H28. https://doi.org/10.1029/2009JD012277

King, N. J., and G. Vaughan. (2012). Using passive remote sensing to retrieve the vertical variation of cloud droplet size in marine stratocumulus: An assessment of information content and the potential for improved retrievals from hyperspectral measurements. *Journal of Geophysical Research: Atmospheres*, **117(D15)**, D15206. https://doi.org/10.1029/2012JD017896

Knippertz, P., H. Coe, J. C. Chiu, M. J. Evans, A. H. Fink, N. Kalthoff, C. Liousse, C. Mari, R. P. Allan, B. Brooks, S. Danour, C. Flamant, O. O. Jegede, F. Lohou, and J. H. Marsham. (2015). The DACCIWA Project: Dynamics–Aerosol–Chemistry–

Cloud Interactions in West Africa. *Bulletin of the American Meteorological Society*, **96(9)**, 1451–1460. https://doi.org/10.1175/BAMS-D-14-00108.1

Kokhanovsky, A. A., V. V. Rozanov, W. Lotz, and M. Vountas. (2005). The SCIAMACHY cloud products: Algorithms and examples from ENVISAT. *Advances in Space Research*, **36(5)**, 789–799. https://doi.org/10.1016/J.ASR.2005.03.026

Komjathy, A., V. U. Zavorotny, P. Axelrad, G. H. Born, and J. L. Garrison. (2000). GPS Signal Scattering from Sea Surface. *Remote Sensing of Environment*, **73(2)**, 162–174. https://doi.org/10.1016/S0034-4257(00)00091-2

Kopp, G., and J. L. Lean. (2011). A new, lower value of total solar irradiance: Evidence and climate significance. *Geophysical Research Letters*, **38(1)**, L01706. https://doi.org/10.1029/2010GL045777

Kulu, E. (2018). Nanosatellites by launch years. Retrieved from http://www.nanosats.eu/

Kurucz, R., and B. Bell. (1995). Atomic Line Data. *CD-ROM No. 23. Cambridge, Mass.: Smithsonian Astrophysical Observatory*. Retrieved from http://adsabs.harvard.edu/abs/1995KurCD..23.....K

Kutzbach, J. E. (1967). Empirical Eigenvectors of Sea-Level Pressure, Surface Temperature and Precipitation Complexes over North America. *Journal of Applied Meteorology*, **6(5)**, 791–802. https://doi.org/10.1175/1520-0450(1967)006<0791:EEOSLP>2.0.CO;2

Kyle, H. L., A. Arking, J. R. Hickey, P. E. Ardanuy, H. Jacobowitz, L. L. Stowe, G. G. Campbell, T. Vonder Haar, F. B. House, R. Maschhoff, and G. L. Smith. (1993). The Nimbus Earth Radiation Budget (ERB) Experiment: 1975 to 1992. *Bulletin of the American Meteorological Society*, **74(5)**, 815–830. https://doi.org/10.1175/1520-0477(1993)074<0815:TNERBE>2.0.CO;2

Kyle, H. L., E. J. Hurley, and P. E. Ardanuy. (1985). The Status of the Nimbus-7 Earth-Radiation-Budget Data Set. *Bulletin of the American Meteorological Society*, **66(11)**, 1378–1388. https://doi.org/10.1175/1520-0477(1985)066<1378:TSOTER>2.0.CO;2

Lockwood, M. (2012). Solar Influence on Global and Regional Climates. *Surveys in Geophysics*, **33(3–4)**, 503–534. https://doi.org/10.1007/s10712-012-9181-3

Loeb, N. G., D. R. Doelling, H. Wang, W. Su, C. Nguyen, J. G. Corbett, L. Liang, C. Mitrescu, F. G. Rose, and S. Kato. (2018). Clouds and the Earth's Radiant Energy System (CERES) Energy Balanced and Filled (EBAF) Top-of-Atmosphere (TOA) Edition-4.0 Data Product. *Journal of Climate*, **31(2)**, 895–918. https://doi.org/10.1175/JCLI-D-17-0208.1

Loeb, N. G., and S. Kato. (2002). Top-of-Atmosphere Direct Radiative Effect of Aerosols over the Tropical Oceans from the Clouds and the Earth's Radiant Energy System (CERES) Satellite Instrument. *Journal of Climate*, **15(12)**, 1474–1484. https://doi.org/10.1175/1520-0442(2002)015<1474:TOADRE>2.0.CO;2

Loeb, N. G., S. Kato, K. Loukachine, and N. Manalo-Smith. (2005). Angular Distribution Models for Top-of-Atmosphere Radiative Flux Estimation from the Clouds and the Earth's Radiant Energy System Instrument on the *Terra* Satellite. Part I: Methodology. *Journal of Atmospheric and Oceanic Technology*, **22(4)**, 338–351. https://doi.org/10.1175/JTECH1712.1

Loeb, N. G., N. Manalo-Smith, S. Kato, W. F. Miller, S. K. Gupta, P. Minnis, and B. A. Wielicki. (2003). Angular Distribution Models for Top-of-Atmosphere Radiative Flux Estimation from the Clouds and the Earth's Radiant Energy System Instrument on the Tropical Rainfall Measuring Mission Satellite. Part I: Methodology. *Journal of Applied Meteorology*, **42(2)**, 240–265. https://doi.org/10.1175/1520-0450(2003)042<0240:ADMFTO>2.0.CO;2

Loeb, N. G., B. A. Wielicki, D. R. Doelling, G. L. Smith, D. F. Keyes, S. Kato, N. Manalo-Smith, and T. Wong. (2009). Toward Optimal Closure of the Earth's Top-of-Atmosphere Radiation Budget. *Journal of Climate*, **22(3)**, 748–766. https://doi.org/10.1175/2008JCLI2637.1

Loeb, N. G., B. A. Wielicki, F. G. Rose, and D. R. Doelling. (2007). Variability in global top-of-atmosphere shortwave radiation between 2000 and 2005. *Geophysical Research Letters*, **34(3)**, L03704. https://doi.org/10.1029/2006GL028196

London, J. A. (1957). *A study of the atmospheric heat balance*. New York.

Love, B. S., A. J. Matthews, and G. M. S. Lister. (2011). The diurnal cycle of precipitation over the Maritime Continent in a high-resolution atmospheric model. *Quarterly Journal of the Royal Meteorological Society*, **137(657)**, 934–947. https://doi.org/10.1002/qj.809

Lücking, C., C. Colombo, and C. McInnes. (2011). A passive de-orbiting strategy for high altitude CubeSat missions using a deployable reflective balloon. In *8th IAA Symposium on Small Satellites*. Berlin.

Lyman, J. M., S. A. Good, V. V. Gouretski, M. Ishii, G. C. Johnson, M. D. Palmer, D. M. Smith, and J. K. Willis. (2010). Robust warming of the global upper ocean. *Nature*, **465(7296)**, 334–337. https://doi.org/10.1038/nature09043

Mace, G. G., and F. J. Wrenn. (2013). Evaluation of the Hydrometeor Layers in the East and West Pacific within ISCCP Cloud-Top Pressure–Optical Depth Bins Using Merged CloudSat and CALIPSO Data. *Journal of Climate*, **26(23)**, 9429–9444. https://doi.org/10.1175/JCLI-D-12-00207.1

Maessen, D. C. (2007). *Development of a generic inflatable de-orbit device for CubeSats*. TU Delft, Aerospace Engineering, Design and Production of Composite Structures. Retrieved from https://repository.tudelft.nl/islandora/object/uuid%3A49d86db1-8909-4464-af1b-fe1655c9c376

Manners, J., J.-C. Thelen, J. Petch, P. Hill, and J. M. Edwards. (2009). Two fast radiative transfer methods to improve the temporal sampling of clouds in numerical weather prediction and climate models. *Quarterly Journal of the Royal Meteorological Society*, **135(639)**, 457–468. https://doi.org/10.1002/qj.385

Marsham, J. H., N. S. Dixon, L. Garcia-Carreras, G. M. S. Lister, D. J. Parker, P. Knippertz, and C. E. Birch. (2013). The role of moist convection in the West African monsoon system: Insights from continental-scale convection-permitting simulations. *Geophysical Research Letters*, **40(9)**, 1843–1849. https://doi.org/10.1002/grl.50347

Mauritsen, T., B. Stevens, E. Roeckner, T. Crueger, M. Esch, M. Giorgetta, H. Haak, J. Jungclaus, D. Klocke, D. Matei, U. Mikolajewicz, D. Notz, R. Pincus, H. Schmidt, and L. Tomassini. (2012). Tuning the climate of a global model. *Journal of*

Advances in Modeling Earth Systems, **4(3)**, M00A01. https://doi.org/10.1029/2012MS000154

Mitchell, T. (2013). Sahel Precipitation Index. https://doi.org/10.6069/H5MW2F2Q

Nag, S., C. K. Gatebe, and O. de Weck. (2015). Observing system simulations for small satellite formations estimating bidirectional reflectance. *International Journal of Applied Earth Observation and Geoinformation*, **43**, 102–118. https://doi.org/10.1016/j.jag.2015.04.022

Nesbitt, S. W., and E. J. Zipser. (2003). The Diurnal Cycle of Rainfall and Convective Intensity according to Three Years of TRMM Measurements. *Journal of Climate*, **16(10)**, 1456–1475. https://doi.org/10.1175/1520-0442-16.10.1456

Nitta, T., and S. Sekine. (1994). Diurnal Variation of Convective Activity over the Tropical Western Pacific. *Journal of the Meteorological Society of Japan. Ser. II*, **72(5)**, 627–641. https://doi.org/10.2151/jmsj1965.72.5_627

Ogawa, K., and T. Schmugge. (2004). Mapping Surface Broadband Emissivity of the Sahara Desert Using ASTER and MODIS Data. *Earth Interactions*, **8(7)**, 1–14. https://doi.org/10.1175/1087-3562(2004)008<0001:MSBEOT>2.0.CO;2

Oreopoulos, L., N. Cho, and D. Lee. (2017). New insights about cloud vertical structure from CloudSat and CALIPSO observations. *Journal of Geophysical Research: Atmospheres*, **122(17)**, 9280–9300. https://doi.org/10.1002/2017JD026629

Oreopoulos, L., N. Cho, D. Lee, S. Kato, and G. J. Huffman. (2014). An examination of the nature of global MODIS cloud regimes. *Journal of Geophysical Research: Atmospheres*, **119(13)**, 8362–8383. https://doi.org/10.1002/2013JD021409

Owens, M. J., M. Lockwood, E. Hawkins, I. Usoskin, G. S. Jones, L. Barnard, A. Schurer, and J. Fasullo. (2017). The Maunder minimum and the Little Ice Age: an update from recent reconstructions and climate simulations. *Journal of Space Weather and Space Climate*, **7**, A33. https://doi.org/10.1051/swsc/2017034

Pfeifroth, U., R. Hollmann, and B. Ahrens. (2012). Cloud Cover Diurnal Cycles in Satellite Data and Regional Climate Model Simulations. *Meteorologische Zeitschrift*, **21(6)**, 551–560. https://doi.org/10.1127/0941-2948/2012/0423

Pilewskie, P., and S. Twomey. (1987). Discrimination of ice from water in clouds by

optical remote sensing. *Atmospheric Research*, **21(2)**, 113–122. https://doi.org/10.1016/0169-8095(87)90002-0

Poghosyan, A., and A. Golkar. (2017). CubeSat evolution: Analyzing CubeSat capabilities for conducting science missions. *Progress in Aerospace Sciences*, **88**, 59–83. https://doi.org/10.1016/J.PAEROSCI.2016.11.002

Puig-Suari, J., C. Turner, and R. J. Twiggs. (2001). CubeSat: The Development and Launch Support Infrastructure for Eighteen Different Satellite Customers on One Launch. In *AIAA/USU Conference on Small Satellites*.

Qian, J.-H. (2008). Why Precipitation Is Mostly Concentrated over Islands in the Maritime Continent. *Journal of the Atmospheric Sciences*, **65(4)**, 1428–1441. https://doi.org/10.1175/2007JAS2422.1

Ramanathan, V. (1987). The role of earth radiation budget studies in climate and general circulation research. *Journal of Geophysical Research*, **92(D4)**, 4075–4095. https://doi.org/10.1029/JD092iD04p04075

Rao, P. K. (1964). Seasonal variations of outgoing long-wave radiation as observed by TIROS II and TIROS III satellites. *Weather*, **19(3)**, 88–89. https://doi.org/10.1002/j.1477-8696.1964.tb02077.x

Rasool, S. I., and C. Prabhakara. (1966). Heat budget of the Southern Hemisphere. In R. V. Garcia & T. F. Malone (Eds.), *Problems of Atmospheric Circulation* (pp. 76–92). New York: Spartan Books.

Ricchiazzi, P., S. Yang, C. Gautier, and D. Sowle. (1998). SBDART: A Research and Teaching Software Tool for Plane-Parallel Radiative Transfer in the Earth's Atmosphere. *Bulletin of the American Meteorological Society*, **79(10)**, 2101–2114. https://doi.org/10.1175/1520-0477(1998)079<2101:SARATS>2.0.CO;2

Roberts, Y. L., P. Pilewskie, D. R. Feldman, B. C. Kindel, and W. D. Collins. (2014). Temporal variability of observed and simulated hyperspectral reflectance. *Journal of Geophysical Research: Atmospheres*, **119(17)**, 10,262-10,280. https://doi.org/10.1002/2014JD021566

Roberts, Y. L., P. Pilewskie, and B. C. Kindel. (2011). Evaluating the observed variability in hyperspectral Earth-reflected solar radiance. *Journal of Geophysical*

Research: Atmospheres, **116(D24)**, D24119. https://doi.org/10.1029/2011JD016448

Roberts, Y. L., P. Pilewskie, B. C. Kindel, D. R. Feldman, and W. D. Collins. (2013). Quantitative comparison of the variability in observed and simulated shortwave reflectance. *Atmospheric Chemistry and Physics*, **13(6)**, 3133–3147. https://doi.org/10.5194/acp-13-3133-2013

Rossow, W. B., and R. A. Schiffer. (1999). Advances in Understanding Clouds from ISCCP. *Bulletin of the American Meteorological Society*, **80(11)**, 2261–2287. https://doi.org/10.1175/1520-0477(1999)080<2261:AIUCFI>2.0.CO;2

Ruf, C. S., S. Gleason, Z. Jelenak, S. Katzberg, A. Ridley, R. Rose, J. Scherrer, and V. Zavorotny. (2012). The CYGNSS nanosatellite constellation hurricane mission. In *IEEE International Geoscience and Remote Sensing Symposium* (pp. 214–216). Munich: IEEE. https://doi.org/10.1109/IGARSS.2012.6351600

Rutan, D. A., G. L. Smith, and T. Wong. (2014). Diurnal Variations of Albedo Retrieved from Earth Radiation Budget Experiment Measurements. *Journal of Applied Meteorology and Climatology*, **53(12)**, 2747–2760. https://doi.org/10.1175/JAMC-D-13-0119.1

Salby, M. L. (1988a). Asynoptic Sampling Considerations for Wide-Field-of-View Measurements of Outgoing Radiation. Part I: Spatial and Temporal Resolution. *Journal of the Atmospheric Sciences*, **45(7)**, 1176–1183. https://doi.org/10.1175/1520-0469(1988)045<1176:ASCFWF>2.0.CO;2

Salby, M. L. (1988b). Asynoptic Sampling Considerations for Wide-Field-of-View Measurements of Outgoing Radiation. Part II: Diurnal and Random Space-Time Variability. *Journal of the Atmospheric Sciences*, **45(7)**, 1184–1204. https://doi.org/10.1175/1520-0469(1988)045<1184:ASCFWF>2.0.CO;2

Sandau, R., K. Brieß, and M. D'Errico. (2010). Small satellites for global coverage: Potential and limits. *ISPRS Journal of Photogrammetry and Remote Sensing*, **65(6)**, 492–504. https://doi.org/10.1016/j.isprsjprs.2010.09.003

Schmid, J. (2000). The SEVIRI instrument. In *EUMETSAT Meteorological Satellite Data Users' Conference*. Bologna. Retrieved from

https://pdfs.semanticscholar.org/d9f2/6fae503fbc743f336b0fba48f1175d3151f9.pdf

Slingo, A., K. I. Hodges, and G. J. Robinson. (2004). Simulation of the diurnal cycle in a climate model and its evaluation using data from Meteosat 7. *Quarterly Journal of the Royal Meteorological Society*, **130(599)**, 1449–1467. https://doi.org/10.1256/qj.03.165

Smith, G. L., P. E. Mlynczak, D. A. Rutan, and T. Wong. (2008). Comparison of the Diurnal Cycle of Outgoing Longwave Radiation from a Climate Model with Results from ERBE. *Journal of Applied Meteorology and Climatology*, **47(12)**, 3188–3201. https://doi.org/10.1175/2008JAMC1924.1

Smith, G. L., and D. A. Rutan. (2003). The Diurnal Cycle of Outgoing Longwave Radiation from Earth Radiation Budget Experiment Measurements. *Journal of the Atmospheric Sciences*, **60(13)**, 1529–1542. https://doi.org/10.1175/2997.1

Smith, W. L., J. Hickey, H. B. Howell, H. Jacobowitz, D. T. Hilleary, and A. J. Drummond. (1977). Nimbus-6 earth radiation budget experiment. *Applied Optics*, **16(2)**, 306–318. https://doi.org/10.1364/AO.16.000306

Soden, B. J. (2000). The diurnal cycle of convection, clouds, and water vapor in the tropical upper troposphere. *Geophysical Research Letters*, **27(15)**, 2173–2176. https://doi.org/10.1029/2000GL011436

Soden, B. J., I. M. Held, R. Colman, K. M. Shell, J. T. Kiehl, and C. A. Shields. (2008). Quantifying Climate Feedbacks Using Radiative Kernels. *Journal of Climate*, **21(14)**, 3504–3520. https://doi.org/10.1175/2007JCLI2110.1

Stein, T. H. M., D. J. Parker, J. Delanoë, N. S. Dixon, R. J. Hogan, P. Knippertz, R. I. Maidment, and J. H. Marsham. (2011). The vertical cloud structure of the West African monsoon: A 4 year climatology using CloudSat and CALIPSO. *Journal of Geophysical Research: Atmospheres*, **116(D22)**, D22205. https://doi.org/10.1029/2011JD016029

Stephens, G. L., M. Z. Hakuba, M. Hawcroft, J. M. Haywood, A. Behrangi, J. E. Kay, and P. J. Webster. (2016). The Curious Nature of the Hemispheric Symmetry of the Earth's Water and Energy Balances. *Current Climate Change Reports*, **2(4)**,

135–147. https://doi.org/10.1007/s40641-016-0043-9

Stephens, G. L., and T. L'Ecuyer. (2015). The Earth's energy balance. *Atmospheric Research*, **166**, 195–203. https://doi.org/10.1016/J.ATMOSRES.2015.06.024

Stephens, G. L., J. Li, M. Wild, C. A. Clayson, N. Loeb, S. Kato, T. L'Ecuyer, P. W. Stackhouse, M. Lebsock, and T. Andrews. (2012). An update on Earth's energy balance in light of the latest global observations. *Nature Geoscience*, **5(10)**, 691–696. https://doi.org/10.1038/ngeo1580

Stephens, G. L., D. O'Brien, P. J. Webster, P. Pilewski, S. Kato, and J. Li. (2015). The albedo of Earth. *Reviews of Geophysics*, **53(1)**, 141–163. https://doi.org/10.1002/2014RG000449

Stephens, G. L., S. van den Heever, and L. Pakula. (2008). Radiative–Convective Feedbacks in Idealized States of Radiative–Convective Equilibrium. *Journal of the Atmospheric Sciences*, **65(12)**, 3899–3916. https://doi.org/10.1175/2008JAS2524.1

Stockli, R., E. Vermote, N. Z. Saleous, R. Simmon, and D. Herring. (2005). *The Blue Marble Next Generation - A true color earth dataset including seasonal dynamics from MODIS*. Retrieved from https://www.researchgate.net/publication/252137621_The_Blue_Marble_Next_Generation_-_A_true_color_earth_dataset_including_seasonal_dynamics_from_MODIS

Su, W., J. Corbett, Z. Eitzen, and L. Liang. (2015). Next-generation angular distribution models for top-of-atmosphere radiative flux calculation from CERES instruments: methodology. *Atmospheric Measurement Techniques*, **8(2)**, 611–632. https://doi.org/10.5194/amt-8-611-2015

Suomi, V. E. (1960). The Thermal Radiation Balance Experiment on Board Explorer VII. In *JUNO ZZ Summary Project Report* (pp. 247–278). Huntsville.

Suttles, J., R. Green, P. Minnis, G. Smith, W. Staylor, B. Wielicki, I. Walker, D. Young, V. Taylor, and L. Stowe. (1988). *Angular Radiation Models for Earth-Atmosphere Systems, Vol. I Shortwave Radiation*. Hampton.

Suttles, J., R. Green, G. Smith, B. Wielicki, I. Walker, V. Taylor, and L. Stowe. (1989).

Angular Radiation Models for Earth-Atmosphere Systems, Vol. II Longwave Radiation. Hampton.

Swartz, W. H., L. P. Dyrud, S. R. Lorentz, D. L. Wu, W. J. Wiscombe, S. J. Papadakis, P. M. Huang, E. L. Reynolds, A. W. Smith, and D. M. Deglau. (2015). The RAVAN CubeSat mission: Advancing technologies for climate observation. In *IEEE International Geoscience and Remote Sensing Symposium (IGARSS)* (pp. 5300–5303). Milan: IEEE. https://doi.org/10.1109/IGARSS.2015.7327031

Swartz, W. H., S. Lorentz, P. Huang, A. Smith, J. Biscoe, J. Carvo, D. Wu, and E. L. Reynolds. (2017). RAVAN CubeSat Results: Technologies and Science Demonstrated On Orbit. In *AIAA/USU Conference on Small Satellites*. Retrieved from https://digitalcommons.usu.edu/cgi/viewcontent.cgi?article=3673&context=smallsat

Swartz, W. H., S. Lorentz, P. Huang, A. Smith, D. Deglau, S. Liang, K. Marcotte, E. Reynolds, S. Papadakis, L. Dyrud, D. Wu, W. Wiscombe, and J. Carvo. (2016). The Radiometer Assessment using Vertically Aligned Nanotubes (RAVAN) CubeSat Mission: A Pathfinder for a New Measurement of Earth's Radiation Budget. In *AIAA/USU Conference on Small Satellites*. Retrieved from https://digitalcommons.usu.edu/smallsat/2016/TS12SciPayload2/3

Taylor, P. C. (2012). Tropical Outgoing Longwave Radiation and Longwave Cloud Forcing Diurnal Cycles from CERES. *Journal of the Atmospheric Sciences*, **69(12)**, 3652–3669. https://doi.org/10.1175/JAS-D-12-088.1

Taylor, P. C. (2014). Variability of Regional TOA Flux Diurnal Cycle Composites at the Monthly Time Scale. *Journal of the Atmospheric Sciences*, **71(9)**, 3484–3498. https://doi.org/10.1175/JAS-D-13-0336.1

Tett, S. F. B., M. J. Mineter, C. Cartis, D. J. Rowlands, and P. Liu. (2013a). Can Top-of-Atmosphere Radiation Measurements Constrain Climate Predictions? Part I: Tuning. *Journal of Climate*, **26(23)**, 9348–9366. https://doi.org/10.1175/JCLI-D-12-00595.1

Tett, S. F. B., D. J. Rowlands, M. J. Mineter, and C. Cartis. (2013b). Can Top-of-Atmosphere Radiation Measurements Constrain Climate Predictions? Part II:

Climate Sensitivity. *Journal of Climate*, **26(23)**, 9367–9383. https://doi.org/10.1175/JCLI-D-12-00596.1

Tian, B., B. J. Soden, and X. Wu. (2004). Diurnal cycle of convection, clouds, and water vapor in the tropical upper troposphere: Satellites versus a general circulation model. *Journal of Geophysical Research*, **109(D10)**, D10101. https://doi.org/10.1029/2003JD004117

Trenberth, K. E. (2009). An imperative for climate change planning: tracking Earth's global energy. *Current Opinion in Environmental Sustainability*, **1(1)**, 19–27. https://doi.org/10.1016/j.cosust.2009.06.001

Trenberth, K. E., and J. T. Fasullo. (2012). Tracking Earth's Energy: From El Niño to Global Warming. *Surveys in Geophysics*, **33(3–4)**, 413–426. https://doi.org/10.1007/s10712-011-9150-2

Tselioudis, G., W. Rossow, Y. Zhang, and D. Konsta. (2013). Global Weather States and Their Properties from Passive and Active Satellite Cloud Retrievals. *Journal of Climate*, **26(19)**, 7734–7746. https://doi.org/10.1175/JCLI-D-13-00024.1

Underwood, C., S. Machin, P. Stephens, D. Hodgson, A. da Silva Curiel, and M. Sweeting. (2005). Evaluation of the utility of theDisaster Monitoring Constellation in support of Earth observation applications. In *Fifth IAA Symposium on Small Satellites for Earth Observation*. Berlin.

Usoskin, I. G. (2017). A history of solar activity over millennia. *Living Reviews in Solar Physics*, **14(1)**, 3. https://doi.org/10.1007/s41116-017-0006-9

Viollier, M., and P. Raberanto. (2010). Radiometric and Spectral Characteristics of the ScaRaB-3 Instrument on Megha-Tropiques: Comparisons with ERBE, CERES, and GERB. *Journal of Atmospheric and Oceanic Technology*, **27(3)**, 428–442. https://doi.org/10.1175/2009JTECHA1307.1

Voigt, A., B. Stevens, J. Bader, and T. Mauritsen. (2013). The Observed Hemispheric Symmetry in Reflected Shortwave Irradiance. *Journal of Climate*, **26(2)**, 468–477. https://doi.org/10.1175/JCLI-D-12-00132.1

Voigt, A., B. Stevens, J. Bader, and T. Mauritsen. (2014). Compensation of Hemispheric Albedo Asymmetries by Shifts of the ITCZ and Tropical Clouds.

Journal of Climate, **27(3)**, 1029–1045. https://doi.org/10.1175/JCLI-D-13-00205.1

von Hoyningen-Huene, W., A. A. Kokhanovsky, M. W. Wuttke, M. Buchwitz, S. Noël, K. Gerilowski, J. P. Burrows, B. Latter, R. Siddans, and B. J. Kerridge. (2007). Validation of SCIAMACHY top-of-atmosphere reflectance for aerosol remote sensing using MERIS L1 data. *Atmospheric Chemistry and Physics*, **7(1)**, 97–106. https://doi.org/10.5194/acp-7-97-2007

Vonder Haar, T. H., and V. E. Suomi. (1971). Measurements of the Earth's Radiation Budget from Satellites During a Five-Year Period. Part I: Extended Time and Space Means. *Journal of the Atmospheric Sciences*, **28(3)**, 305–314. https://doi.org/10.1175/1520-0469(1971)028<0305:MOTERB>2.0.CO;2

Wallace, J. M., C. Smith, and C. S. Bretherton. (1992). Singular Value Decomposition of Wintertime Sea Surface Temperature and 500-mb Height Anomalies. *Journal of Climate*, **5(6)**, 561–576. https://doi.org/10.1175/1520-0442(1992)005<0561:SVDOWS>2.0.CO;2

Walters, D., I. Boutle, M. Brooks, T. Melvin, R. Stratton, S. Vosper, H. Wells, K. Williams, N. Wood, T. Allen, A. Bushell, D. Copsey, P. Earnshaw, J. Edwards, M. Gross, S. Hardiman, C. Harris, J. Heming, N. Klingaman, R. Levine, J. Manners, G. Martin, S. Milton, M. Mittermaier, C. Morcrette, T. Riddick, M. Roberts, C. Sanchez, P. Selwood, A. Stirling, C. Smith, D. Suri, W. Tennant, P. L. Vidale, J. Wilkinson, M. Willett, S. Woolnough, and P. Xavier. (2017). The Met Office Unified Model Global Atmosphere 6.0/6.1 and JULES Global Land 6.0/6.1 configurations. *Geoscientific Model Development*, **10(4)**, 1487–1520. https://doi.org/10.5194/gmd-10-1487-2017

Walters, D. N., K. D. Williams, I. A. Boutle, A. C. Bushell, J. M. Edwards, P. R. Field, A. P. Lock, C. J. Morcrette, R. A. Stratton, J. M. Wilkinson, M. R. Willett, N. Bellouin, A. Bodas-Salcedo, M. E. Brooks, D. Copsey, P. D. Earnshaw, S. C. Hardiman, C. M. Harris, R. C. Levine, C. MacLachlan, J. C. Manners, G. M. Martin, S. F. Milton, M. D. Palmer, M. J. Roberts, J. M. Rodríguez, W. J. Tennant, and P. L. Vidale. (2014). The Met Office Unified Model Global Atmosphere 4.0 and JULES Global Land 4.0 configurations. *Geoscientific Model Development*, **7(1)**, 361–386. https://doi.org/10.5194/gmd-7-361-2014

Webster, P. J., C. A. Clayson, and J. A. Curry. (1996). Clouds, Radiation, and the Diurnal Cycle of Sea Surface Temperature in the Tropical Western Pacific. *Journal of Climate*, **9(8)**, 1712–1730. https://doi.org/10.1175/1520-0442(1996)009<1712:CRATDC>2.0.CO;2

Weinstein, M., and V. E. Suomi. (1961). ANALYSIS OF SATELLITE INFRARED RADIATION MEASUREMENTS ON A SYNOPTIC SCALE. *Monthly Weather Review*, **89(11)**, 419–428. https://doi.org/10.1175/1520-0493(1961)089<0419:AOSIRM>2.0.CO;2

Wielicki, B. A., B. R. Barkstrom, E. F. Harrison, R. B. Lee, G. Louis Smith, and J. E. Cooper. (1996). Clouds and the Earth's Radiant Energy System (CERES): An Earth Observing System Experiment. *Bulletin of the American Meteorological Society*, **77(5)**, 853–868. https://doi.org/10.1175/1520-0477(1996)077<0853:CATERE>2.0.CO;2

Wielicki, B. A., D. R. Doelling, D. F. Young, N. G. Loeb, D. P. Garber, and D. G. MacDonnell. (2008). Climate Quality Broadband and Narrowband Solar Reflected Radiance Calibration Between Sensors in Orbit. In *IGARSS 2008 - 2008 IEEE International Geoscience and Remote Sensing Symposium* (p. I-257-I-260). IEEE. https://doi.org/10.1109/IGARSS.2008.4778842

Wild, M., D. Folini, M. Z. Hakuba, C. Schär, S. I. Seneviratne, S. Kato, D. Rutan, C. Ammann, E. F. Wood, and G. König-Langlo. (2015). The energy balance over land and oceans: an assessment based on direct observations and CMIP5 climate models. *Climate Dynamics*, **44(11–12)**, 3393–3429. https://doi.org/10.1007/s00382-014-2430-z

Williams, K. D., and G. Tselioudis. (2007). GCM intercomparison of global cloud regimes: present-day evaluation and climate change response. *Climate Dynamics*, **29(2–3)**, 231–250. https://doi.org/10.1007/s00382-007-0232-2

Williams, K. D., and M. J. Webb. (2009). A quantitative performance assessment of cloud regimes in climate models. *Climate Dynamics*, **33(1)**, 141–157. https://doi.org/10.1007/s00382-008-0443-1

Wiscombe, W., and C. Chiu. (2013). The next step in Earth radiation budget measurements. In *AIP Conf. Proc.* (pp. 648–651).

https://doi.org/10.1063/1.4804853

Wood, R., C. S. Bretherton, and D. L. Hartmann. (2002). Diurnal cycle of liquid water path over the subtropical and tropical oceans. *Geophysical Research Letters*, **29(23)**, 2092. https://doi.org/10.1029/2002GL015371

Yang, G.-Y., and J. Slingo. (2001). The Diurnal Cycle in the Tropics. *Monthly Weather Review*, **129(4)**, 784–801. https://doi.org/10.1175/1520-0493(2001)129<0784:TDCITT>2.0.CO;2

Young, M. (2015). *Improved rainfall monitoring for Africa*. University of Reading.

Zhang, R.-H., and Z. Liu. (1999). Decadal Thermocline Variability in the North Pacific Ocean: Two Pathwaysaround the Subtropical Gyre. *Journal of Climate*, **12(11)**, 3273–3296. https://doi.org/10.1175/1520-0442(1999)012<3273:DTVITN>2.0.CO;2

Zhang, Y., S. Klein, G. G. Mace, and J. Boyle. (2007). Cluster analysis of tropical clouds using CloudSat data. *Geophysical Research Letters*, **34(12)**, L12813. https://doi.org/10.1029/2007GL029336

7 APPENDIX I: List of acronyms

The following list provides a reference for every acronym defined in this thesis. Note that each figure caption, chapter summary and chapter are written as stand-alone with respect to definition of acronyms. As a result, some acronyms are defined more than once within this thesis, and previously defined acronyms are sometimes spelt out.

ADM	Angular distribution model
ASTER	Advanced Spaceborne Thermal Emission and Reflection Radiometer
A-Train	Afternoon-Train
CALIOP	Cloud-Aerosol Lidar with Orthogonal Polarization
CALIPSO	Cloud-Aerosol Lidar and Infrared Pathfinder Satellite Observations
CASE	Collaborative Awards in Science and Engineering
CCCM	CloudSat-CALIPSO-CERES-MODIS
CERES	Clouds and the Earth's Radiant Energy System
CLAAS	Cloud Property DAtAset using SEVIRI
CMSAF	Climate Monitoring Satellite Applications Facility
CPR	Cloud Profiling Radar
CTH	Cloud top height
DISORT	Discrete Ordinate Radiative Transfer
EBAF	Energy Balanced And Filled
ENVISAT	Environmental Satellite
EOF	Empirical orthogonal function
EOR	Earth outgoing radiation
ERA	European Reanalysis

ERB	Earth radiation budget
ERBE	Earth Radiation Budget Experiment
ERBS	Earth Radiation Budget Satellite
ESA	European Space Agency
ESSA	Environmental Sciences Service Administration
FOV	Field-of-view
GA6	Global Atmosphere 6.0
GEOS	Goddard Earth Observing System Model
GERB	Geostationary Earth Radiation Budget
GL6	Global Land 6.0
HT-FRTC	Havemann-Taylor Fast Radiative Transfer Code
ISCCP	International Satellite Cloud Climatology Project
ITCZ	Intertropical convergence zone
IWP	Ice water path
JPL	Jet Propulsion Laboratory
LW	Long-wave
LWP	Liquid water path
MODIS	Moderate Resolution Imaging Spectroradiometer
NASA	National Aeronautics and Space Administration
NERC	Natural Environment Research Council
NFOV	Narrow-field-of-view
NH	Northern Hemisphere
NOAA	National Oceanic and Atmospheric Administration
NWP	Numerical Weather Prediction

OLR	Outgoing long-wave radiation
PC	Principal component
PCA	Principal component analysis
RAVAN	Radiometer Assessment using Vertically Aligned Nanotubes
RMSD	Root-mean-square difference
RMSE	Root-mean-square error
RS	Rayleigh scattering
RSR	Reflected short-wave radiation OR reflected solar radiation
ScaRaB	Scanner for Radiation Budget
SCENARIO	SCience of the Environment: Natural and Anthropogenic pRocesses, Impacts and Opportunities
SCIAMACHY	SCanning Imaging Absorption spectroMeter for Atmospheric CHartographY
SEVIRI	Spinning Enhanced Visible and InfraRed Imager
SH	Southern Hemisphere
SNR	Signal-to-noise ratio
SORCE	Solar Radiation and Climate Experiment
SW	Short-wave
SWCRE	Short-wave cloud radiative effect
SZA	Solar zenith angle
TIM	Total Irradiance Monitor
TIROS	Television Infrared Observational Satellite
TOA	Top-of-atmosphere/top-of-the-atmosphere
TRMM	Tropical Rainfall Measuring Mission
TSI	Total solar irradiance

UTH	Upper tropospheric humidity
WFOV	Wide-field-of-view